Measuring and modelling the influence of weather factors on CSP reflector soiling

by

Jones Musango

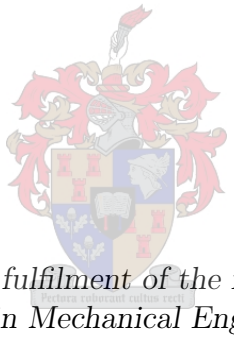

Thesis presented in partial fulfilment of the requirements for the degree of Master of Engineering in Mechanical Engineering in the Faculty of Engineering at Stellenbosch University

Supervisor:

Prof. Frank Dinter

December 2016

Declaration

By submitting this thesis electronically, I declare that the entirety of the work contained therein is my own, original work, that I am the sole author thereof (save to the extent explicitly otherwise stated), that reproduction and publication thereof by Stellenbosch University will not infringe any third party rights and that I have not previously in its entirety or in part submitted it for obtaining any qualification.

Date: . . December 2016 . . . . . .

Abstract

Measuring and modelling the influence of weather factors on CSP reflector soiling

J. Musango

Department of Mechanical and Mechatronic Engineering,
University of Stellenbosch,
Private Bag X1, Matieland 7602, South Africa.

Thesis: MEng (Mechanical)

March 2016

South Africa is among the countries with a plan to reduce GHG emissions of up to 34% by 2020 through investment in renewable energy in order to reduce its base load coal generation. High solar resource and the potential of concentrated solar power (CSP) to address the challenges facing other solar technologies have attracted CSP investment in the country. CSP uses reflector surfaces or mirrors to focus low solar energy radiation from a large field into a small area of high energy concentration. In their working conditions, CSP reflector surfaces are subjected to harsh outdoor environments which drastically degrade their performance. The main objective of the study was to develop and test reflector optical degradation measurement device and use these optical degradation measurements from the device to relate optical losses caused by soiling to weather.

A reflector optical degradation assessment device termed as real-time cleanliness monitoring sensor (RCMS) was designed, developed and tested for its ability to measure soiling optical degradation. The device was then utilised to relate weather conditions with optical losses caused by soiling on CSP reflectors. Furthermore, a neural network model was developed to simultaneously relate various weather factors to the optical loss caused by soiling on CSP reflectors. Error analysis and calibration were undertaken for RCMS measurement in order to improve confidence in the data, which was further used in experimental analysis. Two experimental analyses were carried out. The results from the first experimental analysis showed only the variation of cleanliness with weather factors that directly influence the rate of soiling. Wind speed and humidity were observed to degrade cleanliness, while rain lead to reflector cleaning. In the second experimental analysis, factors that directly or indirectly influence cleanliness were statistically analysed using clustering method. The results showed that temperature and direct normal irradiation (DNI) correlate relatively well with cleanliness although they do not directly influence it. The neural

network model demonstrated that a combination of weather factors could be used to estimate the optical degradation caused by soiling on CSP reflectors. High coefficient of determination was observed from the neural network model results, as compared to the correlations that considered the relationship between cleanliness and a single weather factor, done in the experimental analysis.

Keywords: Concentrated solar power (CSP); reflector optical degradation; cleanliness; soiling losses

Uittreksel

Die meting en modellering van die uitwerking van weerfaktore op die bevuiling van gekonsentreerdesonkrag(GSK)-reflektors

("Measuring and modelling the influence of weather factors on CSP reflector soiling")

J. Musango

Departement Meganies en Megatroniese Ingenieurswese,
Universiteit van Stellenbosch,
Privaatsak X1, Matieland 7602, Suid Afrika.

Tesis: MEng (Meganies)

Maart 2016

Suid-Afrika is een van die lande wat oor 'n plan beskik om die vrylating van kweekhuisgas (KHG) met tot 34% teen 2020 te verminder deur in hernubare energie te belê en sy basislas-steenkoolopwekking te verlaag. Die omvangryke sonkraghulpbron en die potensiaal van gekonsentreerde sonkrag (GSK) om die uitdagings wat ander sonkragtegnologieë in die gesig staar te trotseer, lok GSK-belegging vir die land. GSK gebruik reflektoroppervlakke of spieëls om lae sonkraguitstraling vanaf 'n uitgestrekte gebied na 'n klein area met 'n hoë konsentrasie energie te herlei. GSK-reflektoroppervlakke word in hul werkende toestand aan strawwe buitelugomgewings onderwerp, wat hul werkverrigting drasties verlaag of degradeer. Die studieoogmerk was om 'n model vir die beraming van hierdie optiese degradasie, wat die gevolg van die bevuiling van GSK-reflektoroppervlakke vanweë weerfaktore is, te oorweeg en te ontwikkel.

'n reflektor- optiese degradasie-assesseringstoestel, of intydse "skoongehalte-monitorsensor (ISMS), is ontwerp, ontwikkel en getoets om die vermoë van die toestel vir die meet van bevuilings- optiese degradasie te bepaal. Die toestel word ook gebruik om die verband tussen weersomstandighede en optiese verliese weens vuil GSK-reflektors aan te dui. Daarby is 'n neuralenetwerkmodel ontwikkel wat verskillende weerfaktore gelyktydig met optiese verliese vanweë die bevuiling van GSK-reflektors in verband bring. Foutontleding en kalibrering is vir ISMS-meting gedoen om databetroubaarheid te verhoog en by eksperimentele ontledings te gebruik. Twee eksperimentele ontledings is uitgevoer. Die resultate van die eerste eksperimentele ontleding het slegs die "skoongehalte"-variasie by weersomstandighede wat die bevuilingskoers direk beïnvloed, aangedui. Daar is bevind dat windspoed en vogtigheid skoongehalte degradeer, terwyl reën die reflektors skoon spoel. In die tweede eksperimentele ontleding is faktore wat 'n direkte of indirekte uitwerking op "skoongehalte" het statisties

aan die hand van die klustermetode ontleed. Die uitslae toon dat temperatuur en direkte normale irradiasie (DNI) relatief goed met skoongehalte korreleer, ofskoon dit nie 'n direkte uitwerking op skoongehalte het nie. Die neuralenetwerkmodel toon dat 'n kombinasie van weerfaktore gebruik kan word om 'n raming van die optiese degradasie wat deur bevuiling aan die GSK-reflektors aangerig word, te gee. 'n Hoë vasstellingskoëffisiënt is by die neuralenetwerkmodel waargeneem in teenstelling met die korrelasies wat die verband tussen skoongehalte en 'n enkele weerfaktor oorweeg het, soos in die geval van die eksperimentele ontleding.

Sleutelwoorde: Gekonsentreerde sonkrag (GSK); reflektor- optiese degradasie; skoongehalte; bevuilingsverliese

Acknowledgements

My sincere gratitude goes to the following people for their input in this research which took place in one way or the other. Firstly I thank the Almighty God, whose Grace has seen me through this masters journey.

My study leaders Prof. Frank Dinter for his support, guidance, ideas and advice during the research meetings and discussion. I owe gratitude to Mr. Paul Gauche who saw my potential and involved me in the Solar Thermal Energy Research Group (STERG) and identified the funding opportunity that supported this study. The STERG members are acknowledged for creating an exiting and fun environment. I would like to specifically thank Mr. Frank Hoffman and Gavin Van der Merwe at the solar roof for their untiring support during experimentation. Sincere thanks to the mechanical department workshop team, specifically Mr. Cobus Ziestsman for the assistance offered in designing the parts manufactured for the experimental device.

My parents and siblings for their spiritual and physical support and the opportunities they have given me not only during the two years of my research period but over my entire life. I owe much gratitude to my sister, Dr. Josephine Musango, who gave moral and emotional support and advice during the entire period of my master's study. I also want to thank you for the assistance in editing. I would not have been strong without the support from people such as Sylvanus Mensa, Mukama Matia, Omotoyosi Craig, Xiao Zheng and Brian Ssebabi.

Last but not the least I would like to thank the National Research Foundation (NRF) for the funding they provided to this study.

Contents

List of Figures

List of Tables

Nomenclature

Annotations

E_{abs}	Absorbed energy
I_b	Incident beam radiation
ρ_{spec}	Specular reflectance
$\rho_s(\lambda, \theta, \psi)$	Solar specular reflectance
$\rho_{spec}(SW, \theta, \psi)$	Solar weighted specular reflectance
ρ_{hem}	Hemispherical reflectance
$\rho_{hem}(SW, \theta, 2\pi)$	Solar weighted specular reflectance
$E_{\lambda i}$	Irradiance fraction at wavelength λ_i
$E_{0-\infty}$	Cumulated solar irradiation
V_z	Particle velocity in z direction
U_z	Wind velocity in z direction
r	Aerodynamic radius
ρ_p	Density of particle
t	time
ϕ_i	Incident radiation flux
ϕ_i	Reflected radiation flux
K_j	Scattering coefficient
R_{soil}	Soiling rate
ρ_{clean}	Clean reflectance
ρ_{soil}	Soiled reflectance
ρ_{Ref}	Reference reflectance
DNI_r	Reflected direct normal irradiation
DNI_{sun}	Incident direct normal irradiation
$\rho_{abs}(\psi, \theta)$	Absolute Solar reflectance
C	Cleanliness
w_{jk}	weight between k and j neuron
$V(k)$	Summation output kth neuron
$Y(k)$	Output of kth neuron

d_i	Target output
E_n	Error nth measurement
b_k	Bias in kth neuron
x_i	Input parameter i
a_{min}	Minimum measurement value
a_{max}	Maximum measurement value
C_{est}	Estimated cleanliness
C_{meas}	Measured cleanliness
$C(t)$	Cleanliness at time t

Greek letters

α	Absorptance
θ	Incidence angle
λ	Wavelength
ξ	Weight bias summation
ρ	Reflectance
ϕ	Radiation flux
τ	Transmittance
ψ	Acceptance angle
Γ	Capture fraction
Δ	Change
Σ	Sum
Ψ	Transfer function
Ω	Surface

Subscripts

abs	Absolute
b	Beam
clean	Clean
est	Estimated
i	Incident
j	jth neuron
k	kth neuron
meas	Measured
n	nth Value
Ref	Reference
soil	Soiled
spec	Specular
r	Reflected

z Height direction

Abbreviations

ANN Artificial neural network
ASTM American standards of testing materials
CAD Computer aided drawing
CPV Concentrated photovoltaic
CSP Concetrated Solar Power
DHI Diffuse horizontal irradiation
DNI Direct normal irradiation
GHG Green house gases
GHI Global horizontal irradiation
IRP Integrated resource plan
ISO International standards organization
LCOE Levilised cost of electricity
MLFF Multi layer feed forward
O&M Operations and maintenance
PTC Parabolic trough collector
PV Photovoltaic
RCMS Real time cleanliness measuring device
SCA Solar collector assembly
SSR Solar specular reflectance
SW Solar weighted

Chapter 1

Introduction

1.1 Background

Renewable energy technologies have been adopted in many developed and developing countries due to increasing global energy demand, decrease in fossil fuel deposit and the rise in concerns to mitigate climate change. South Africa is among the countries that have committed to reduce its CO_2 and other green house gas (GHG) emission levels. The country has set a target to achieve a 34% reduction in GHG emission by the year 2020 by adopting renewable energy sources as an alternative to its current base load coal generation (Ziuku and Meyer, 2012; Department of Environmental Affairs, 2011).

Renewable energy technologies such as photovotaic (PV) and wind technologies have experienced a rapid expansion in the 2000s but there are still some valid concerns regarding the integration of these renewable energy sources in conventional power generation infrastructure. Large scale electricity storage needs to be developed in order to dispatch wind or PV in a conventional electricity grid. Nonetheless, the technical potential of renewable energy and specifically solar energy is still tremendous. South Africa has made solar the priority renewable energy source, and recently, there has been a plan to include concentrated solar power (CSP) generation into current electricity generation mix due to shortfall in electricity base load capacity and concerns about its coal reserves depletion. According to the Integrated Resource Plan (IRP), CSP capacity of 600MW has already been allocated for the period upto the year 2030 with an option of additional 400MW capacity (Department of Energy, 2010). The first 100 MW grid connected commercial CSP plant has been in operation since April 2015 (Heerden *et al.*, 2015).

Conventional CSP technologies use reflective surfaces usually mirrors to concentrate low energy solar radiation from a large solar field into a small area of high energy concentration in form of heat which is then utilised in normal thermodynamic cycle to produce electricity (Raccurt *et al.*, 2014). It is worth mentioning that the attractiveness of CSP lies in the fact that it provides a solution to the challenges presented by wind and PV technologies. In contrast to the latter, CSP benefit from advances in thermal storage which enables them to generate energy under a cloudy

sky or after sunset. This has significantly increased their capacity factor[1] and has provided for the generation of dispatchable electricity for grid integration. However, the cost of electricity produced by CSP is still high when compared to electricity generated by conventional fossil power plants. Nonetheless, CSP technology is expected to experience the same development as PV or wind power experienced during the past decade.

Most international CSP based research programmes aim at reducing the components and systems cost and improving the system performance of CSP technology in order to make it competitive in the market. This study focused on optical degradation of the CSP reflector surfaces due to outdoor exposure. The main optical characteristic of a reflector is its reflectance, which has to be highly specular for a maximum amount of incident beam radiation to be reflected onto the receiver. This high reflectance has to be maintained during the entire plant operation for maximum plant output.

1.2 Problem statement

The potential of soiling is a key factor in determining economic feasibility of CSP power plants. Direct normal irradiance (DNI) is the only solar resource of interest for concentrating systems. CSP systems can only be located in regions where the DNI is above 1800-2000 kWh/m^2 per year referred to as the world's Sun- belt (Caron, 2011).

While DNI radiation is an important criterion for the optimal sitting of CSP projects, the appropriate DNI levels are found in arid and semi- arid regions which are frequented by dust and dust storms due to lack of vegetation (Herrmann *et al.*, 2014). Evidently, the reflectors used in CSP application are exposed to these harsh outdoor environment which leads to degradation of the mirror optical characteristics. Dust on CSP reflectors form a critical event because solar field performance and power sales revenue are directly related to the optical characteristics of mirrors. Although dust causes reversible optical degradation, techniques used to restore the high optical performance are labour intensive, make use of water, which is a scarce resource in these areas, and lead to increase in operation and maintenance (O&M) costs.

Currently the soiling rates of most of these solar potential regions are not yet known. Understanding the key variation of optical losses caused by soiling has been challenged by the spatial variation of soiling losses. The variation of soiling losses is influenced by the local weather factors. However, very little attention has been given to the influence of weather factors and how they relate to the rate of soiling. Understanding the relations between the optical losses caused by soiling on CSP reflectors and the weather factors, may be vital in providing insights into improving the performance and cleaning routines of CSP plants.

[1]This is a measure of how often an electric generator runs for a specific period of time. It expresses the average percentage of full capacity over a given period of time usually a year.

1.3 Objective

The objective of this study is to establish a CSP reflector optical degradation assessment method in order to relate optical losses caused by soiling with weather conditions. To achieve this, the sub-objectives were:

i To develop and test a reflector soiling optical degradation device.

ii To relate optical losses caused by soiling of CSP reflectors to local weather factors in an experimental analysis.

iii To develop a neural network model to estimate optical losses caused by soiling on CSP reflector by relating the combined effect of weather factors to reflector soiling.

1.4 Thesis Outline

Chapter 1 introduced the study and its objectives.

Chapter 2 reviews the literature on CSP systems and their working principles with a key focus on CSP reflector materials optical requirements and optical assessment of reflector surface. The composition of soiling materials is discussed alongside the factors influencing aeleon[2] dust concentrations. Factors influencing the rate of reflector optical degradation are outlined. Existing reflector optical degradation assessment devices are outlined in order to identify appropriate measurement techniques that would be applied in this study.

Chapter 3 presents the experimental procedures followed to achieve the research objectives. The assessment requirements of reflector optical losses caused by soiling in the CSP context are discussed. A description of the adopted device for assessment of optical degradation caused by soiling is provided. Other existing devices used in experimentation are also outlined. The experimental strategy, procedures and planing are further discussed.

Chapter 4 discusses the procedure followed in modelling the weather factors to estimate CSP reflector optical losses using a neural network model.

In Chapter 5, the experimental and neural network model results and key findings are presented and discussed.

In Chapter 6, the conclusions and recommendations based on research findings are discussed.

[2]Dust suspended in air

Chapter 2

Literature review

2.1 Introduction

The objective of this chapter is to familiarise the reader with the key study area and outline previous works related to the current research field. In the first section, CSP systems and their working principles are briefly introduced. The reflector materials and their different optical characteristics are discussed in the second section. In the third section, dust physics and chemistry along with the processes leading to dust advection are discussed. The influence of dust on CSP reflector surfaces is discussed in the fourth section, as well as the parameters influencing the rate of optical losses caused by soiling on CSP reflector surfaces. The existing devices and methods used to quantify optical losses caused by soiling on CSP reflector surfaces are discussed thereafter. Finally the attempts made to relate weather factors to soiling rates and consequently optical losses caused by soiling are then outlined.

2.2 Concentrated solar power systems

The basic working principle of CSP has been briefly outlined in Section 1.1. CSP systems generally consist of three sub-systems; solar field, thermal storage and thermal Power Conversion Unit (PCU). This section outlines the current solar field technologies and provides a description of CSP solar collector assemblies (SCAs) and their characteristics. The cost and performance of these system is outlined thereafter.

2.2.1 Solar field technologies and application

The function of the solar field is to concentrate direct solar radiation and convert the radiation flux into useful heat. This function is performed by solar reflectors, usually the mirrors. CSP technologies are categorised depending on the organisation of SCAs as line concentrators and point concentrators as shown in Figure 2.1. In line concentrator systems, solar radiation is concentrated on a linear receiver as in parabolic trough collector (PTC) and liner Fresnel collectors (Stine and Geyer, 2001). In point concentrator systems, solar radiation is concentrated on a point as in central receiver systems and parabolic dish system (Stine and Geyer, 2001). In

comparison to line concentrators systems, point concentrators systems can achieve a higher range of useful temperatures due to higher concentration ratio (Duffie and Beckman, 1980).

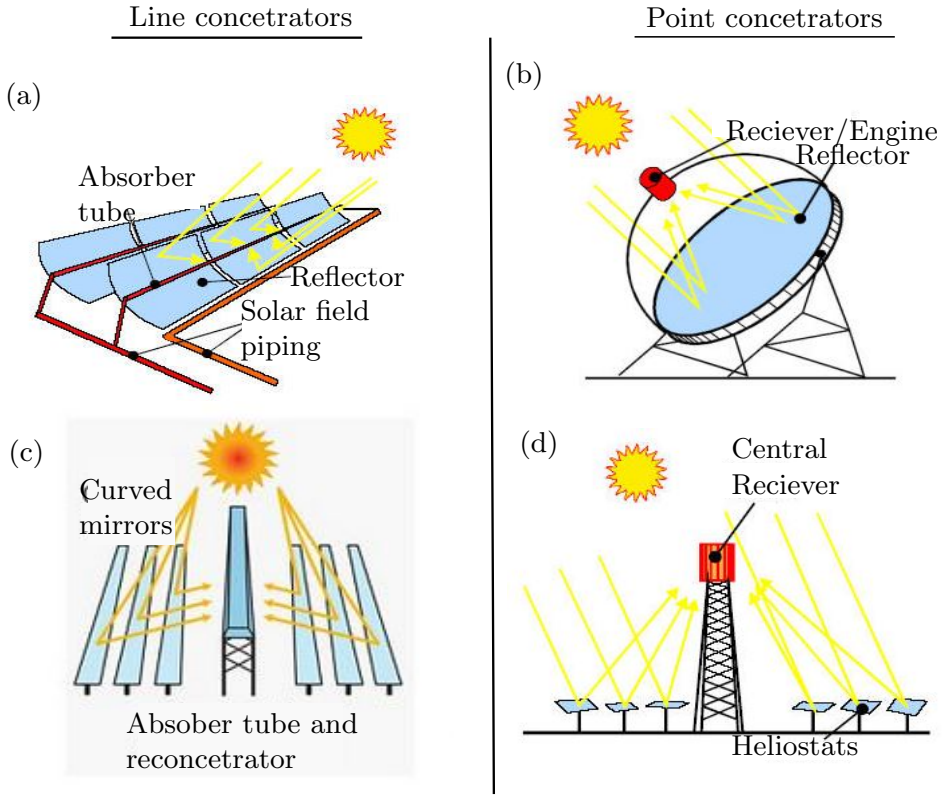

Figure 2.1: Concentrated solar power technologies; (a) parabolic trough (b) parabolic dish (c) linear fresnel (d) central receiver. ((IEA), 2010)

The most common application of CSP is power generation. The parabolic trough collector (PTC) is the most mature solar field technology. Other solar field technologies are at the stage of commercial demonstration. The solar tower has an advantage of centralized electricity generation, while parabolic dish[1] system have to compete with concentrated photovoltaics (CPV) for decentralized application due to lack of storage system ((IEA), 2010).

2.2.2 Solar collector assemblies (SCAs)

SCAs consist of solar reflectors,concentrator structures, receivers, and other components (foundations, drive, pylons, connections and controls). This section outlines the optical characteristics of SCAs.

[1]In these system the collected heat is directly utilised to run a Stirling engine.

The main characteristic of a SCA is its concentration ratio. Two different definitions of concentration ratio are in general use which are optical concentration ratio and geometric concentration ratio (Stine and Geyer, 2001). Geometric concentration ratio is defined as the ratio of the reflector aperture area to the area of the receiver. Alternatively, one can define concentration ratio using flux ratio as in ratio of flux at a certain point ion the receiver to the flux on the collector aperture ((IEA), 2010).

The second important optical characteristic of SCAs is the acceptance angle, denoted as ψ. The acceptance angle is defined as the maximum angle at which reflected direct solar beams can be captured by the receiver. This depends on the SCA geometry. The minimum acceptance angle value corresponds theoretically to the angular diameter of the sun, which equals to 32'($\approx 0.53^{\circ}$ or 9 mrad) (Caron, 2011). In practice, the acceptance angle increases due to optical errors caused by certain factors such as tracking accuracy, misalignment of concentrator structures, deformation of reflectors or wind loads (Stine and Geyer, 2001). The concentration ratio is affected by the acceptance angle,that is, the higher the acceptance angle is, the larger the receiver area must be to collect reflected solar radiation, thus lowering the concentration ratio. Reciprocally, the SCA geometry determines the maximum acceptance angle and thus the requirement on optical errors, such as tracking accuracy (Duffie and Beckman, 1980; Caron, 2011).

The third SCA optical characteristic is the capture fraction, denoted by Γ, which is the fraction of the reflected radiation that is incident on the absorbing surface of the receiver (Stine and Geyer, 2001). Often, this is described in terms of 'spillage' that is, the fraction of reflected energy not impinging on or entering the receiver. A poorly shaped concentrator, or a receiver that is too small will make this number considerably less than 1.0, implying that there is increased spillage (Stine and Geyer, 2001).

Using the SCA characteristics described, the amount of absorbed radiation per unit area of aperture denoted E_{abs} (W/m^2) can be fomulated as (Stine and Geyer, 2001):

$$E_{abs} = I_b \rho_{spec} \Gamma \tau \alpha \tag{2.1}$$

where: I_b = incident beam radiation (W/m^2).
ρ_{spec} = specular reflectance of reflector.
Γ = Capture fraction.
τ = Transmittance of the receiver.
α = Absorptance of the receiver.

2.2.3 Cost and performance of systems

In the future, CSP technology is expected to compete with conventional power generation due to economies of scale, implementation of major technological improvements, cost and efficiency optimization (Sector *et al.*, 2012). Currently the main challenge facing CSP is the high cost of electricity generation defined by the Levilised cost of electricity (LCOE[2]), which is high when compared to that of fossil fuel.

[2]LCOE represents kWh cost of building and operating a generating plant over an assumed financial life and duty cycle.

LCOE of CSP systems depends on several factors, such as DNI, storage capacity, maturity of technology (learning rate/effects), nominal power capacity and plant efficiency among others (Caron, 2011).

According to Sector *et al.* (2012) the expected service lifetime of CSP plants should not exceed 30 years. The LCOE, which includes actualized capital, O&M costs, lies between USD 0.17-0.29 /kWh for new CSP plants including thermal storage and between USD 0.20 -0.36 /kWh for CSP plants without thermal storage (Sector *et al.*, 2012; Caron, 2011). However, in areas with excellent solar resources it could be as low as USD 0.14- 0.18/kWh. These are general cost estimates for the current state of the art technology, regardless of solar field technology.

The O&M costs are still relatively high for CSP plant and are in the range of USD 0.02 - 0.035/kWh, of which includes among others, cleaning of SCA due to optical losses induced by soiling (Caron, 2011). Understanding the soiling rates for improved cleaning routine could lead to substantial cost reductions. Moreover, cost reduction opportunities are likely to result from improved plant design and experience gained across a large number of plants.

2.3 Solar reflector materials

The cost of the solar field represent a significant part of the capital cost. Thus, there has been a significant evolution of solar reflector material since the inception of CSP technology. Research and development have aimed at achieving a durable and cost effective reflector material (Kennedy *et al.*, 2005) that is easy to maintain and replace, has good optical and mechanical properties that can withstand harsh outdoor environments, and can maintain these properties during its lifetime (Brogren *et al.*, 2004). The types of mirrors that have being identified for CSP application include: polymer, aluminium and glass mirrors (Kennedy *et al.*, 2005).

Solar reflector materials are generally categorized depending on where the reflecting material is deposited as first surface reflective material and second surface reflective material (Kennedy *et al.*, 2005). First surface reflector have their reflective surfaces located in front of the surface substance. An example of first surface reflector is aluminium. Second surface reflectors have reflective surface deposited on back of impervious stable material. An example of second surface reflector is low iron silvered glass mirrors. Commercial CSP plants make use of low iron glass with silver coating behind the glass as the reflective material.

2.3.1 Concentrator optics

As indicated in Equation 2.1 in Subsection 2.2.2, the mirror reflectance directly affects the amount of absorbed solar radiation. From theory, two cases of reflection of light by a surface are observed, that is, specular reflection and diffuse reflection (Taylor, 2009).

Specular reflection defined as the amount of light coming from a single direction that is reflected into a single outgoing direction as shown in Figure 2.2 (a). In specular reflection, the laws of reflection comes into play. Both incident beams and reflected beams lie on the same plane and are symmetric with respect to the normal axis at the point of incidence on the surface, such that the angle of incidence θ_i is equal

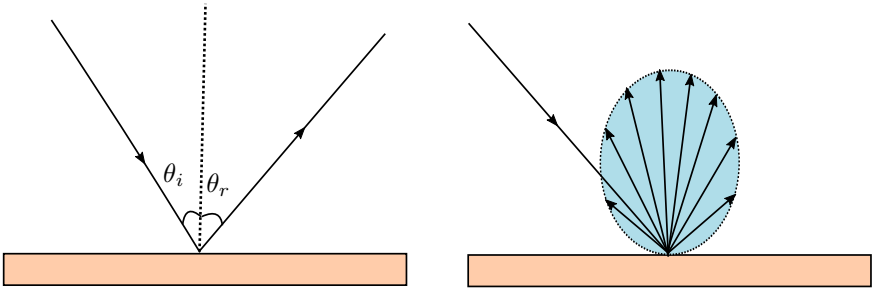

(a). Specular reflectance (b). Diffuse reflectance

Figure 2.2: Cases of reflection of light: Adapted fromTaylor (2009).

to the angle of reflection θ_r. The magnitude of specular reflection is characterized by the specular reflectance ρ_{spec}. Specular reflectance is measured with a spectral specular reflectometer (SSR) and the solar weighted (SW) specular reflectance $\rho_{spec}(SW, \theta, \psi)$. This can be evaluated using Equation 2.2 assuming that the ratio of specular reflectance to hemispherical reflectance is constant over the entire terrestrial solar spectrum as well as the ratio of wavelength interval.

$$\rho_{spec}(SW, \theta, \psi) = \frac{\sum_{\lambda=250}^{2500} \rho_{spec}(\lambda_i, \theta, \psi)\rho_{hem}(SW, \theta, 2\pi)}{\sum_{\lambda=250}^{2500} \rho_{hem}(\lambda_i, \theta, 2\pi)} \tag{2.2}$$

where: $\rho_{spec}(\lambda_i, \theta, \psi)$ = Specular reflectance at various λ_i and θ.
$\rho_{hem}(SW, \theta, 2\pi)$ = Solar weighted hemispherical reflectance.
$\rho_{hem}(\lambda_i, \theta, 2\pi)$ = Hemispherical reflectance at various λ_i.

Diffuse reflection is the reflection of light from a surface such that an incident ray is reflected at all spatial angles rather than a single direction as shown in Figure 2.2 (b). In practice no reflector surface that can produce a perfect specular or diffuse reflection and a combination of both is exhibited in almost all of the materials (Kennedy *et al.*, 2005). Furthermore, direct solar radiation is not perfectly collimated and hence reflection on a specular surface is spread in a cone with an acceptance/aperture angle ψ. Hemispherical reflectance ρ_{hem} characterizes the sum of specular and diffuse reflection magnitudes. Hemispherical reflectance ρ_{hem} is measured using integrated sphere reflectometers and solar weighted hemispherical ρ_{hem}(SW, θ, 2π) reflectance is evaluated using Equation 2.3.

$$\rho_{hem}(SW, \theta, 2\pi) = \sum_{t=250}^{k} \rho_{hem}(\lambda_i)\left(\frac{E_{\lambda i}.\Delta_{\lambda i}}{E_{0-\infty}}\right) \tag{2.3}$$

where: λ_i = Mid-wavelength of the wavelength interval $\Delta_{\lambda i}$
$E_{\lambda i}$ = Solar irradiance fraction at the wavelength λ_i.
$E_{0-\infty}$ = Cumulated solar irradiance at λ = 250-2500 nm.

Since the function of reflectors used in concentrating solar collectors is to concentrate direct solar radiation onto a receiver, the reflector surface must exhibit a high

solar weighted specular reflectance ρ_{spec}(SW, θ, ψ) for any wavelength within the solar spectrum range. The magnitude of reflected radiation is a function of wavelength λ (nm) and spatial distribution of the incident radiation (Duffie and Beckman, 1980). When soiling occurs on reflective collector surfaces, a significant proportion of light is scattered and lost because the optical parts are not able to focus the scattered light specularly on a given point (Meyen *et al.*, 2014).

2.4 The physics of dust

This section discusses the concept of dust and various modes of dust transport and deposition.

2.4.1 Definition of dust

Dust is a general term for any particulate matter with diameter $\phi \leq 500\mu$m, which is about the dimension of an optical fibre used for communications or 10-times the diameter of a human hair (Sarver *et al.*, 2013). According to the study carried out by Call (1980), over 60% of the soiling contaminants have a particle size within the range of 200 μm-500 μm in most of the sites with the rest of particle sizes being $\leq 200\mu$m. Particulate matter with particle diameters $\phi > 500\mu$m are classified as a combination of sand, silt and clay according to Wentworth scale[3] (Wentworth, 1922), and follows a standard norm ISO 14688-1, which is used in engineering for the purpose of identification and classification of natural soils (Karim *et al.*, 2014).

The various sources of particulate matter making up dust include; atmospheric aerosols, geomophic minerals and biological matter such as plants/ animal cells, which include but are not limited to pollen algae and bird droppings (Sarver *et al.*, 2013). The composition of the constituents of dust varies from region to region (Elminir *et al.*, 2006) and is influenced by factors such as human activities and vegetation among other contributing factors (Sayyah *et al.*, 2013).

According to Nelson *et al.* (2011) there is a spatial variation in mineralogic composition of dust. In their study, they analysed the composition of reflector soiling material using X- ray diffraction for five different sites located in the south western united states. The elemental variation of the soiling compounds for the five sites is shown in Figure 2.3. The bulk minerals in terms of weight were in decreasing order: quartz or silicon dioxide (SiO_2) Aluminium oxide (Al_2O_3), and ferric oxide (Fe_2O_3). This can be explained by the abundance of these chemical elements on earth and their resistance to weathering (Caron, 2011). Similar studies investigating mineralogical variation with season were conducted by Elminir *et al.* (2006). Common elements were reported as for those identified by Nelson with a significant variation of the elements over a season. This can be explained by weathering of some chemical elements, for instance, limestone as compared to silicon.

2.4.2 Dust emission and transport

The emission and transport of dust occur simultaneously since these two processes are mainly initiated by wind (Tanabe, 2008; Heinold *et al.*, 2009). Factors such as

[3]Wentworth scale classifies soiling particles as per particle size rather than composition.

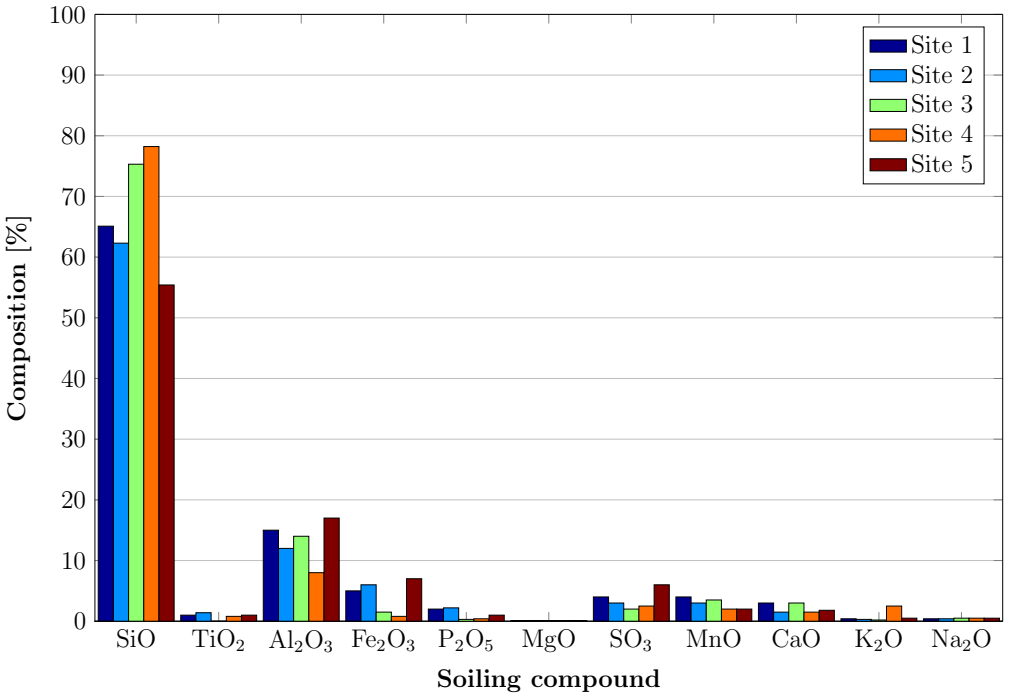

Figure 2.3: Chemical composition of organic soiling components. Reproduced from: (Elminir *et al.*, 2006).

particle shape, particle size and moisture content only determine either the mode of transport or the ease with which the particle is emitted (Petavratzi *et al.*, 2005). There are three known modes of dust transport. These are identified as: creeping, saltation and airborne suspension (Caron, 2011; Barrierger, 1978). All these three modes of dust transport are initiated by wind.

Surface creep involves the rolling and/or sliding of relatively large particles (500 μm -1000 μm) along the ground. This occurs when the particle aerodynamic force fail to exceed gravitational force. Saltation refers to the jumping and bouncing of particles within a few centimetres of the surface. Particles that saltate vary in size from 100 μm -500 μm and are brought back to the surface due to their size and density. Wind tunnel experiments conducted by Barrierger (1978) indicate saltation to be the most predominant mode of transportation.

Airborne suspension describes the transport of particles less than 100 μm diameter, which are lifted from the ground and are completely borne up by the wind. This occurs when the upward eddies currents have a larger magnitude than the terminal velocity of fall of particles and since the terminal settling velocity of particles increase with size, there is a maximum particle size that can be suspended by a given turbulent updraft. The acceleration of a particle is described by Equation 2.4.

$$\frac{dV_z}{dt} = \frac{-3\rho C_0 (U_z - V_z)^2}{8 r \rho_p} \tag{2.4}$$

where: C_0 = Coefficient of drag.
r = Aerodynamic radius.
U_z = Velocity of wind in z direction.
V_z = Velocity of Particle in z direction.
z = Height above the ground.

2.4.3 Dust deposition

The deposition of dust particles on a mirror surface is controlled by the complex fluid mechanical interaction of the dust laden air stream with the entire mirror structure (Roth *et al.*, 1980). The understanding and eventual control of dust on solar reflectors and other surfaces will eventually depend significantly on the understanding of the mechanics of the fundamental dust accumulation process (Barrierger, 1978). The soiling or deposition process itself involves delivering the dust to the surface either by directive of attractive processes, the initial adhesion of dust, changes in adhesion by condensation and chemical reactions.

These processes themselves involve multiple and sometimes interdependent interactions that add layers of complexity to modelling or unravelling the controlling parameters. The deposition rate and bond strength is a function of not only the type of dirt particle and mirror surface material but also of numerous environmental conditions, geographical and site effects, design features and time effects (Biryukov, 2000). Processes such as convective diffusion, impaction and sedimentation play an important role in the deposition process depending on particle size and wind velocity particle size.

The study conducted by Roth *et al.* (1980) provides a theoretical understanding of the different dust deposition mechanisms and material properties affecting each of the deposition mechanisms. Details of the settling mechanisms identified from their study are provided in Table 2.1. In a different study, Berg (1978) showed that the initial deposition depends on the surface itself, its composition, chemistry, morphology, conductivity and electrostatic properties. He also found that these adhesion forces can increase to greater than 10,000 times the gravitational force thereby rendering the dust removal all but impossible without damaging the surface.

Cuddihy (1980) described the known and postulated mechanisms of soil retention on surfaces, and inferred from these mechanisms that low soiling and easily cleanable surfaces should have low surface energy, and be hard, smooth, hydrophobic and chemically clean of sticky materials and water soluble salts. While these studies provide a primal understanding of the deposition mechanisms, they do not provide details of the order of each of deposition mechanism. Building on these findings, Sarver *et al.* (2013) have suggested that initial deposition is due to particles falling onto the surface through gravitational settling. These particles are then held together by electrostatic charges and can be washed away by wind or water. These authors further suggested that after settling, particles are held by charge double layer, surface energy and capillary effects in addition to gravitational and electrostatic forces.

Table 2.1: Soil deposition mechanisms

Mechanism	Affected material property
Gravity	Mass
Electrostatics	surface (coating) conduction
Charge double layer	Contact potential (difference in work functions)
Van der walls forces	Particle size; Surface roughness
Surface energy	Solid relaxation
Capillary force	Fluid Surface relaxation Chemical/ physical bond Chemical activity

2.5 Soiling of CSP reflector surfaces

Soiling is the process in which surfaces become dirty during exposure to the outdoor environment. Dirt herein and thereafter referred to as dust, is anything that settles on the surface thereby changing the physical and / or chemical properties of the surface. This section describes the factors that influence the presence of aeolian aerosols (dust) and factors influencing the threat posed dust on SCA reflector surfaces.

2.5.1 Impact of dust on reflector optics

Accumulation of dust on solar mirrors basically leads to absorption and scattering of light and a reduction in the reflective surface area (Vivar *et al.*, 2010). It has been indicated by several authors that the primary effects of dust on reflector surfaces is scattering rather than absorption (Sarver *et al.*, 2013). The scattering effect is associated with reduction in specular reflection and an increase in diffuse reflection.

According to Freese and Pettit (1980) different scattering effects of dust are observed at all wavelengths in the entire solar spectrum. From their study conducted in a 5 MW solar thermal test facility located in Albuquerque, New Mexico, a difference in measurement of specular reflectance was observed from different accumulated dust particles sizes using a Bidirectional reflectometer at wavelength ranges between 400nm -900nm for five silvered glass mirrors exposed to five weeks outdoor environment as presented in Figure 2.4.

Several empirical studies investigating the impact of dust on reflector surfaces have correlated light scattering effects of dust in a number of ways. For instance, Vivar *et al.* (2010) have compared optical degradation to the reduction in electrical output of CPV systems reporting maximum losses in electrical output of upto 26% for mirrors exposed for a period of four months. Roth *et al.* (1980), investigated the degradation of specular reflectance and reported a loss in specular reflectance of 25% for two weeks for mirror materials under outdoor exposure test. Wolfertstetter (2013) related the errors incurred in DNI measurement using two pryheliometer one which is kept clean and the other exposed to degradation. A 25% reduction in measured values of DNI for exposure period of few weeks is reported from the

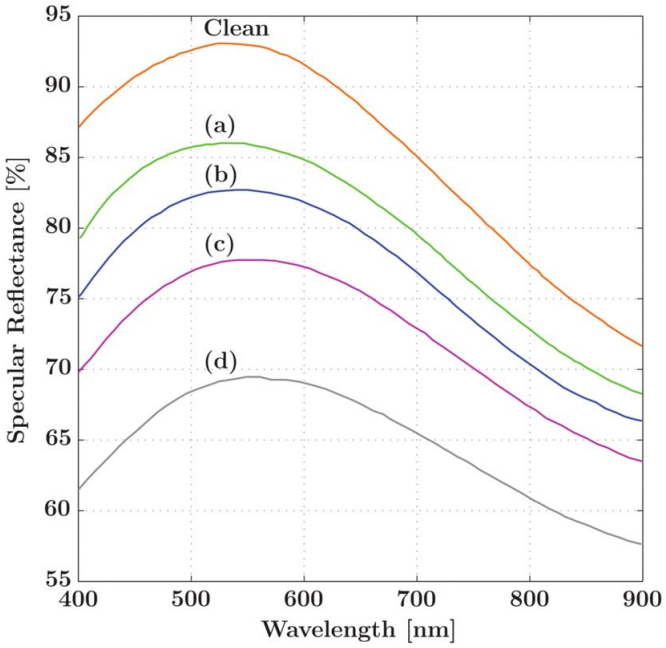

Figure 2.4: Variation of specular reflectance with wavelength for clean and dusty mirror samples exposed in Albuquerque, NM. Dust concentration density increases from (a) to (d): Adapted from (Sayyah *et al.*, 2013).

degraded pyrheliometer. Deffenbaugh *et al.* (1986) investigated thermal efficiency loss of parabolic trough system. They reported 1.3% daily reduction in efficiency. The research above was based on the number of days, weeks, or months of exposure which does not lead to a general correlation for the dust effect, because the amount of dust accumulating on the reflective surface is different from one place to another for the same number of days, weeks, or months of exposure.

Several empirical studies that have investigated the soiling phenomenon correlate the time of exposure or the amount of accumulated dust with the measured optical loss or performance of the solar collector (Sarver *et al.*, 2013; Vivar *et al.*, 2010; Mani and Pillai, 2010). Of particular interest is the site variation in potential of soiling that has been described in most of these studies. Nevertheless, no useful effect of dust on solar collectors that has been reported in any of the reviewed literature.

El-Shobokshy and Hussein (1993) carried out an experimental study aimed at providing a general correlation that avoids the uncertainity associated with seasonal and site variations of soiling in CPV systems. Their study concluded that the deposition density, given as dust accumulation per unit area, represents the extent of the impact of dust much better as compared to exposure period. Although these claims attempt to generalise the optical effect of dust, the challenge is that inhomogeneity of soiling materials is witnessed in particular instances. On the other hand, authors such as Call (1980) argue that different soiling materials might have different optical effects.

According to Call (1980), the optical effects of each of the particular contaminants is determined by the optical properties, quantity, size and shape of the accumulated particles. He argued that smaller particle sizes such as those with diameters within

0.3-2 μm posses the greatest potential for optical loss. He also suggested that the mineralogical composition of the contaminants affects the sticking effect and the ease with which cleaning can be done.

2.5.2 Parameters influencing the rate of soiling

The phenomenon of soiling on SCAs surfaces is very complex and involves the dependence and inter- dependence of several factors that lead to emission, transport and deposition of dust particles on SCAs surfaces. These processes are driven and affected by factors such as: wind speed, wind direction, precipitation, soil type, humidity, human activities, industrial activities and vegetation cover among other factors (El-Shobokshy and Hussein, 1993; Herrmann *et al.*, 2014). A summary of factors affecting the rate of soiling is shown in Figure 2.5. The rate at which all these process take place is referred as the soiling rate.

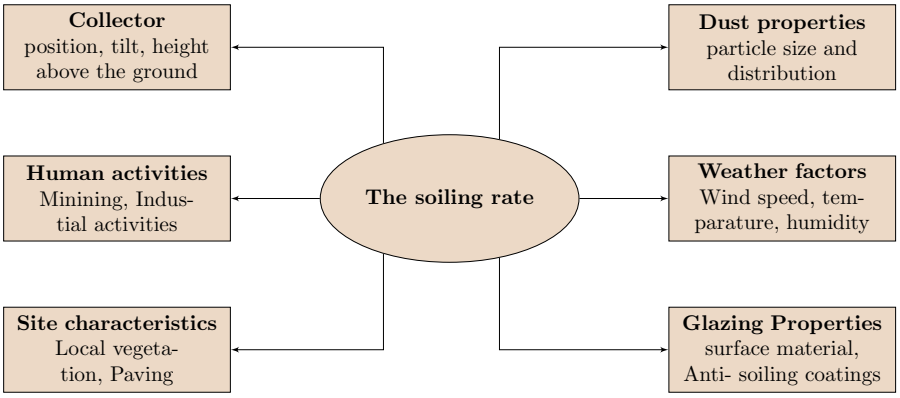

Figure 2.5: Factors affecting the rate of soiling Source: Own compilation.

As indicated in Section 2.5.1 accumulation of dust leads to the degradation of optical characteristics of solar reflector surfaces. An understanding of the rate at which dust accumulates on the surface provides an idea of the dust risk which helps in the development of a mitigation routine.

Several studies associated with rate of soiling in the CSP context have been carried out. These studies present their results which are integrated over long time periods over a wide spread of meteorological conditions (Igel and Hughes, 1979). They provide evidence of a meaningful relationship between reflector optical degradation to parameters influencing the rate of soiling such as reflector surface material (Fend *et al.*, 2003; Blackmon, 1978), collector position and orientation (Roth *et al.*, 1980; Elminir *et al.*, 2006), dust particle size and composition (El-Shobokshy and Hussein, 1993; Nelson *et al.*, 2011). Few attempts have been made to relate the rate of soiling to the weather factors.

According to Fend *et al.* (2003), one of the major design factors affecting the choice of reflectors for CSP applications is precisely their resistance to dirt accumulation. From a materials science perspective, they elegantly documented what might

be logically inferred, that some material surfaces can accumulate negligible amounts of foreign matter, whereas others seem to attract or build up soiling that significantly reduces reflectance under the same conditions.

The effect of one type of dust on two physically different reflector surfaces, namely glass and acrylic mirror, was described anecdotally by Blackmon (1978). Reflectance data were taken before and after the occurrence of a major dust storm. Following the storm, a layer of fine dust was observed on the two reflector surfaces. The specular reflectance loss from the glass reflector and acrylic reflector was 7.17 % and 10.95% respectively. Blackmon (1978) indicates that the difference in surfaces accounted for differences in adhesion properties. Moreover, the glass reflector returned almost to its original pristine condition after mild cleaning with water, however, the acrylic one did not. He concluded that the dirt adhesion was greater on the acrylic surface, although there was the possibility of abrasion damage or surface penetration of the particles.

The angle of inclination of a solar collector, and more generally its orientation, has been shown to be a decisive factor in determining the rate of soiling. Mirror orientation during the exposure period affects the particle size and distribution of accumulated particles (Call, 1980). Studies such as those conducted by Roth *et al.* (1980) and Elminir *et al.* (2006) indicate that the quantity of suspended particles deposited on mirror surface decrease with increase in tilt angle.

According to Elminir *et al.* (2006), dust particles tend to roll as the tilt angle increases. Their study conducted with samples at different azimuth and tilt angles provides an understanding of the dynamics of physical dust settling. This study conducted by Elminir *et al.* (2006) investigated the impact of dust on transparent covers which does not represent dust impact on reflector surface. The results presented by Roth *et al.* (1980) relating reflectivity degradation as a function of tilt angle as shown in Figure 2.6 for five mirrors exposed to natural weathering for few days. It was observed that, high soiling rates are achieved at low collector incidence angle due to high chances of gravitational settling in the collector. Although the collector orientation has been a key focus in most of the soiling study conducted, little focus has been given on the influence of a tracking system on the rate of soiling.

According to Bowman *et al.* (2011), different parts of the solar field can soil at substantially different rates. Their study conducted on commercial CPV plant recorded a difference of degradation in performance of more than 10% for two CPV modules located 150m apart. This was related to the position of the mirror in the field. For instance, it was observed that mirror soiling rates particularly near to the cooling tower are high due to cooling tower drift. They therefore suggested that an awareness of these variations is essential to generating accurate prediction of site performance to maximizing the energy harvest throughout the field design and maintenance policies and to ensuring accurate estimate of ongoing performance.

Several theoretical studies have been conducted to provide an understanding of weather and climatic dependence optical losses caused by soiling of solar reflector surfaces. Cuddihy (1980) provided a theoretical understanding of the soiling mechanism by providing the understanding of several weather factors and their influence on dust retention on reflector surfaces. The author highlighted cementation as the key natural process of soil retention which is accelerated by the presence of high wind speeds and humidity levels. Figure 2.7 shows the natural cementation pro-

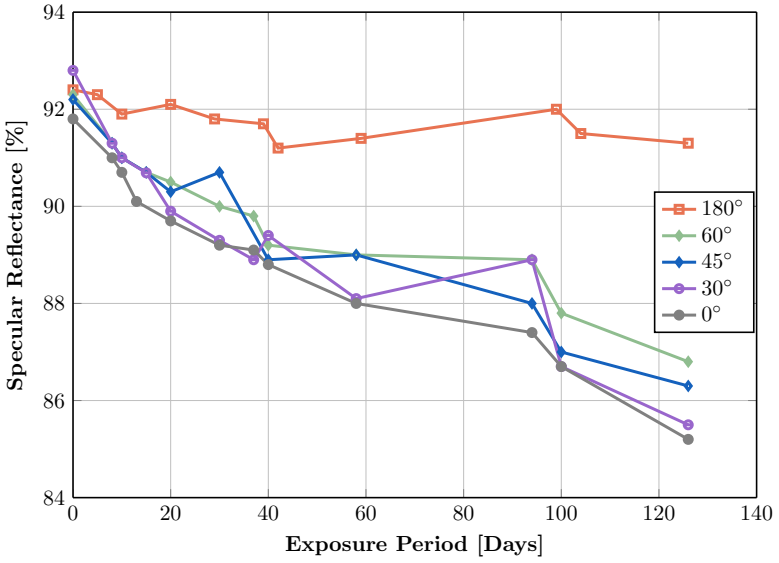

Figure 2.6: Collector degradation as a function of mounting angle(0° =facing up 180° =facing down): Adapted from(Roth *et al.*, 1980).

cess. In other studies conducted to correlate soiling to climatic and weather factors, Deffenbaugh *et al.* (1986) have argued that solar collectors located in semi-arid and desert environment are at higher risk of soiling due to the inadequate amounts of rainfall received in the regions and a high amount of aeolian dust. Their study investigated the spatial nature of soiling by comparing the performance of parabolic trough collectors located in three potential CSP sites in United States, namely; San Antonio, El Paso both in Texas and Lavington in New Mexico. Typical degradation of maximum output reported was 1.3%, 0.7% and 1.3% per day for San Antonio, El Paso and Lavington respectively. A similar study was conducted by Tahboub *et al.* (2013) in two test sites in Abu Dhabi, namely, Al Wagwan and East Jabal Hafeet. They reported weekly drop in solar mirrors specular reflectance of 16.84% and 14.85% for Al Wagwan and East Jabal Hafeet respectively. High soiling rates in Al Wagwan were attributed to the surrounding desert climate. Other than pointing out to the influence and variation of weather and climate to different soiling and optical degradation caused by soiling on reflector surfaces, the relationship between weather influences to these optical losses were under looked.

2.6 The state of art in solar reflectivity measurement

Two methods of measurement of soiling were established by Terrat and Joumard (1990), namely, mass based methods and optical degradation methods. Mass based methods record the amount of accumulated mass with time whereas in an optical based method, the optical degradation, represented as reflectivity in mirrors, is measured with time. Authors such as El-Shobokshy and Hussein (1993) strongly recommend the mass based methods to optical degradation methods although the applicability of their method in reflector surfaces is still questionable.

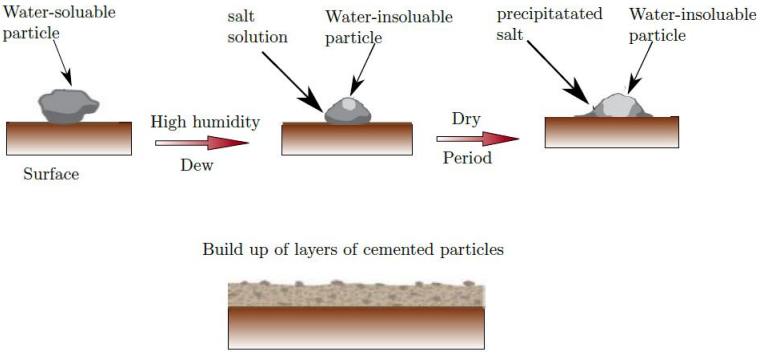

Figure 2.7: Dust moisture cementation process: Adapted from(Cuddihy, 1980).

Currently, a number of portable instruments are used for reflectance measurements to quantify the extent of optical degradation caused by soiling on CSP reflector both in assesment of opitcal state of solar field, and in research such as that conducted by Fernández-Reche (2006); Nelson *et al.* (2011); Ho *et al.* (1995); Pettit *et al.* (1977). These portable devices include: Devices and Services 15R-USB, Abengoa solar Condor SR-6.1, Surface optics SOC 410 and Fraunhofer ISE reflectometer. Figure 2.9 shows these commonly used standard portable reflectometers. These portable devices offer measurements at different incident angles, acceptance angles and different wavelengths of light following different measurement standards. For instance, Devices and Services D&S 15R follows ASTM 173-96[4] while Surface optics SOC 410 follows ASTM E903-97[5].

(a) (b) (c)

Figure 2.8: Standard commercial portable reflectometers. (a) Devices and Services D& S 15R-USB (b) Surface optics SOC 410 (c) Abengoa Solar condor .

Table 2.2 shows device measurement specification comparison for some commercial standard reflectometers based on the results of the studies conducted by Crawford *et al.* (2012) and Meyen *et al.* (2014). Crawford *et al.* (2012) only compared the measurements obtained from three commercial reflectometers, that is, Devices and Services D&S 15R portable reflectormeter, Surface Optics SOC410 and Abengoa Solar Condor. Their findings indicate variable but comparable measurement

[4]Direct measurement of specular reflectance.
[5]Specular reflectance evaluated from the difference of hemispherical and diffuse reflectance.

between D&S 15R portable reflectometer and surface optics SOC410. Variable and inconclusive measurements were obtained from Abengoa Solar Condor and the other two reflectometers. Their study indicates the possibility of different measurement standards leading to different measurements. This can be explained by the different standards followed during the reflectivity measurement.

Table 2.2: Comparison of different portable reflectometer measurement device. Source: Own compilation based on Crawford *et al.* (2012) and Meyen *et al.* (2014).

Device	**Specifications**			
	Iluminated area (mm)	**Acceptance angle**	**Incident angle**	**wavelenght Bandwitdth**
Devices & Services D&S 15R-USB	10	7 mrad 15 mrad 25 mrad 46 mrad	15	570 nm 660 nm
Surface optics 410- Solar	10	105 mrad	20	7 bands in 330-2500 nm
Abengoa Solar Condor SR-6.1	1	408 mrad	25	435 nm 525 nm 650 nm 780 nm 940 nm 1050 nm
Fraunhofer ISE reflectometer 2	12	82 mrad	8	430 730 820-880

The guidelines provided in SolarPACES Task III in search for appropriate reflectometer for CSP application stipulate that, an ideal reflectometer ought to be capable of taking measurement of reflectivity at wavelength between 280-2500 nm in increments of 5 nm and with controllable acceptance angle among other requirements (Meyen *et al.*, 2013). Currently, there is no device in the market that has met these measurement specifications.

Recent research has focused on development of alternative and non-standard methods to characterise the state of reflector optics and optical losses caused by soiling with thee purpose of addressing challenges faced with current standard reflectometers (Griffith *et al.*, 2014; Meyen *et al.*, 2014). Figure 2.9 shows some of reflectometers in research and development phase. Griffith *et al.* (2014) developed a camera based reflectometer to measure the state of specular reflectance of material as well as to capture the composition and distribution of dirt within a reflector surface. Their study used image analysis and discretises color channels from a monochromatic light source to represent specific wavelength of the solar spectrum. Similar studies

conducted by Sutter *et al.* (2013) provides a camera based reflectometer prototype that is capable of extending measurement spot of more than 5 cm at three acceptance angles and three different wavelengths. Meyen *et al.* (2014) developed a device to evaluate the mirror specular reflectance from the mirror specular distribution function[6]. These research based reflectometers seek to address the challenges faced by the current reflectometers in the market.

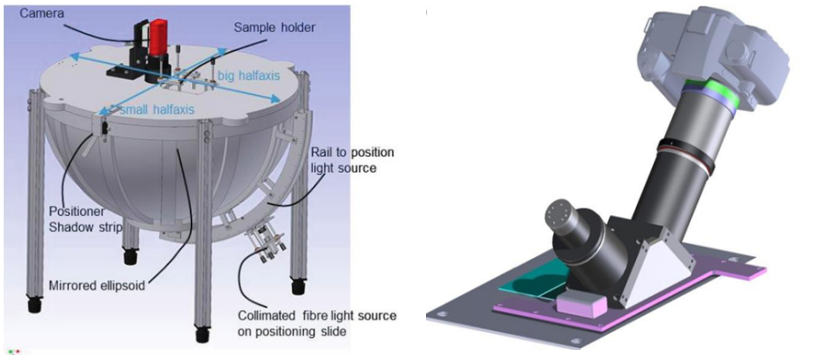

(a) (b)

Figure 2.9: Research based reflectometers. (a). Mirror reflectance function analyser (MIRA). (b) Digital single lens reflex (DSLR) Reflectometer

2.7 Modelling soiling optical losses

Developing a CSP reflector soiling model has been challenged by the complex and spatial variation nature of soiling optical losses, although significant attempts have been made in environmental science to relate the spatial variation of aeolian dust concentration (Shao *et al.*, 2011) and time based variations of soiling (Perez and Reyes, 2006; Alkasassbeh *et al.*, 2013; Kukkonen, 2003). Shao *et al.* (2011) have developed a mathematical earth dust cycle model to estimate the dust variations from one location to another by analytical representation of key parameters involved in emission, transport and deposition processes. Although this study generally provides a basis of understanding the dust cycle processes, they do not focus on the consequences of this atmospheric dust.

Building on the studies carried out by Shao *et al.* (2011), Herrmann *et al.* (2014) developed a solar specific soiling potential model for glazing material in MENA[7] regions using Geographical Information Systems (GIS) by investigating the influence of the soil emission, transport and deposition processes. Their results presented in form of a soiling potential map do not provide a consideration of the extent of dust on different solar technologies and lacks numerical quantification of the soiling potential.

A number of instances of time variation models of aeolian dust suspension has been developed in environmental science with the artificial neural network modelling

[6]Specular distribution function is discussed later in Subsection 3.2.1
[7]Middle East and North Africa

being the key modelling technique. Perez and Reyes (2006) developed a neural network model to estimate a 36 hour concentration of PM10 in Santiago, Chile by observing the key input weather factors contributing to particulate matter concentration with dust concentration as the model output. Similar studies conducted by Alkasassbeh *et al.* (2013) were used to estimate and compare the concentration of soiling materials in three cities across Italy and France. These models shows good relations between weather model input factors to dust concentration although they do not translate the potential of soiling into optical losses caused by these dust materials.

Verney-Carron *et al.* (2012) developed a neural network model to estimate the optical losses on a transmitter glass material exposed to polluted environment with the results showing a good coefficient of determination (R^2=0.88) between the measured and estimated optical losses (Verney-Carron *et al.*, 2012). In other studies modelling effect of dust on transmitter, Massi Pavan *et al.* (2011) developed a neural network to estimate soiled PV performance. The different extent of impact of optical losses caused by soiling are expected from a transmitter to a reflector surfaces. In conclusion, while it remains a challenge to model soiling losses so as to extrapolate the optical degradation caused by soiling from one location to another as well as the variations with time, ANN's have provided a versatile and reliable approach to address the complex nature and the multi- parametric influence of optical losses caused by soiling on reflector surfaces.

2.8 Summary

This chapter reviewed the literature that provided insight into the CSP systems and their working principles, the influence of dust on CSP reflector surfaces, the devices for measuring optical losses and the respective modelling approaches.

Factors influencing the rate of soiling were identified as: human activities, site characteristics, dust properties, weather factors and glazing properties. The focus of this study was on the weather factors.

With CSP being recognized as potential competitive technology to conventional base-load fuels, research to measure model and provide an understanding of the weather factors on reflector soiling has become indispensable.

Chapter 3 presents an experimental process aimed at assessing the optical losses caused by soiling on CSP reflector surface.

Chapter 3

Experimental equipment and procedures

3.1 Introduction

As mentioned in Section 1.3, the aim of the study was to develop CSP reflector degradation assessment method and relate the reflector optical losses caused by soiling to weather factors. This chapter focuses on experimental devices and the procedures followed to obtain experimental data. In Section 3.2, CSP specific solar reflector optical measurement concepts that are necessary for assessing soiling optical losses receive discussion. In Section 3.3 the experimental equipment adopted and tools used in acquiring experimental data are then discussed. Experimental test plans and procedures are then outlined in Section 3.4.

3.2 Soiling optical degradation concepts

As stated earlier, soiling of CSP reflectors leads to scattering reflected light (Vivar *et al.*, 2010; Roth *et al.*, 1980; Sarver *et al.*, 2013) which consequently leads to a substantial loss in specularity or rather the specular reflectance of the reflector surface (Sarver *et al.*, 2013). Measurement of specular reflectance follows specified measurement requirements and procedures.

The measurements requirement for CSP applications are outlined in the guidelines provided in Solar Paces Task III (Meyen *et al.*, 2013). This section focuses on specular reflectance measurement concepts and quantification of optical losses caused by soiling on CSP reflectors.

3.2.1 Characterization of CSP reflector optical losses

When light interacts with matter, it is either transmitted, absorbed, or reflected according to the three corresponding ratios that depend on the wavelength of the light and its material properties (Meyen *et al.*, 2013). The material properties associated with these behaviours are transmittance (τ), absorbance (α), and reflectance (ρ). Usually a combination of these parameters takes place according to the law of conservation of energy following that $\rho + \tau + \alpha = 1$. The transmittance is considered

to be zero for opaque objects. The reflectance of a material is defined as the ratio of the radiant flux reflected from a surface to that of the incident flux (Meyen *et al.*, 2013) as defined in Equation 3.1.

$$\rho = \frac{\phi_{\mathrm{r}}}{\phi_{\mathrm{i}}} \tag{3.1}$$

where: ϕ_i = Incident flux.
ϕ_r = Reflected flux.

Two cases of reflection observed from reflector materials which were outlined in Section 2.6 and different reflector characterization parameters are provided in Meyen *et al.* (2013). As mentioned earlier, specular reflectance, denoted by $\rho_s(\lambda, \theta, \psi)$ gives the reflectance characteristics of a typical CSP reflector material. Understanding the required measurement procedure is vital. On the other hand, the consequence of dust on reflector surface is to increase the scattering effect of light and eventually decrease the mirror specularity/ specular reflectance.

Measurement of specular reflectance for CSP materials follows the measurement vector diagram shown in Figure 3.1 with ρ_s being dependent on wavelength, λ, of the incident light and is a function of the incidence angle, θ as well as (half) acceptance angle, $\psi(\lambda, \theta, \psi)$, associated with detector aperture (Meyen *et al.*, 2013). The specular reflectance of a material is often inferred by intensity of measurement of reflected beam collected through an aperture as shown in Figure 3.1 or measured within field of view of a detector (Sutter *et al.*, 2013). The observed signal is given by Equation 3.3

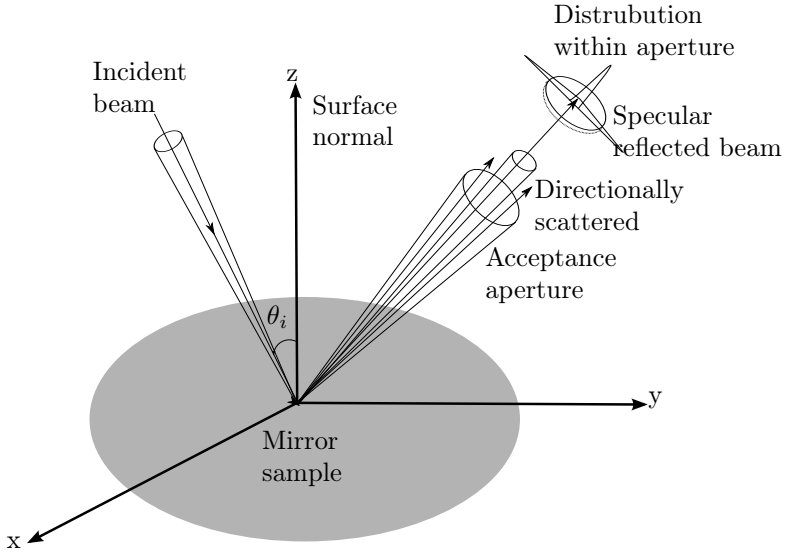

Figure 3.1: Specular reflection vector diagram (Sutter *et al.*, 2013).

$$\rho_{detected} = N \int_{\Omega} \int_{Sbeam} \int_{detector} I(A\overrightarrow{i}) R \left\{ \frac{\overrightarrow{AB} x \overrightarrow{r}}{|\overrightarrow{AB}|} \right\} d\Omega_i dS_{beam} dS_{detector} \tag{3.2}$$

Where N is the normalisation factor, $I(A\overrightarrow{i})d\Omega_i$ represents the beam of intensity I travelling in the direction i and hitting a point A in mirror in a solid cone angle $d\Omega$. B is a point on the detector surface capturing the light scattered along $\overrightarrow{AB}$, whereas S_{beam} and $S_{detector}$ represent the mirror and detector surface respectively.

Equation 3.3 represents the intensity profile of light impinging on the mirror that is then convoluted with a function R according to which light is reflected and scattered by mirror. A second convolution takes place with the function representing the detector aperture capturing the reflected light. Therefore, in general, the measured signal is not a characteristic of a material as is the scattering distribution function, R . Additionally R is dependent on wavelength and incidence angle. Once the reflectance distribution function is known, the acceptance angle ψ is given by:

$$\rho_s(\lambda, \theta, \psi) = \rho_h(\lambda, \theta, h) \int_0^{2\pi} \int_0^{\psi} d\theta d\psi sin\psi R(\lambda, \theta, \psi) \tag{3.3}$$

where R is the reflectance distribution function, $\rho_s(\lambda, \theta, \psi)$ is the specular reflectance at wavelength λ, incidence angle θ and acceptance angle ψ and $\rho_h(\lambda, \theta, h)$ is the hemispherical reflectance at wavelength λ, incidence angle θ over an hemispherical angle h.

In some instances it is easier to characterise the specular distribution function as described by Gee *et al.* (2010) and Pettit *et al.* (1977). This changes Equation 3.3 to:

$$\rho_s(\lambda, \theta, \psi) = \rho_h(\lambda, \theta, h) \left\{ 1 - \sum_{i=1}^{M} K_j exp \left[\frac{-\theta^2}{2\sigma^2(\lambda)} \right] \right\} \tag{3.4}$$

Where K_j is the scattering coefficient, $\rho_s(\lambda, \theta, \psi)$ is specular reflectance at wavelength λ, incidence angle θ, $\rho_h(\lambda, \theta, h)$ is the hemispherical reflectance at wavelength λ, incidence angle θ and over a spherical angle h, and σ standard deviation of reflected light.

In other cases, R may be approximated more adequately by adding an exponential term (Meyen *et al.*, 2014) or even another different approach. Especially for materials with anisotropic scattering functions, appropriate approximation is not defined yet. Under certain circumstances, it is possible to relate Equation 3.3 directly to the intensity measurement for a circular acceptance aperture/detector aperture that is positioned in the exact specular direction. This applies when a highly collimated incidence beam is used and thus $I(A\overrightarrow{i}) = I_0\delta(\overrightarrow{i})$, or when the illuminated area on the mirror is much smaller than the detector aperture, so that it can be considered punctual (Meyen *et al.*, 2013).

The convolution problem might also be avoided by relating the intensity measurement of a sample with unknown R to the intensity measurement of a reference mirror, of which it is known that all the reflected light enters the measurement aperture; thus it has perfect specular quality. Both intensity measurements imply the

convolution of the same components, except for different R. This way, the specular reflectance value at this specific ψ can also be estimated without knowing the R of the sample.

Equation 3.3 and Equation 3.4 relate the specular reflectance to specularity, which describes the beam spread caused by scattering according to R. A mirror with perfect specularity has no scattering or beam widening. In that case the beam spread is zero and $\rho(\lambda, \theta, \psi)$=$\rho(\lambda, \theta, h)$. regardless of the acceptance. In CSP systems, the actual impact of reduced specularity must be evaluated considering other optical errors in the system.

3.2.2 Soiling degradation concepts

There are various mechanisms leading to optical degradation on CSP reflector surfaces outlined in Cuddihy (1980). Kattke and Vant-Hull (2012) have summarized soiling optical degradations into two independent leading processes identified as film growth and dust deposition respectively. The rate of occurrence of these processes was then mathematically translated into optical losses caused by soiling (Kattke and Vant-Hull, 2012).

Optical soiling caused by soiling reflector surfaces are defined by the soiling rate (Kattke and Vant-Hull, 2012). Soiling rate is defined as the change in reflector cleanliness over a specified period of time (Heimsath *et al.*, 2014), usually between two successive cleaning events. Equation 3.5 provide the expression of soiling rate. Soiling rates are significantly variable depending on seasonal air quality which is affected by variation in weather.

$$R_{Soil} = \frac{dC}{dt} \tag{3.5}$$

The fraction of clean reflectance lost due to soiling follows a functional form 1-e^{-ft} where R_{soil} is the soiling rate and t is the time since the last cleaning. The reflectance loss caused by soling is given by Equation 3.6.

$$\Delta\rho_{soil} = \rho_{clean}(1 - e^{-R_{soil}t}) \tag{3.6}$$

Optical loss caused by soiling on reflector surfaces has recently been expressed in terms of reflector cleanliness (Merrouni *et al.*, 2015) which is defined as the fraction of clean[1] reflector reflectance lost due to soiling. This is expressed as the ratio of specular reflectance of the soiled mirror to that of the clean mirror as shown in Equation 3.7. This measure eliminates the optical degradation caused by reflector ageing, assuming that the reflectance of the clean reflector remains constant before successive cleaning.

$$Cleanliness\ (C) = \frac{\rho_{soil}}{\rho_{RefC}} \tag{3.7}$$

Routine measurements of optical losses due to soiling in plant operation aim to find the level of cleanliness in which the reflector specular reflectance would fall below the optimum level for optimum plant operation. Time based degradation of

[1]Reflectance the surface is returned to after removal of respective soiling mechanism

a reflector surface is expressed in terms of the soiling rate (Caron, 2011; Kattke and Vant-Hull, 2012).

3.3 Experimental equipment and samples

The section describes the experimental equipment, tools and samples used to carry out the experimental procedures.

3.3.1 Real- Time Cleanliness Monitoring Sensor (RCMS)

Devices used to measure and assess soiling optical losses and the challenges facing them were discussed in Section 2.6. These devices offer measurements at a particular instant and measurements obtained from them are rather tedious, and the assessment is usually done through sampling. Due to the nature of the experiment for this study, there was a need to develop a punctual method to asses a CSP reflector optical losses caused by soiling, and at the same time, relate these soiling degradation measurements to the corresponding weather factors same the time step. Although monitoring mirrors and sensors was recently proposed by Wolfertstetter (2013), there is currently no commercially available device that provides real time measurement of reflector optical losses caused by soiling. Real time monitoring cleanliness sensor evaluates CSP reflector soiling optical losses by mimicking the reflector performance under normal working conditions.

The working principle of real- time cleanliness monitoring sensor makes use of a well established measurement equipment. An existing meteorological station at Stellenbosch University used in solar resource assessment was used as the basis for installation of the real time cleanliness monitoring set up. Typical solar resource assessment at a meteorological station usually consist of two pyranometers for measuring diffuse horizontal irradiation (DHI) and global horizontal (GHI) and one pyrheliometer for measurement of direct normal irradiance (DNI). A real time cleanliness monitoring sensor set up was installed as an accessory on the same tracker, with a second pyrheliometer (RCMS) modified such that it faces backward at an angle into a mirror that reflects direct solar irradiance into the RCMS pyrheliometer as shown in Figure 3.2. This device is capable of providing the real time optical state of a typical CSP reflector.

I. Overview of components

As mentioned earlier RCMS made use of existing radiometric assessment devices with additional, manufactured devices to modify the existing device to adapt for reflector soiling optical loss assessment. Figure 3.3 shows the RCMS device that was installed at Stellenbosch University Sonbesie weather station. Details of the pyrheliometer mounting on the measuring section are as shown in Figure 3.4. The existing components forming the measurement set-up include pyrheliometer and sun tracker. More detailed pictures of the device construction are provided in Appendix C. A new Kipp & Zonen pyrheliometer CH1 was acquired. A new set of pyrheliometer mounting Clamps, mirror mounting plate, mirror mounting rod and a tracker mirror mounting bracket were manufactured as the accessories for the RCMS measuring

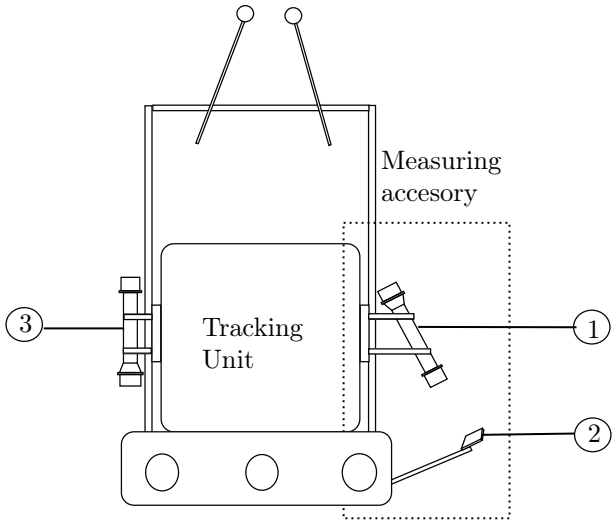

Figure 3.2: Plan view of absolute solar reflectance measurement device. 1. Measuring pyrheliometer 2. Mirror sample 3. Reference pyrheliometer

section. Figure C.1 in Appendix C shows the RCMS manufactured accessories. A description of the specification of the components forming the RCMS set up is provided below.

Figure 3.3: Real time cleanliness monitoring device installation.

(a) Kipp & Zonen CH 1 pyrheliometer

Both pyrheliometers used in the cleanliness measurement set up were Kipp & Zonen CH1. Kipp & Zonen pyrheliometers employ a thermopile sensor located at the back of a tube housing that defines the opening angle of the instrument. One

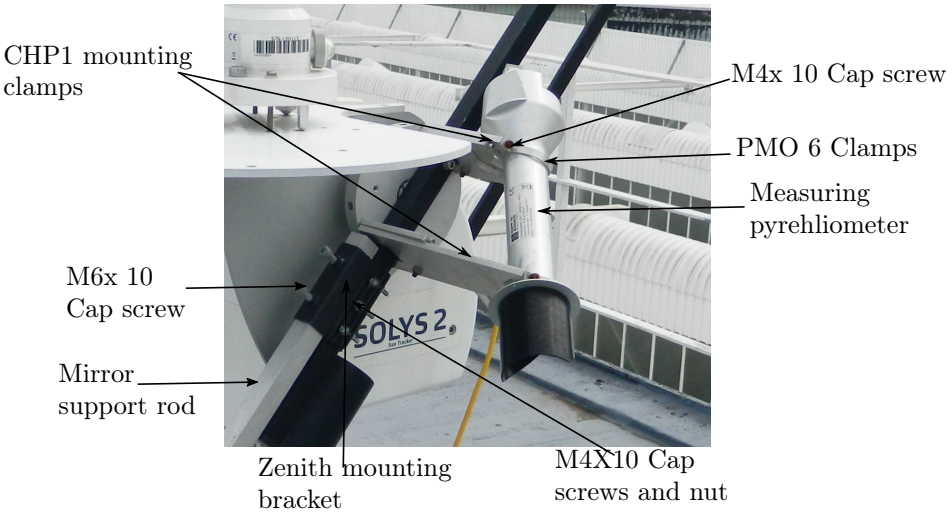

Figure 3.4: Measuring section, pyrheliometer mounting and mirror mounting.

side of the thermopile consists of a blackened surface where the solar radiation is completely absorbed, independent of the wavelength of the incoming light (Kipp & Zonen, 2001). The calibration of the incoming solar irradiance measured results from the temperature difference between the solar heated thermopile and the interior of the pyrheliometer body. Measurement and calibration follows ISO 9060 standard.

The manufacturer designated opening angle for this device is 5° (Kipp & Zonen, 2001). This implies that the pyrheliometer receives radiation from a region which is at 5° around the center of the sun in the case of perfect tracking. Deviations from the optimum angle cause the percentage of received light to decrease following the penumbra function as described in Major (1994). The manufacturer designated total uncertainty for the measurement of DNI while tracking the sun perfectly is given as 1% for daily total values and 2% for hourly total values. Other device ISO specification are provided Appendix A.1.

(b) SOLYS 2 sun tracker

The meteorological solar tracker utilised in this experimental set up was Kipp & Zonen SOLYS 2 tracker. Figure C.4 and Figure C.5 in Appendix C shows the device sitting area and minimum required operating area respectively. This two axis sun tracker platform is integrated to a regularly updating GPS in order to configure the location and time in a specialized manner. This ensures that the instrument accurately tracks the sun's position during its movement across the sky under any weather conditions. According to the device manufacture, this device is capable of providing a tracking accuracy of better than 0.1° with passive tracking (Kipp & Zonen, 2011).

The Kipp & Zonen SOLYS 2 sun tracker installed at Sonbesie Weather Station in Stellenbosch is equipped with the Kipp & Zonen sun sensor for active tracking. This improves the tracking accuracy to better than 0.02°. Other device specifications for Kipp & Zonen SOLYS 2 sun tracker are provided in Appendix A.2.

(c) Pyrheliometer mounting clamp

The angle provided in the measuring pyreliometer in RCMS is determined by the design of pyrheliometer mounting clamps. A pair of pyrheliometer mounting clamps, parts 4 and 5 in Figure C.1 in Appendix C were manufactured from 6 mm thick aluminium plate. The 100 mm distance of separation provided in the SOLYS 2 sun tracker side mounting plate was used as the reference dimension to provide an outward angle of 45° from basic trigonometric calculations between the heights of the two clamps on which the pyheliometer circumference should rest. The dimensions of the two mounting clamps are 198 x 63.4 mm and 98 x 63.4 mm respectively. The height difference of 100 mm was provided between the two clamps. Other features of the two brackets are a 25 x 25 mm notch centrally cut on one side of the width. This notch provides the opening for the shading ball drive arm. The second side of the width was a centrally cut half octagonal notch of side 19.6 mm. Figure E.1 and Figure E.2 in Appendix E show the CAD drawing for the two manufactured mounting clamps showing the details and dimension of the key features.

(d) Mirror support unit

The mirror mounting unit consist of three parts; mounting bracket, mounting support rod and mirror mounting panel. Figure C.1 in Appendix C shows the manufacture parts forming the mirror support unit. The mounting bracket provides clamping of the mirror support arm to the shading ball drive arm. The mirror support rod then provides the mounting of the sun tracker on the mirror mounting panel. The mirror mounting panel is used for placement of the sample mirror while ensuring that there is some movement to ensure that different measuring spots can be taken. A detailed description of these parts and the their specification are provided in Section C.2 in Appendix C.

(e) Mirror panel sample

Due to material availability, the scope of the study was reduced to second surface silvered glass mirrors. Figure 3.5 shows a typical construction of second surface glass mirror. Typical design criteria for solar mirrors dictate making the thickness of the cover glass as small as possible so as to minimize double absorption during the transmission of the incident solar radiation over as wide a spectrum as possible and still withstand the strength specification or other requirements for a particular application (Czanderna *et al.*, 1985). Figure B.1 in Appendix B shows the typical variation of mirror specular reflectance with thickness for different glass mirrors.

Figure 3.5: Construction of typical mirror structure.

The mirrors used were typical 3 mm silvered glass mirrors with protective back. The mirrors were supplied by PG Glass Stellenbosch. According to the manufacturer, these mirrors were manufactured through by vacuum evaporation process [2].

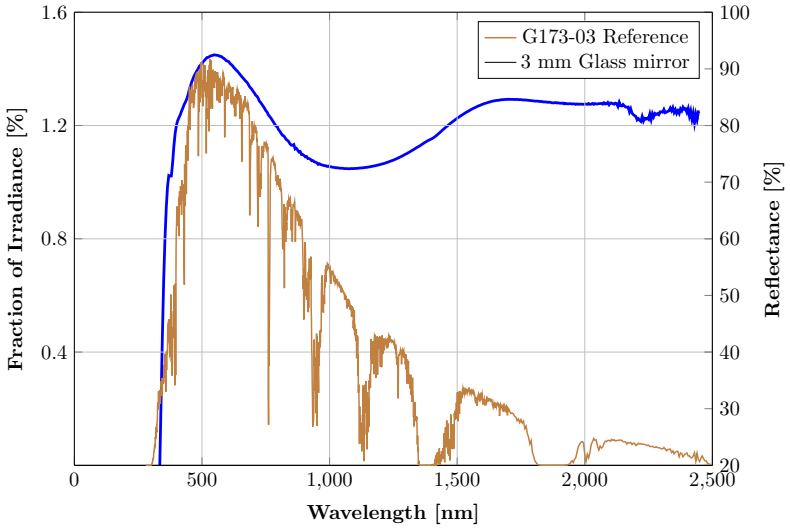

Figure 3.6: PG 3mm Glass reflectance over spectral distribution (Hugo, 2015)

The solar weighted hemispherical reflectance for the mirror samples were evaluated according to ISO 9050 standard is 83% using a Perkin Elimer Lambda 950 spectrometer (Meyen *et al.*, 2013). Figure 3.6 shows the distribution of reflectance over the solar spectrum wavelength alongside the standard ISO G173-03 solar weighting spectrum. A decreasing reflectance in wavelength of about 550- 1500 nm observed in Figure 3.6 is due to the double absorption of light (Czanderna *et al.*, 1985) caused by the iron content in cover glass.

The mirror sample was cut into a 100 x 100 mm sized square. The size was chosen to be large enough to illuminate the pyrheliometer's aperture window as well as the pinhole mounting control system at its top. Furthermore, the mirror surface covers the complete imaginary area defined by the limit angle of the pyrheliometer and the working distance. Additional mounting was done to ensure that the mirrors could easily be mounted on the reflectance measuring device during cleanliness measurement. A 3.5 mm steel sheet cut into a 30 x 100 mm strip is bent into a L- shape with a 4 mm hole to provide mounting to RCMS. This strip was mounted at the back of the mirror using adhesive glue. Figure C.3 in Appendix C shows the mirror sample construction.

II. Measurement and calculation of mirror cleanliness

Cleanliness as obtained from the real- time cleanliness sensor was inferred from the absolute solar specular reflectance which is defined as solar specular reflectance ob-

[2]This a thin film deposition process where the vacuum allows vapour particles to travel directly to the target object (substrate), where they condense back to a solid state. Evaporation is used in micro fabrication, and to make macro-scale products such as metallized plastic film.

tained using the natural sun's spectrum as the source of light at the present geometry of direct solar radiation and atmospheric conditions (Wolfertstetter *et al.*, 2012). Measurement of absolute solar specular reflectance followed the specular reflectance measurement vector diagram shown in Figure 3.1.

From the RCMS, since the pyrheliometer measures the direct component of solar radiation, DNI, the measured DNI signal from the measuring pyrheliometer represents the specularly reflected solar radiation from the mirror sample (DNI_r). The signal measured from the pyrheliometer measuring directly from the sun represents the incident solar radiation denoted, (DNI_{sun}). The ratio of the reflected signal from the measuring pyrheliometer to that of incident measurement signal represents absolute solar specular reflectance ($\rho(\theta, \psi)$). Mathematical representation of solar absolute specular reflectance is as shown in Equation 3.8.

$$\rho_{abs}(\psi, \theta) = \frac{1}{N} \sum_{n=1}^{N} \frac{DNI_r(t_n)}{DNI_{sun}(t_n)} \tag{3.8}$$

From Equation 3.7, soiling losses are represented as a fraction of soiled mirror to that of clean mirror reflectance (Merrouni *et al.*, 2015). Solar absolute specular reflectance of a clean mirror over a time span t_n in which N measurement values were taken, in a mirror state that can be considered clean and preferably in clear sky conditions were used as the calibration factor for soiling optical losses. This calibration factor obtained before each soiling test was calculated from Equation 3.9 and is assumed to remain constant[3] for the exposure period before the successive cleaning routine.

$$\rho_{clean} = \frac{1}{N} \sum_{n=1}^{N} \frac{DNI_r(Clean, t_n)}{DNI_{sun}(t_n)} = C_{clean} = Constant \tag{3.9}$$

The cleanliness at any other time after the exposure period (T) is obtained by multiplying the inverse of calibration factor C_{clean} with the cleanliness obtained after the exposure period (T) as shown in Equation 3.10

$$\text{Cleanliness } (C) = \frac{1}{N} \sum_{n=1}^{N} \frac{DNI_r(Soil, t_n)}{DNI_{sun}(t_n) x C_{clean}} \tag{3.10}$$

III. Measurement uncertainties

Measurement errors and uncertainties are inherent features of the performance of the instrumentation used to take the measurements and the measurement procedures themselves. Knowledge of measurement uncertainty and error analysis can be used to determine the quality of the measurements and can be used to eliminate noise or rather noisy data in a measurement set. The error of a measurement is defined as the deviation of a measured value of a physical quantity and the actual or true value (Beckwith *et al.*, 2007). When the absolute error between the actual and the true

[3]Assumed that optical losses during single exposure period occur only due to soiling and not ageing or abrasion caused on mirror.

value of the measured quantity is too large, the measured value becomes meaningless and is referred to as noise (Bevington and Robinson, 2003).

Bevington and Robinson (2003) outlined two categories of errors in physical measurements as precision errors and systematic errors. Systematic errors are those errors that occur in a consistent way each time a measurement is made. Systematic errors are identified and eliminated through device calibration. It is difficult to completely eliminate systematic errors as most of calibrations references carry errors with them as well. Precision is defined as a measure of how well a measurement has been determined without reference to its agreement with the true value. Precision is also a measure of reproducibility of a certain measure in an experiment (Bevington and Robinson, 2003). An experimental measure is said to have precision error if it is not reproducible. Precision errors are eliminated using statistical analysis, if enough measurements are taken, and they will generally cluster about a central value, only extending over a short interval surrounding that central value.

Potential causes of systematic errors include: improper mirror alignment and improper calibration of the measuring device. Different mounting positions of the mirror were tested to eliminate mirror mounting error. The measuring pyrheliometer was also recently calibrated by the manufacturer. The incident measurements were compared to this previously calibrated pyrheliometer. Calibration of optical losses caused by soiling was done following a similar procedure followed by Wolfertstetter *et al.* (2012) according to Equation 3.9. Potential causes of precision errors include fluctuation of incident radiation intensity over time, circumsolar radiation effects [4], fluctuation of environmental conditions and potential soiling of the pyrheliometers during the measurements. The manufacturer's routine maintenance procedures regarding daily cleaning of pyrheliometer were followed during the experimental period.

3.3.2 Outdoor exposure site

The experimental test site is located in the Sonbesie Weather Station on the roof of the Civil Engineering building in Stellenbosch University, located in Stellenbosch, South Africa. The GPS coordinates of the station are 33.9200° S, 18.8600° E and it is located at an elevation of 119 m above sea level. Figure F.1 in Appendix F shows the location map of the Sonbesie Weather Station. The choice of location was based on its vicinity, availability of the pre- installed weather station and the potential usefulness of the soiling data to the Helio 40, CSP research project located on the adjacent Mechanical engineering building roof top.

Stellenbosch and the its surroundings experience a Mediterranean climate with an average annual rainfall of about 800 mm per annum (Bonnardot *et al.*, 2002). Maximum precipitation occurs during winter, specifically in the months of May, June and July. High wind velocities are experienced during autumn and spring while high levels of humidity are witnessed during spring and summer. A yearly average of these weather factors of Stellenbosch obtained over the previous five years is provided in Appedix F. Medium soiling rates were expected as most of the roads in the surrounding area are paved, with construction around the Engineering building during

[4]Noring *et al.* (1991)

the experimental period the likely human activity with a potential of increasing the soiling rates. These soiling rates were expected to vary over the course of the year due to seasonal variations of weather factors. Nevertheless, high aeolian suspension was expected during summer and autumn with low to medium suspension expected during winter and spring.

3.3.3 Meteorological data acquisition

As mentioned in Section 3.3.1, there was an existing meteorological station in the experimental site and relevant meteorological data was recorded throughout the experimental exposure period. Necessary meteorological data recorded included, wind speed, wind direction, ambient temperature, relative humidity and solar resource measurements. Wind speed and wind direction were measured using a Campbell Scientific 03001 R.M. Young wind sentry set. This probe consists of a 03101 R.M. Young wind sentry anemometer and a 03301 R.M Young wind sentry vane. The anemometer is capable of measuring wind speeds in the range of 0-50 m/s while the wind vane measures angular direction in the range 0°-360° using North as the installation reference. The measurement accuracy of wind speed and wind direction is provided by the manufacturer as ± 0.5 m/s and and ± 5° respectively (Campell Scientific. Inc, 1996).

Similarly, a single probe measuring both temperature and relative humidity was pre- installed in both sites. The installed probe in both sites was a Campbell Scientific CS215, 41303-5A, measuring temperature in the range -40°- 70°C and relative humidity in the range 0-100%. The accuracy of temperature measurement provided by the manufacturer is ± 0.3°C (Campell Scientific. Inc, 2015). The accuracy of measurement of relative humidity is dependent on the temperature and is provided as ± 4% in the range 0-100% and ± 2% in the range 10-90% at 25°C (Campell Scientific. Inc, 2015). Figure 3.7 (a) shows the installed meteorological measuring devices, where, Figure 3.7 (b) shows the wind measurement probe which consists of an anemometer and a wind vane, while Figure 3.7 (c) shows the installed temperature and relative humidity measuring probe.

All the solar resource measurements were obtained from a single unit as one described in Section 3.2.1. In each of the solar resource measurement unit at least two Kipp & Zonen CMP 11 pyranometers and at least one pyrheliometer had been installed on a Kipp & Zonen Solys 2 sun tracker. One pyranometer measured global horizontal irradiation(GHI) while the second consisted of a shading ball as an accessory to enable the measurement of diffuse horizontal irradiation (DHI). The uncertainty in the measurements obtained by the pyranometers was ± 2% for daily total and ± 3% for hourly total (Kipp & Zonen, 2001). A description of the specifications of Kipp & Zonen CHP 1 pyrheliometer and Solys2 tracker were provided in Section 3.3.1.

Table 3.1 provides a summary of the recorded meteorological quantities, measurement device and accuracy of measurements. Detailed information of the specifications is provided in Appendix A. The device installation architecture in the test location is shown in Figure F.2 in Appendix F.

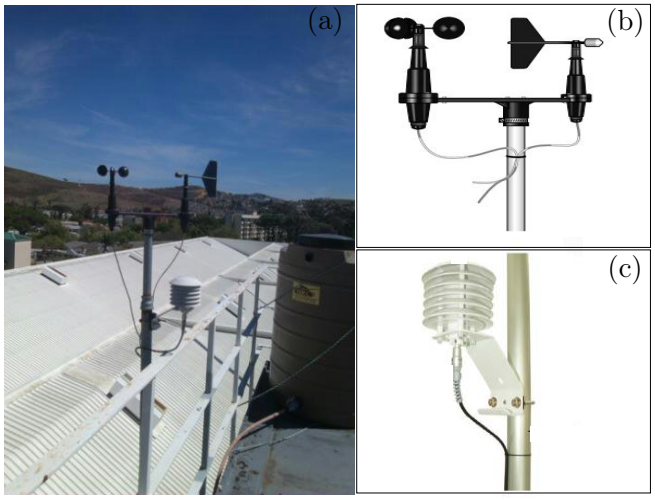

Figure 3.7: Installed meteorological device

Table 3.1: Recorded meteorological quantities and specification

Quantity	**Device specification**	**Accuracy range**
Wind speed	03101 R.M. young wind sentry anemometer	± 5° (0-50m/s)
Wind direction	03101 R.M. young wind sentry vane	± 0.5 m/s (0°-360°)
Temperature	Campbell Scientific CS215	± 0.3°C
Relative humidity	Campbell Scientific CS215	± 4% (0-100%) ± 2% (10-90%)
DHI	Kipp & Zonen CMP 11	± 3% hourly total ± 2% daily total
DHI	Kipp & Zonen CMP 11 with shading ball	± 3% hourly total ± 2% daily total
DNI	Kipp & Zonen CHP 1	± 2% hourly total ± 1% daily total

3.4 Test plans and procedures

This section describes the experimentation strategy followed to collect experimental data. Proper test plans and procedures were followed in order to ensure adequate experimental data was available with minimum number of tests.

3.4.1 Experimental design

Appropriate experimentation design was vital to obtain adequate experimental data to relate the influence of weather factors to optical degradation caused by soiling on the CSP reflectors. At the same time, adequate data to develop a neural network model to estimate soiling losses was required in order to avoid using unnecessary data.

The experimentation strategy to achieve the objective of this study required the following:

- Determining weather parameters influencing soiling.
- Defining exposure period.
- Selecting data time step
- Experimental planning.

Determining weather parameters influencing soiling

Optical loss caused by soiling on CSP reflectors is affected by a number of parameters as discussed in Subsection 2.5.2. Similarly a number of weather factors influence the optical loss caused by soiling on reflectors (Mani and Pillai, 2010). The first strategy referred to as "intuitive approach" consist of selecting a number of weather factors that can be used to describe the the rate of soiling and consequently optical losses caused by soiling. This strategy does not require planning effort although its a vital to ensure that any weather parameter influencing optical losses is fully investigated. The second strategy was to investigate the factors that directly influence the rate of soiling with optical loss caused by soiling on CSP reflectors so as to describe the relationship between time series optical loss variation between these weather factors. The weather factors identified to directly influence soiling rate and in turn optical loss caused by soiling include: wind speed, humidity and rainfall.

The third strategy was to establish a correlation between the weather factors directly and indirectly influencing the rate of soiling to optical loss caused by soiling. This strategy removes the time series variation and seeks to correlate the optical losses caused by soiling to weather factors by assuming other factors remain constant to establish which weather factors best describes the optical losses caused by soiling. The understanding of the interaction of weather factors and how they vary with time was required to accomplish this strategy. The final experimental strategy was to combine the effect of weather factors to develop a time series neural network model relating optical losses of the reflector to a set of weather factors directly and indirectly influencing the rate of soiling. A detailed description of this strategy is discussed in Chapter 4.

Defining exposure period

Optical degradation caused by soiling on CSP reflectors is considered as a time function of multiple factors that lead to emission transport and soil deposition (Mani and Pillai, 2010) and consequently the time variation of soiling. This study seeks

to relate to the variation of weather factors with time. Selecting an appropriate exposure period was fundamental to understand the variation over a fixed period of time. The exposure period for the experiment was defined as the period between two successive cleaning periods (Heimsath *et al.*, 2014). The strategy followed to obtain the exposure period was based on the relevance of the optical loss after each of the exposure period. Two exposure periods were selected, that is, a weekly and a monthly exposure period, depending on the required data. The choice was based on the fact that medium soiling rates were observed at the test site.

Selecting data time step

The recorded experimental data was available in three time steps, that is, minute, hourly, and daily averages. Apart from cleanliness, the averages of other meteorological parameters was obtained as recorded from the devices. To evaluate cleanliness, a consideration of measurement uncertainty discussed in Subsection 3.3.1 had to be taken into account. Due to the high limits of DNI measurement required to evaluate cleanliness, the values of cleanliness were evaluated from minute DNI measurement data.

Experimental planning

Once the exposure period had been defined, it was necessary to define the manner in which the experiments were carried out. The experiment plan ensured that the end of each of the experimental tests coincided. The purpose was to ensure that there was no interruption of any test during cleanliness measurement since a single cleanliness measurement device was used for the test. This was achieved by ensuring that the selected exposure period coincide during successive period of testing.

3.4.2 Experimental procedure

The experimental procedure followed in order investigate the optical loss due to soiling under natural soiling conditions can be divided into four stages which were repeated after every pre- defined exposure period:

- Stage 1: Preliminary cleanliness measurement uncertainty test.
- Stage 2: Cleanliness measurement before exposure.
- Stage 3: Soiling degradation test.
- Stage 4: Cleanliness measurement after exposure.

Preliminary cleanliness measurement uncertainty tests (Stage 1)

Before the soiling test was carried out, several measurement uncertainty tests were conducted to establish and eliminate potential sources of errors from the developed RCMS device. The first test was to calibrate the two pyrheliometers in the RCMS. One of the two pyrheliometers was recently calibrated by the manufacturer and was used as a calibration reference for the other one. The two pyrheliometers were

mounted to measure DNI under direct sunlight over a period of two days and the two measurements obtained compared. The second test investigated the variation of mirror cleanliness with the value of measured DNI. Mirror cleanliness obtained during a partly cloudy day was related with the corresponding DNI value to determine the clustering pattern of cleanliness.

To determine mirror mounting accuracy required in the mounting plate, a clean mirror in the mirror mounting was placed imperfectly in four different positions of the systems and the values of cleanliness obtained. Two pinholes in the pyrheliometer indicate a perfectly aligned sun center if the light falling on the upper pinhole hits the bottom pinhole (Kipp & Zonen, 2001). According to the pyrheliometer manufacturer, the device should be pointed at the sun with a deviation not less than 0.75° from it's center (Kipp & Zonen, 2001). This implies that the light spot from the measuring mirror should not deviate by more than 2 mm from ideal position. Figure 3.8 shows different mirror position and the light alignment with the pyrheliometer pinhole from which different measurement were taken and recorded. The final preliminary test to eliminate measurement errors was conducted to investigate the influence of pyrheliometer soiling on measurement values. Ten minute measurements were carried out before and after cleaning both measuring and incident pyrheliometers and the results of variation between clean and dirty pyrheliometer were recorded.

(a) Pos 1. **(b)** Pos 2. **(c)** Pos 3. **(d)** Pos 4.

Figure 3.8: Light spot reflected by mirror as seen from the pinhole for the four different mirror positions.

Cleanliness measurement before exposure (Stage 2)

Soiling losses were inferred from the percentage of degraded clean reflectance and knowledge of initial cleanliness. Thus, the cleanliness factor was vital before outdoor exposure of the mirror to soiling. The front surface of all mirrors samples was first cleaned with demineralised water to remove any loose dirt on its surface. The surface was then thoroughly cleaned with acetone solution using a piece of soft cotton and then polished with a soft dry piece of cotton. To test the initial cleanliness of the mirror, the mirror was placed and moved across the mirror mounting into 4 different positions for 5 minutes in each position during a clear sky day. 20 measurements values were thus obtained. The initial cleanliness/cleanliness factor was obtained as the average of these 20 measurements using Equation 3.9.

Soiling degradation test (Stage 3)

After the initial cleanliness of the mirror was known, the next step was to expose the mirror to outdoor degradation under natural conditions. The mirror was fixed on the RCMS and the variation of cleanliness with time was recorded into the data logger. Meteorological measurements described in Subsection 3.3.3 were measured simultaneously during the entire exposure period taking into account the measuring accuracy and error margins outlined in Table 3.1.

Cleanliness measurement during and after exposure period (Stage 4)

Measurement of cleanliness at any other period during and after the designated exposure period followed Equation 3.10. It is worth mentioning that two sources of missing cleanliness data were experienced during the experimental period. Cleanliness measurement was terminated for the period between March 26- April 16 when loose support damaged the tracker and had to be fixed again. Similarly, during some cloudy days, the cleanliness DNI measurement limits were not observed. These recordings were excluded during data analysis.

3.4.3 Safety precaution

It is important here to highlight potential hazards associated with experimental procedures that were followed. As previously noted, the experimental work was carried out at Sonbesie weather station located on the roof of the Civil Engineering building, Stellenbosch University. The set up and experimental work followed the laboratory safety procedures outlined in by the Department of Mechanical and Mechatronic engineering, Stellenbosch university (2012).

The potential health and safety risks associated with the experimental work relating to the experimenter and the people in the proximity were identified in order to minimise or eliminate the chances of these risks. The key experimental risks and their mitigation procedures were as follows:

- Like any other radiometric station, Sonbesie Meteorological Station is located at the top of a building. This posed a potential risk of falling from height. The radiometric station is protected with a fence and appropriate personal protective equipment (PPE) was worn during experiment to minimize injuries in case of fall.
- There was a potential of reflection from the mirror sample to surrounding offices in Mechanical and Mechatronic building and the solar roof. This was addressed by resetting the tracker and observing the motion of reflection coming from the mirror sample with the tracker movement. Protective sun glasses were worn all the time during the experimentation process.
- Injuries to the experimenter while setting up the real time measuring device, with a potential of cuts from sharp mirror edges. Protective gloves were worn during setting up and any other time working on the experimental set up.

3.5 Summary

This chapter presents the design of the experimental equipment and procedures followed in obtaining experimental data. While monitoring mirror and sensor were recently proposed by Wolfertstetter (2013), there is currently no commercially available device that provides real time measurement of reflector optical losses caused by soiling. As part of the aim of the study, a device termed as real time cleanliness sensor (RCMS) was developed. The procedures for error analysis and calibration of RCMS were described in this chapter. Four experimental design strategies were followed, namely: (i) determining weather parameters influencing soiling; (ii) defining exposure period; (iii) selecting data time step; and (iv) experimental planning.

To augment the analysis of optical losses caused by soiling on CSP reflector surfaces, Chapter 4 discusses the neural network modelling.

Chapter 4

Modelling reflector optical losses

4.1 Introduction

Extrapolating soiling variations experienced in CSP reflector surfaces has not been successful and measured optical losses are only applicable in the specific site and at specified period of time (Sayyah *et al.*, 2013). The complex nature of soiling and challenges facing measurement of optical losses caused by soiling in CSP applications has been the major challenges facing modelling of soiling optical losses. Recently, neural network model have been developed to estimate optical losses caused by soiling with great success (Verney-Carron *et al.*, 2012).

Generally, two variations of optical losses are experienced in the CSP field; time variation of soiling and site variation. The parameters influencing these variations were previously outlined in Subsection 2.5.2. This section provides the modelling concepts and procedures followed to come up with time estimation of optical losses caused by soiling on CSP reflector surfaces. Section 4.2 provides a brief review of artificial neural networks. The procedure followed in the implementation of neural networks to estimate CSP reflector time variation optical losses is outlined in Section 4.3. Modelling tools used in development of the neural network are also discussed in Section 4.3.

4.2 Modelling approach

As outlined in Section 2.7, recent attempts in environmental science have provided a breakthrough in the estimation of variations of suspended particulate matter with time by relating these variations with weather variations using neural networks. Of particular interest is the study carried out by Verney-Carron *et al.* (2012), to related the translation of this suspended particulate matter to optical losses of transmitter using multi- layer feed forward (MLFF) neural networks. This section discusses the working principles of neural network, with particular focus on MLFF, which was adopted in development of neural network to estimate CSP reflector optical losses.

4.2.1 Neural network modelling

Artificial neural networks (ANN's) are networks of simple processing elements (called neurons) operating on their local data and communicating with other elements (Svozil *et al.*, 1997). ANN's simulates the human brain learning system and are able to determine an input-output relationship for complex linear or non-linear systems within a multidimensional information domain. In principle, an ANN has the power of a universal approximator, which is capable of mapping one arbitrary vector space onto another (Svozil *et al.*, 1997). ANNs makes use of some unknown prior information in data in mathematical formalism in such a way that some conditions are fulfilled through a process referred to as learning.

There are many types of neural network, as outlined in Haykin and Network (2004), but the basic principles are similar. ANNs are categorised in terms of learning process into supervised and unsupervised training. Supervised training means that one knows the desired output and weight coefficients can be adjusted in such a way that the calculated and desired outputs are as close as possible (Haykin and Network, 2004). An example of supervised training is followed in multi layer feed forward neural network (MLFF) (Svozil *et al.*, 1997). Unsupervised training means that the output is not known and the system is given a group of facts and then left to settle into a stable state in some number of iterations. An example of unsupervised neural network is the Kohonen network (Svozil *et al.*, 1997). In this study multi layer feed forward neural network was adopted and is described in Subsection 4.2.2.

4.2.2 Multi Layer Feed Forward (MLFF) network

Among all the neural networks outlined in Haykin and Network (2004) and Svozil *et al.* (1997), the multi layer feed forward (MLFF) neural network is the most widely used network due to its ability to tackle a vast number of complex problems (Svozil *et al.*, 1997). As with any other neural network, MLFF consists of an input layer, a hidden layer(s) and an output layer, with each of these layers consisting of a number of nodes/neurons. Figure 4.1 shows a typical single output, single layer neural network with four inputs.

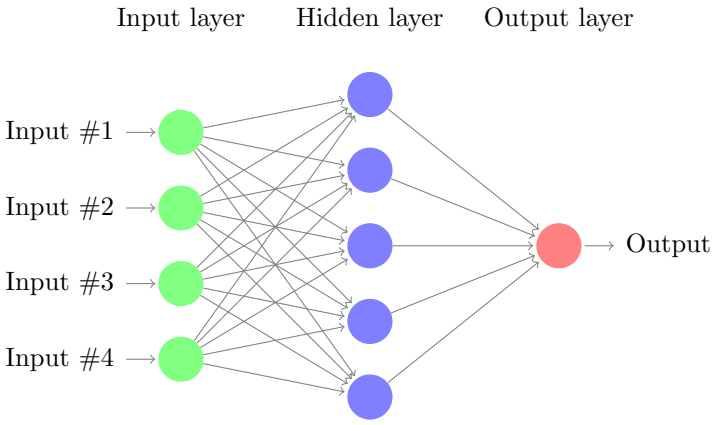

Figure 4.1: Typical neural network system with a single output.

A neuron is defined as the building block of a neural network (Saberian *et al.*, 2014). Each neuron is connected to at least one neuron and each connection is evaluated by real numbers in order to determine the degree of importance of each connection to the neural network output. The communication between two neurons is characterised by a summing junction, weight coefficient, transfer function and a threshold (Haykin and Network, 2004). Each neuron in the network is able to receive input signal process it and then send an output signal (Svozil *et al.*, 1997). Figure 4.2 shows a typical information processing flow map in a neural network system.

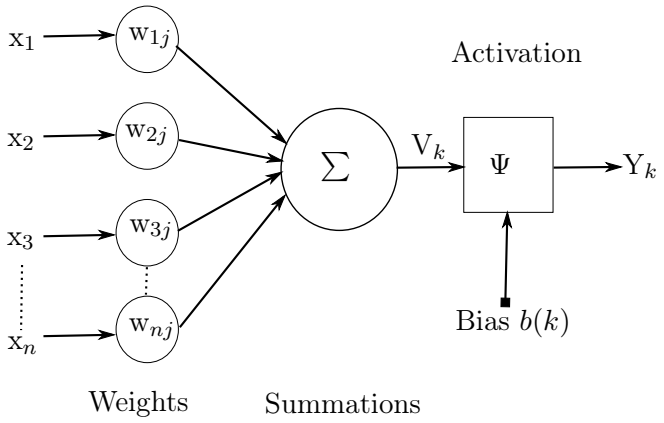

Figure 4.2: Information processing in a neural unit

Considering the information processing between the j^{th} and the k^{th} neuron, if x_j denotes the k^{th} element of the input vector x and is the input signal to the synapse j. The output Y_k transferred into the k^{th} neuron is obtained by multiplying the weight and adding the threshold coefficient. The mathematical representation of the estimated output Y_k in the k^{th} neuron is given by Equation 4.1

$$\begin{aligned} V(k) &= \sum_{j=1}^{m} w_{kj} x_j \\ Y(k) &= \Psi(V(k) + b(k)) \end{aligned} \tag{4.1}$$

where:

$V(k)$	= output of the linear combiner.
$\Psi(.)$	= Transfer function.
$Y(k)$	= Output of k^{th} neuron.
$w_{k1}, w_{k2}, ...w_{kj}$	= m weight coefficients
$b(k)$	= bias
$x_1, x_2, ...x_m$	= m inputs to k.

The weight coefficient serves as an indicator of the degree of importance of each individual connection. The summing junction receives the sum of the weighted inputs and transfers them to the activation function. The transfer functions ($\Psi = f(\xi)$, and $\xi = Y(k)$) are taken as non- linear function, usually sigmoid function which includes curves such as logistic and hyperbolic tangent curves and takes the form of Equations

4.2. The threshold is a minimum value that is provided to shift the transfer function to the left or right (Perez and Reyes, 2006) and avoid a null value in the network.

$$\begin{aligned} f(\xi) &= \left[\frac{1}{1+e^{-\xi}}\right] \quad \text{Logistic function} \\ f(\xi) &= \frac{e^{-\xi}+e^{\xi}}{e^{\xi}-e^{-\xi}} \quad \text{Hyperbolic tangent} \end{aligned} \tag{4.2}$$

MLFFs operates in two modes, namely, training and prediction modes.The training mode involves the process of modifying the connection weights in some orderly manner using a suitable learning method to achieve an output that is as close as possible to a targeted output (Svozil *et al.*, 1997). The input of a MLFF neural network can be regarded as a set of vectors, X consisting of a number of input signals $x_1, x_2, ...x_n$ as shown in Figure 4.1. During the training process, there are some available K known training pairs $f_x(k)$, $d(k)g$, $k = 1, 2, ...K$, which represent the input and desired response respectively. The output vector $Y(k)$ produced by the MLFF network for the input vector $X(k)$ is compared to the desired response $D(k)$. Initial weights are usually set at random and therefore, the initial error would be high. The most commonly used error indicator is the mean square error which is evaluated from Equation 4.3.

$$E_i = \frac{1}{2}\sum_n (d(k) - y_{kn}(\omega))^2 \tag{4.3}$$

where: E_i = Root mean square error.
$d(k)$ = Target output.
$O_{kn}(\omega)$ = Predicted output.

The error signals are then propagated backwards through the MLFF network layer by layer from the output to the first hidden layer, through a set of algorithms, until the error converges (Svozil *et al.*, 1997). This process of error propagation is referred to as back propagation because the output error is propagated from the output layer through the hidden layers to the input layer. Back propagation training algorithm uses the steepest descent minimization method for adjustment of weight and threshold coefficient holding into Equation 4.4 where n represents the n^{th} iteration and η represents the learning rate.

$$\begin{aligned} w_{kj}^{n+1} &= w_{kj}^{n} - \eta\left(\frac{\partial E}{\partial w_{kj}}\right)^n \\ b_{k}^{n+1} &= b_{k}^{n} - \eta\left(\frac{\partial E}{\partial b_{k}}\right)^n \end{aligned} \tag{4.4}$$

The second step is to evaluate the error derivatives in Equations 4.4. Equation 4.5 shows the procedure followed in calculation of error derivative with respect to weight coefficient.

$$\begin{aligned}\frac{\partial E}{\partial w_{kj}} &= \frac{\partial E}{\partial x_i}\frac{\partial x_i}{\partial w_{kj}} = \frac{\partial E}{\partial x_i}\frac{\partial f(\zeta_i)}{\partial w_{kj}} \\ &= \frac{\partial E}{\partial x_i}\frac{\partial f(\zeta_i)}{\partial \zeta_i}\frac{\partial \zeta_i}{\partial \omega_{ij}} \\ &= \frac{\partial E}{\partial x_i}f'(\xi_i)\frac{\partial(\kappa + \sum \omega_{ij}x_j)}{\partial \omega_{ij}} \\ &= \frac{\partial E}{\partial x_i}f'(\xi_i)x_j\end{aligned} \tag{4.5}$$

Following a similar procedure the error derivative with respect to the threshold is given from Equation 4.6.

$$\begin{aligned}\frac{\partial E}{\partial b_k} &= \frac{\partial E}{\partial x_i}\frac{\partial x_i}{\partial b_k} \\ &= \frac{\partial E}{\partial x_i}f'(\xi_i)l\end{aligned} \tag{4.6}$$

From Equations 4.5 and 4.6, then the relationship shown in Equation4.7 holds.

$$\frac{\partial E}{\partial w_{jk}} = \frac{\partial E}{\partial b_k}f'(\xi_i).x_j \tag{4.7}$$

Based on the approach in Equations 4.4 - 4.7, the derivatives of the objective function for the output layer and the hidden layers can be recurrently calculated and updated until the MSE between the output and the target is as minimum as possible. A complete pass through the whole training dataset is called an epoch, and training can take many epochs to complete learning. When the training is complete, the weight vector contains meaningful information and the network can then be implemented in the prediction. In the prediction mode, the information flows forward through the network from inputs to outputs producing an estimate of output values. The resulting error is used to estimate the quality of prediction of the trained network.

4.3 Model development

As outlined in section 4.2.1 there are different ways to construct an artificial neural network as described in Svozil *et al.* (1997). Understanding the problem at hand is important for selection of appropriate properties that define a neural network model. This section defines the procedure followed in development of a MLFF neural network model that was used to estimate CSP reflector optical losses using weather variation as input factors and reflector cleanliness as the output.

4.3.1 Model data

Neural networks make use of pre-acquired data to develop a meaningful input to output relationship from complex systems. Therefore, the model data forms the basis of neural network models. In this study the experimental procedures described in Chapter 3 formed the basis of the model databases. The measurements of weather

factors outlined in Subsection 3.3.3 formed the neural network input while the cleanliness obtained using the measurement device described in Subsection 3.3.1 forms the model output. Five months of data collected between February and June 2015 from the installed devices in Sonbesie Meteorological Station was used in the development of the neural network model.

4.3.2 Modelling tools

Two software programs running on Windows™ 7- professional were used in development of the model. Excel® 2013 from the Microsoft Corporation was used to manage all databases including importing files previously created using Notepad and reorganising and editing the data, preprocessing the data using statistical functions and exporting the data in a format compatible with the neural network software. The ANN was developed using the MATLAB® 2013a nntool.

4.3.3 Data pre-processing

The prediction power of the developed model depends on the reliability of the input and outputs provided during the learning process. Data pre-processing is necessary to analyse the quality and relevance of the input and output data, minimise noise from the measured data and highlight important relationship in the measured data. Generally, in rare cases, measured data is fed into the neural network in raw form.

Due to the unavailability of cleanliness data obtained from the RCMS in particular instances, as discussed in the experimental procedure in Section 3.4.2, a daily average time step was selected for development of the model relating optical losses caused by soiling on CSP reflectors due to weather factors. This ensured that the number of cleanliness measurements corresponds to the available meteorological data. In addition, cleanliness obtained during a short period was small and insignificant. Entries with missing values of cleanliness were removed from the databases since they do not offer a relation between weather factors and cleanliness.

Since the measurements of the input and output are of different magnitude, the complete data required to develop the neural network was normalised into two data sets with values lying within 0 to 1 and -1 to 1 to test sigmoid and hyperbolic tangent transfer functions respectively (Haykin and Network, 2004). Equations 4.8 and Equations 4.9 shows the procedure of normalization and de-normalisation of the data for sigmoid and hyperbolic transfer function respectively. This normalization process adjusts the measured values that have different scales, and converts them to a common size.

$$\begin{aligned} a &= \frac{b - b_{min}}{b_{max} - b_{min}} \\ b &= \frac{a - a_{min}}{a_{max} - a_{min}} \end{aligned} \tag{4.8}$$

$$\begin{aligned} a &= (b - b_{min}) \left[\frac{a_{max} - a_{min}}{b_{max} - b_{min}} \right] + a_{min} \\ b &= (a - a_{min}) \left[\frac{b_{max} - b_{min}}{a_{max} - a_{min}} \right] + b_{min} \end{aligned} \tag{4.9}$$

4.3.4 Training, testing and validation sets

Before the network is run the normalised time series input and output data was divided into three groups; training, testing and validation sets. Training data sets are usually larger because the model pattern in the learning process is developed from the training sets. The testing sets is used to evaluate the generalisation ability of the trained network and usually ranges from 10% to 30% of the training set. The validation set is used for the final evaluation of the performance of the network and usually consist of most recent observations for both training and testing. From the entire pre-processed time series data of input and output, the range selected for training, testing and validation was 70%, 15% and 15% respectively.

4.3.5 Model design

Designing a neural network model requires a number of distinct steps because it involves the selection of many variables and parameters. The design of the neural network is defined by the properties of individual neuron such as transfer function and the manner in which the inputs are combined and associated with the number of neurons in each layer as well as the type of interconnections. In addition, the selection of neural network model parameters critically depends critically on the number of training cases, the amount of noise and the complexity of the function or classification you are trying to learn (Geográfica *et al.*, 2014). A successful design can only be achieved if the problem is clearly specified and understood.

The selected neural network type was a MLFF, which was described in Section 4.2.1. The selection model input factors fall into those meteorological factors that are believed to directly or indirectly influence the rate at which soiling leads to optical degradation of CSP reflector surface. The input weather factors selected were temperature, wind speed , humidity, DNI and rainfall. The generalization ability of neural network is provided by the hidden layer(s), although increasing the number of hidden layers can lead to over fitting and longer computation time (Geográfica *et al.*, 2014). In addition, increasing the number of hidden layers also increases the number of weights relative to the size of the training set and the ability to memorise instead of learning (Geográfica *et al.*, 2014). Selection of different learning rates, weights and biases were initially generated by random numbers from MATLAB® 2013a. The two transfer functions investigated were tested under different scenarios of hidden layers and neurons. Three ranges of hidden layers (1, 2) were tested and compared in terms of computation time and model performance. The selection number of neurons in each of the hidden layers involved a heuristic approach. Four different number of neurons in the hidden layer were tested (5,10, 15,and 20). The best performing MLFF was selected.

4.3.6 Training, testing and prediction

Figure 4.3 shows the standard architecture of flow of information in a typical MLFF during the training process. This architecture outlines the procedure described in Section 4.2.1 on how MLFF was implemented in estimation of time variation of the dynamic optical losses caused by soiling on CSP reflector. The cleanliness data

$(C(t))$ is used as the target series $(y(t))$, while meteorological factors are used as the input factors $(x_i(t))$.

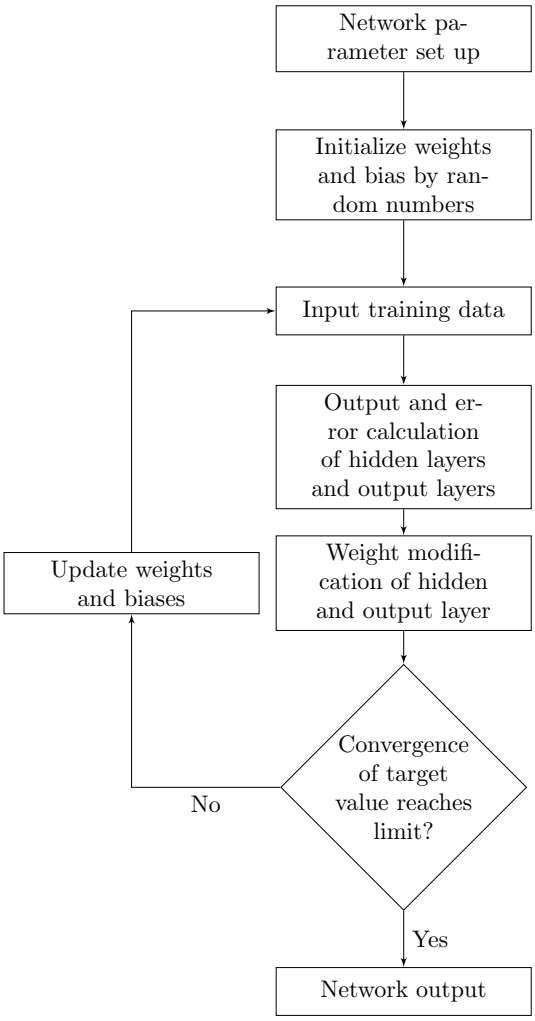

Figure 4.3: Neural network code flow chart.

From Figure 4.3, every time the network was trained different values of $(C(t))$ were achieved. The error between the estimated value and the targeted values were evaluated using MSE given by Equation 4.3. Different weights and biases were provided iteratively following the steepest descent iteration algorithm as applied in Equations 4.5 to Equations 4.7. This process updated the weights and biases provided in Equation 4.4, until the estimated values of cleanliness converged to the actual measured values of cleanliness. The model was then tested using a different set of data to validate the generalization capability of the obtained model. Different scenarios for evaluation of the different ways of developing model outlined in Subsection 4.3.5 were used in testing and optimisation of the neural network model. Once the tested and validated model was constructed, a new data set was fed in the model to provide further estimation of cleanliness values.

4.4 Summary

This chapter discussed the neural network modelling approach utilised in this study. The multi layer feed forward was selected and applied to estimate the optical losses caused by soiling on CSP reflector.

Chapter 5 presents the results of the experimental analysis and neural network modelling.

Chapter 5

Results and Discussions

5.1 Introduction

This chapter discusses the results of the experiment relating the significance of weather factors to optical losses caused by soiling on CSP reflector, as well as results obtained from time series model used for estimation of reflector optical losses. In Section 5.2, the measurement uncertainties from the device developed in the assessment of optical losses caused by soiling of CSP reflectors are outlined. The results of the impact of factors directly affecting optical losses are discussed in Section 5.3. Multi-parametric analysis of correlation of weather factors that directly or indirectly influence the optical losses are presented in section 5.4. Finally, model results based on meteorological factors for estimating soiling losses is presented in Section 5.5.

5.2 Cleanliness measurement uncertainties

The potential causes of error in the measurement of optical losses caused by soiling on a CSP reflector as measured using the RCMS device and the procedures followed to test the devices outlined in Subsection 3.3.1. This section presents the device testing results from the four measurement error elimination procedures, namely, calibration of the incident pyrheliometer, DNI measurement limits, mirror mounting position and soiling losses caused by a soiled pyrheliometer. These measurements ensured that valid and consistent cleanliness measurements were obtained in developing the relationship between optical losses caused by soiling and weather factors.

(a) Calibration of incident pyrheliometer

The first test to evaluate the uncertainty in cleanliness measurement was undertaken to calibrate the two pyrheliometers used in RCMS. Figure 5.1 shows the comparison between the two measurement observed from the measuring and incident pyrheliometer. Since the measuring pyrheliometer had recently been calibrated, it was used as the calibration reference. From Figure 5.1, it is observed that the incident pyrheliometer has a zero error of about 5 W/m^2. The correlation equation used to evaluate the values of incident DNI in calculation of cleanliness was given by y=1.006x-4.9324.

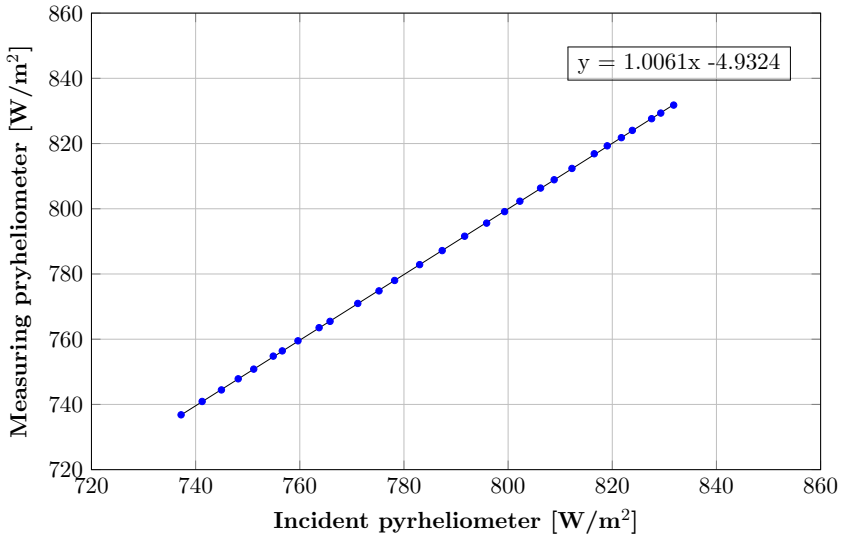

Figure 5.1: Measurement comparison between the measuring and incident pyrheliometer

(b) DNI measurement limits

The second test was conducted to establish the variation of cleanliness with measuring DNI value in order to determine the lower boundary of for reasonable measurement. Cleanliness factor measured during a partially cloudy day was plotted against the measuring DNI values. As observed in Figure 5.2, cleanliness factor obtained from measuring DNI values above 300 w/m^2 lies within a narrow range of 82-83%, while below this range, the values tend to become more noisy. Possible cause of this would be effect of circumsolar radiation received which tends to escalate in the morning and evening. Another possible cause would be sky clearance difference between the light received from the measuring and the incident pyrheliometer.

(c) Mirror position

The third preliminary test to eliminate possible causes of errors in cleanliness measurement aimed at establishing appropriate mirror mounting position in the mounting plate. The different mounting positions used were shown in Figure 3.8. Figure 5.3 shows the cleanliness values obtained from the four different positions, Pos 1, Pos 2, Pos 3 and Pos 4. As the spot (refer Figure 3.8) at the bottom pinhole falls more than 2 mm off the perfect position, the measurement value decreases less than 1% from the expected value (pos3). For Pos 4, the cleanliness factor falls to 98.5%. This obviously incorrect mounting can be avoided easily even by an inexperienced operator.

(d) Cleanliness loss caused by soiled pyrheliometer

The final preliminary test aimed at investigating the potential of errors incurred due to dust accumulation in the measurement devices. Figure 5.4 shows the variation of

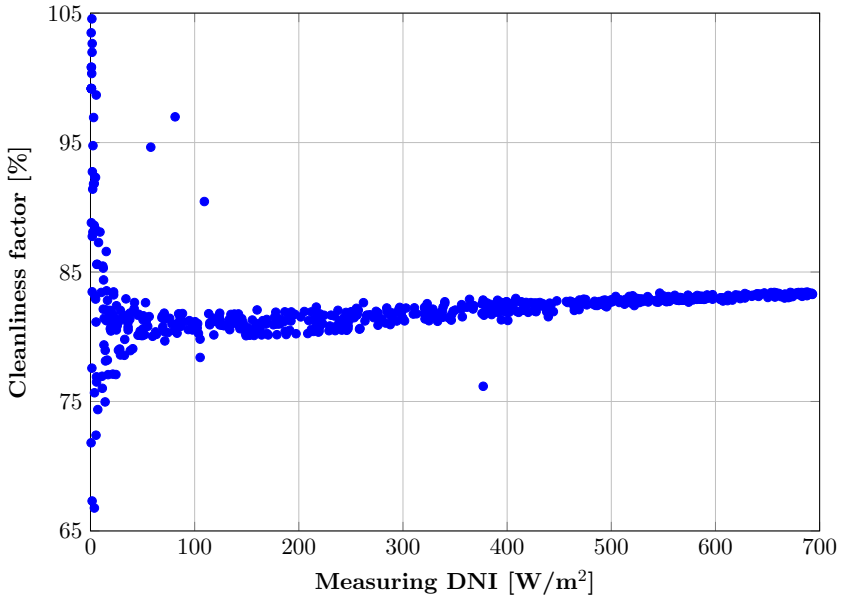

Figure 5.2: Meteorological limits of cleanliness measurement.

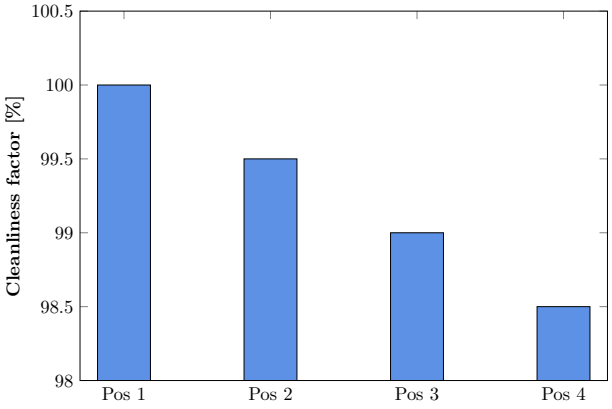

Figure 5.3: Cleanliness obtained from corresponding positions.

cleanliness with time before and after the cleaning as well as variation of the measured DNI from the measuring pyrheliometer after cleaning. An improvement in the measuring DNI values of about 2.7% was observed after cleaning, while the measured cleanliness values improved by about 1%. Daily cleaning routine as designated by the manufacturer for the two pyrheliometer was followed during experimental period.

5.3 Investigating the influence of weather factors on reflector optical losses

From the experimental design discussed in Subsection 3.4.1, the first strategy was to investigate the influence of weather factors that are believed to directly influence on

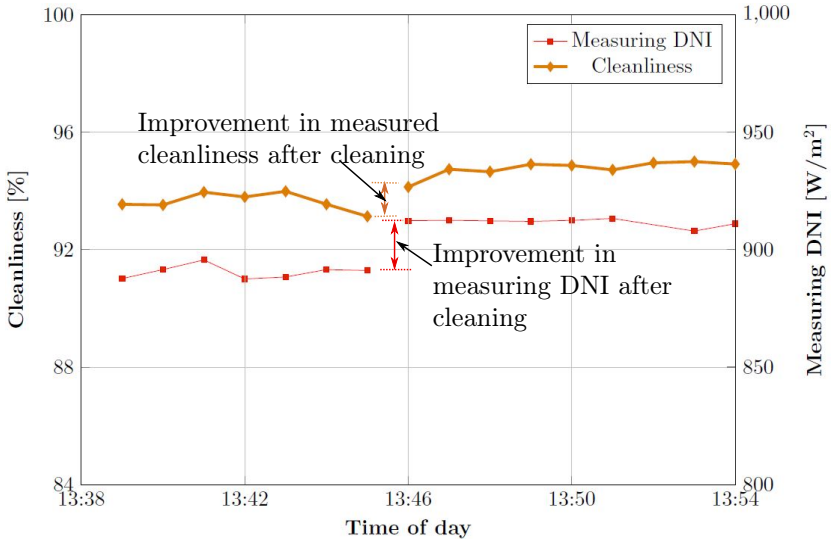

Figure 5.4: Improvement of DNI and measured cleanliness after cleaning.

reflector optical degradation with time. These factors include: rainfall, wind speed and humidity. The relationship between these weather factors and cleanliness was used to establish the variation of key weather factors influencing the time variation of optical loss caused by soiling on CSP reflector.

Figure 5.5 shows the variation of cleanliness over a period of 50 days alongside with wind speeds experienced over the same period. Wind is regarded as the greatest factor leading to soiling, and in return the optical losses caused by soiling. As observed in Figure 5.5, increased wind speed is followed by a corresponding decrease in cleanliness value. The effect of wind is to increase the density of airborne particulates matter and consequently the soiling rate. It was also noted that the effect of wind on soiling is negligible in the event of rain.

Figure 5.6 shows the variation of mirror cleanliness over a period of 50 days and the corresponding rainfall received in the test location over the same period. It was observed that after the event of light rain, cleanliness was improved. Rain washes away accumulated dust, and thus restores reflector cleanliness. It was also observed that the effectiveness of cleaning depends on the intensity and frequency of rain. Maximum cleaning effects of about 12% was achieved after a maximum rainfall of 27 mm. Similar maximum cleaning effects were observed when an average rainfall of 10 mm distributed for three days was received. Evidently, soiling may not be a challenging issue on areas receiving high and frequent rainfall. Rain does not necessarily have a cleaning effect. During the event of light rain, the cleanliness was observed to degrade rather than improve. For instance, after the light showers of about 0.2 mm received on 8th of June, the corresponding cleanliness was observed to drop from 91% to 85%. This can be explained by the fact that cementation is accelerated by light rain. In addition, light rain leaves a spotty appearance on the mirror surface hence decreasing the level of cleanliness.

Investigating the influence of humidity to cleanliness, effects similar to those those of light showers were observed. Figure 5.7 shows the variation of cleanliness

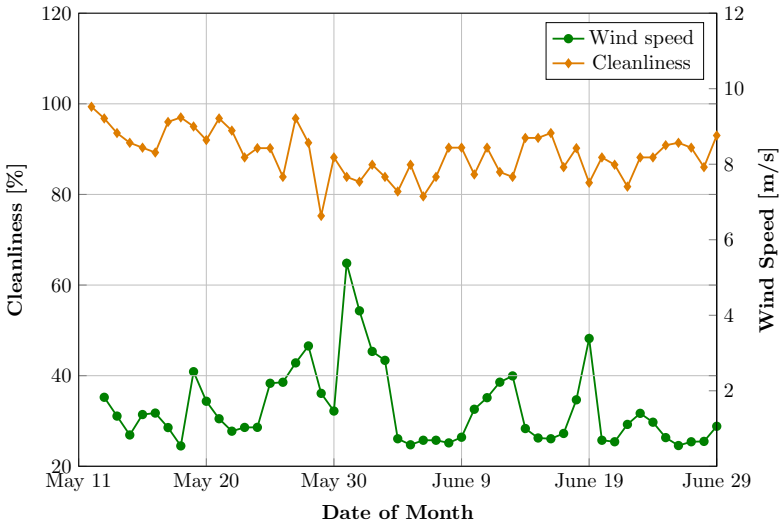

Figure 5.5: Variation of cleanliness with wind speed and humidity.

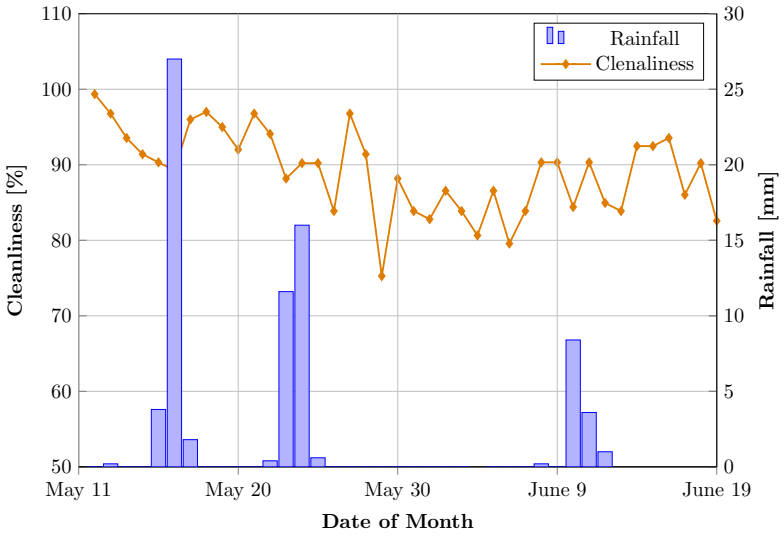

Figure 5.6: Variation of mirror cleanliness with time alongside precipitation.

with relative humidity over the 30 days experimental period. It was observed that an increase in relative humidity leads to decrease in cleanliness. Maximum level of relative humidity of 80% recorded, was followed by a drop in cleanliness from 98% to 78%. Humidity leads to the formation of dew when the temperatures fall below dew point temperature. Consequently, the dew formed leads to cementation of dirt particles and coagulation of dust deposited on the mirror surface, eventually resulting in severe reflector optical losses.

In summary, time variation of reflector optical losses caused by soiling are closely related to the time variation of weather factors that directly influence the rate of soiling. Evidently, the influence of wind speed and humidity on degradation of reflector optical state ceases during the event of rain due to cleaning effect provided

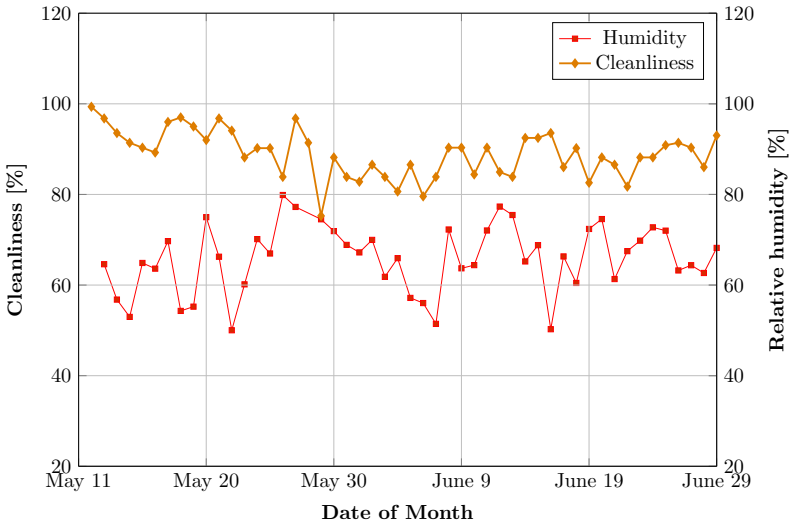

Figure 5.7: Variation of cleanliness with wind speed and humidity.

naturally by rain. Light rain have similar effects of degrading reflector surface as humidity.

5.4 Correlation of optical losses to weather factors

The second strategy in experimental design in Subsection 3.4.1 was to correlate weather factors to optical losses caused by soiling. This was achieved by observing clustering patterns between factors that directly and indirectly influence the rate of soiling. The purpose was to identify the weather factors that influence the optical loss caused by soiling on CSP reflector.

Investigating the relationship between relative humidity and cleanliness, inverse and weak correlation was observed as shown in Figure 5.8a. The low coefficient of determination, $R^2 = 0.0447$ indicates that humidity is not a good indicator of potential optical losses caused by soiling on CSP reflectors. Figure 5.8b shows results from a similar analysis where the data obtained during the event of rain was excluded since they were outliers. A relatively high coefficient of determination, $R^2 = 0.105$ was observed as compared to regression with data obtained in the event of rain included. These observations confirm that the general effect of increasing humidity levels is to increase coagulation of dirt and accelerate the rate of cemetation process. The cleaning effect of dew formed due to increasing levels of humidity requires further investigation.

Wind speed shows similar a correlation, as observed with humidity. A weak inverse relationship as shown in Figure 5.9a is observed when wind cleanliness is plotted against wind speed. A low coefficient of determination, $R^2 = 0.035$ indicates that wind speed cannot be linearly correlated to the optical loss caused by soiling. Similarly, excluding the data obtained in the event of rain and re-plotting cleanliness against wind speed, resulted in an improved coefficient of determination, $R^2 = 0.1264$, as seen in Figure 5.9b. The inverse relationship indicated that increasing wind speed results in an increase in the rate of soiling. Consequently, this

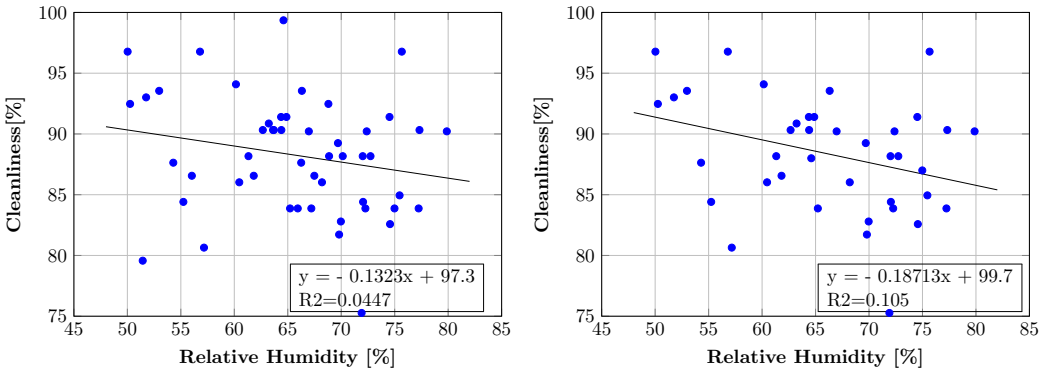

(a) Cleanliness vs. humidity. **(b)** Cleanliness vs. humidity no rain data.

Figure 5.8: Regression relationship between cleanliness and humidity (a) with rain data, (b) without rain data.

increases the optical losses caused by soiling on the CSP reflector. The improved coefficient of determination after excluding cleanliness observations in the event of rain indicate that the effect of wind speed on soiling is insignificant during the event of rain.

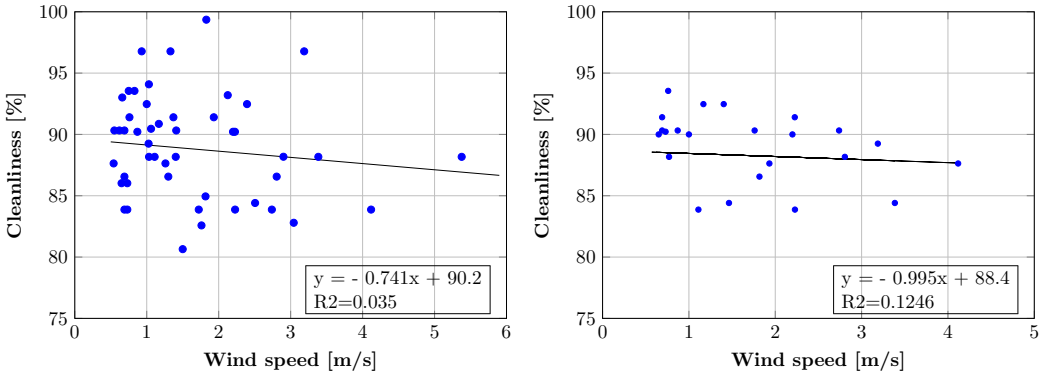

(a) Cleanliness vs. Wind speed with rain data. **(b)** Cleanliness vs. Wind speed no rain data.

Figure 5.9: Regression correlation between cleanliness and wind speed: (a) with rain data (b) without rain data.

Investigating the relationship between cleanliness and ambient temperature, a strong direct correlation and a coefficient of determination, $R^2 = 0.4682$ were observed as shown in Figure 5.10. Temperature does not have a direct effect on soiling and consequently on CSP reflector optical loss. However, it does correlate with other key weather factors that directly lead to soiling. Figure 5.11a and Figure 5.11b show the variation in temperature with relative humidity and wind speed respectively over

a 50 day experimental period. As illustrated in Figure 5.11a, temperature is inversely correlated with humidity, where, increase in temperature leads to decrease in levels of humidity. In the case of wind speed, increase in temperature leads to an increase in wind speeds as shown in Figure 5.11b. During event of rain, low temperatures are observed and natural cleaning is observed, hence, increasing cleanliness.

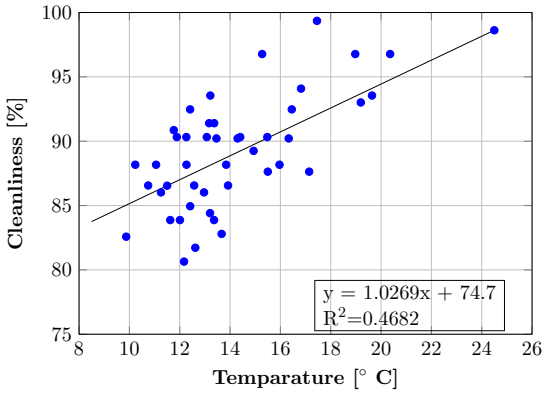

Figure 5.10: Regression correlation of temperature vs. cleanliness.

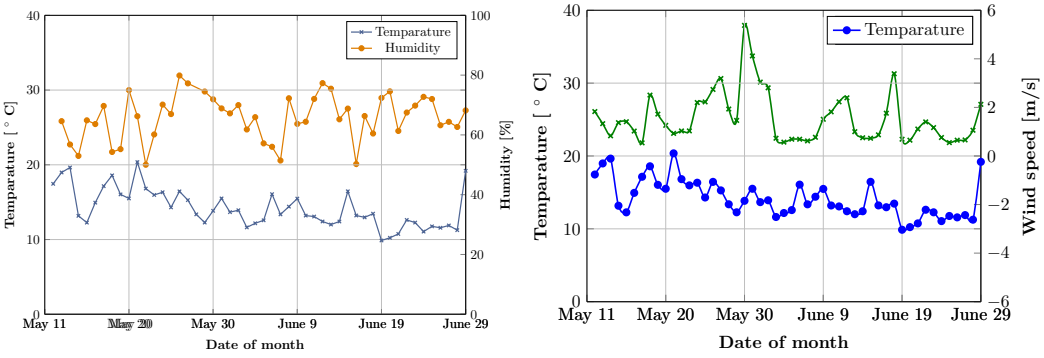

(a) Correlation between temperature and humidity

(b) Correlation between temperature and wind speed

Figure 5.11: Influence of temperature of factors affecting soiling

Investigating the correlation between cleanliness and DNI, a strong direct relationship similar to temperature correlation was observed (see Figure 5.12a) with a coefficient of determination of $R^2 = 0.2181$. This is because increase in DNI values results in an increase of temperature. This explains the reason behind high soiling rates experienced in CSP potential areas, where high DNI values and consequently high temperatures are experienced. In addition, seasonal variations of temperatures may indicate the seasonal variation of soiling.

Investigating the relationship between cleanliness and DHI, a weak inverse relation was observed between cleanliness and DHI, as shown in Figure 5.12b. A very

low coefficient of determination of $R^2 = 0.0115$ was obtained. A strong inverse correlation between DHI and cleanliness was expected since one of the factors contributing to the increase in DHI value is high content of aerosol in the atmosphere. Other factors that could influence the DHI levels such as cloud cover requires further investigation.

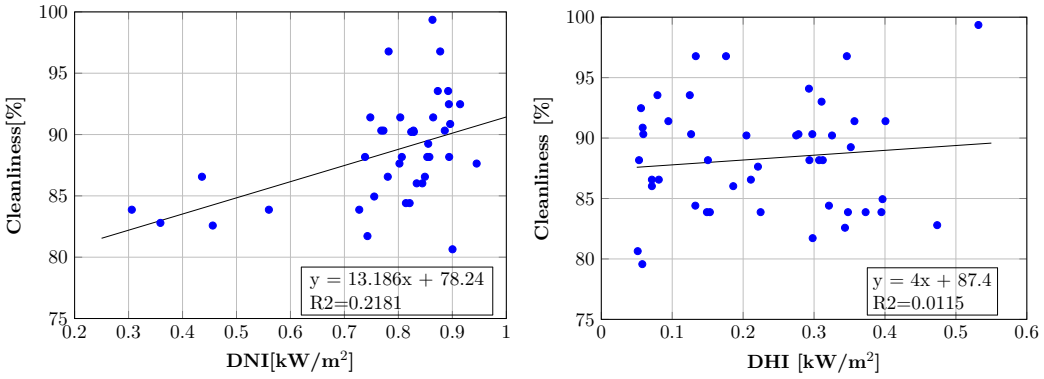

(a) Variation of cleanliness with temperature.

(b) Variation of cleanliness with direct normal irradiation (DNI).

Figure 5.12: Regression correlation between cleanliness and; (a) Direct normal irradiation (b) Diffuse horizontal irradiation.

The cluster and regression analysis that was carried out provide fundamental weather factors that influence optical loss caused by soiling on CSP reflectors. Temperature and DNI measurement were found to affect a combination of key weather factors that lead to soiling and consequently the optical loss caused by soiling on CSP reflectors. Wind speed and humidity were the weather factors that directly influence the rate of soiling, but were observed to poorly correlate with the optical loss caused by soiling on CSP reflectors. Table 5.1 summarises the regression coefficients, coefficient of determination (R^2) and constants obtained from the correlations between the degradation of cleanliness and weather factors. Variation of soiling losses on CSP reflector surface is a function of a combination of weather factors, and no single weather factor provides sufficient explanation to these losses.

5.5 Modelling weather factors to estimate soiling losses

This section presents the modelling results obtained following the neural network modelling procedures presented in Chapter 4. The aim of the neural network model was to combine weather factors and relate them to optical loss caused by soiling on a CSP reflector and provide further estimation of time variation of these soiling optical losses.

Table 5.1: Summary of correlation of weather factors with mirror cleanliness

	Coefficient		
Parameter	a	b	R^2
Temperature	1.03	74.73	0.47
Direct normal radiation (DNI)	13.17	78.24	0.22
Wind speed (No rain data)	-0.10	88.44	0.12
Relative humidity (No rain data)	-0.19	99.71	0.11
Relative humidity	-0.13	97.36	0.04
Wind speed	-0.74	90.22	0.03
Direct Horizontal radiation (DHI)	4.00	87.38	0.01

5.5.1 Preliminary model test

Several ways and designs that can be followed in developing a neural network were discussed in Subsection 4.3.5. Preliminary model tests aimed at coming up with a neural network model that is simple, yet suitable to provide analysis of weather factors influencing optical losses caused by soiling on CSP reflector. Three aspects of neural network modelling namely, model transfer function, number of hidden layers and number of neurons in hidden layers were tested. The normalisation parameters for model input data are provided in Table D.2 in Appendix D.

Figure 5.13 shows the coefficient of determination for all data obtained when sigmoid and hyperbolic transfer functions were tested with a different number of neurons from a single hidden layer. This test was performed under 100,000 training cycles to ensure that the training is complete under a single model run. From Figure 5.13 it is observed that better coefficients of determination were observed when the number of neurons were increased. Hyperbolic tangent gives better correlations than the sigmoid function due to wide data range and was adopted in the developed model. Testing the adopted model with different numbers of hidden layers, it was observed that increasing the number of neurons had a insignificant effect on the obtained residual. Table 5.2 summarises the coefficient of determination obtained when different number of hidden layers were tested. From Table 5.2, it is observed that, the training time increases from 199 seconds to 746 seconds when the number of hidden layers increases from 1 to 3. This implies that increasing the number of hidden layers increases the training time. This is always associated with over fitting in the model.

5.5.2 Cleanliness estimation from adopted model

Figure 5.14 shows the variation of the model estimated cleanliness and the measured cleanliness over a 50 day experiment period. The adopted model used hyperbolic transfer function with 10 hidden layers, trained over 100,000 training cycles. A similar cleanliness variation trend line was observed between the measured and the estimated cleanliness (see Figure 5.14). It was also observed that the model gen-

Table 5.2: Summary of model performance at different number of hidden layers

Number of hidden layers	Training time (sec)	R^2 (All)
1	199	0.968
2	526	0.986
3	746	0.989

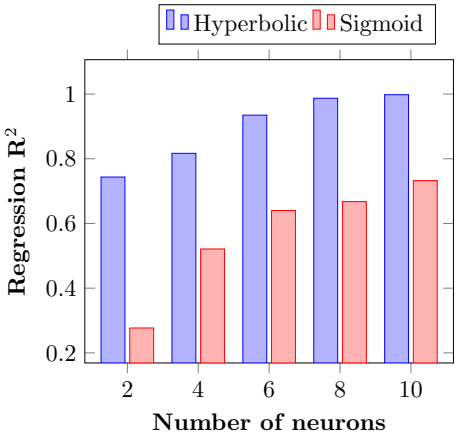

Figure 5.13: Variation of coefficients of determination at different neurons and transfer function.

erally underestimates the cleanliness values. The percentage difference between the measured and estimated cleanliness values are presented in Table D.3 in Appendix D. The maximum percentage difference between the measured and the estimated value that was observed was 5.4%.

Figure 5.15 shows the performance of the adopted model represented by the coefficient of determination. In all the data sets, the coefficient of determination (R^2) obtained were:(i) 0.961 for training data set; (ii) 0.999 for the validation data set; (iii) 0.950 for testing data set; and (iv) 0.968 for all the data sets combined. These high coefficients of determinations indicate a good predictive power of the adopted neural network in estimating optical losses caused by soiling on CSP reflector. Equation 5.1 represents the relationship between the estimated and measured values for all the data sets. From Equation 5.1, it can be observed that the model underestimates the values and the estimated values were about 93% of the measured values.

$$C_{est} = 0.93xC_{Meas} + 0.013 \tag{5.1}$$

The equation relating the input and output are long and quite complex. Referring to Equation 4.1, the values obtained in the hidden layer of the adopted model were evaluated using Equation 5.2. Table 5.3 provides the weights and biases between the input and hidden layer as obtained from the adopted model. These weights and

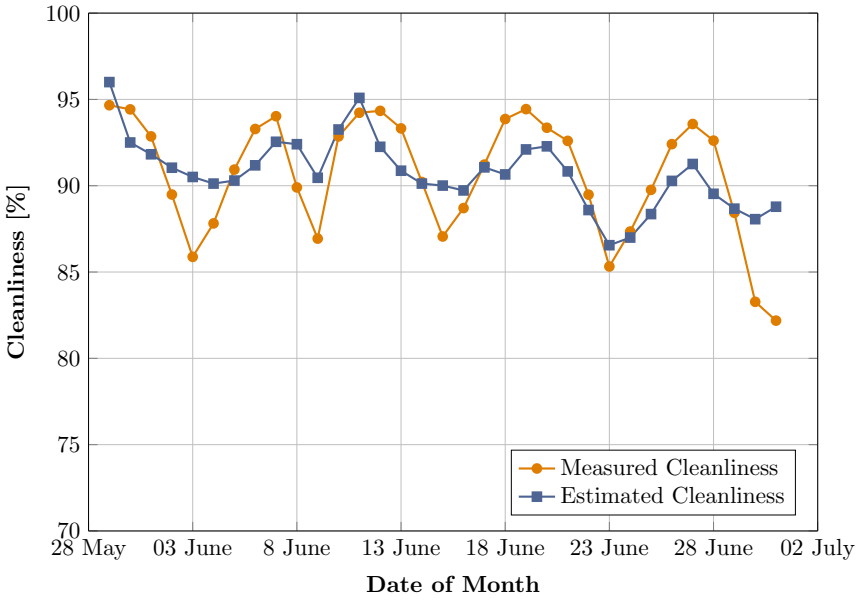

Figure 5.14: Variation of estimated and measured cleanliness with time.

biases shows the value that were used in the hidden layer of the model following Equation 5.2.

Table 5.3: Weights and biases between the input and hidden layer

		Weights (w_{jk})				
Node	**Bias**	**DNI**	**Rainfall**	**Temp**	**Wind speed**	**Humidity**
1	4.3973	-1.465	1.429	-4.548	2.553	1.694
2	-3.5115	3.474	-4.052	-1.661	0.894	1.113
3	2.6748	-1.285	3.195	4.379	-1.401	0.310
4	1.5117	-2.488	1.707	-3.596	-2.433	-0.052
5	-1.2365	2.759	-1.178	4.169	-3.170	-0.310
6	1.0596	4.090	-2.502	1.715	0.397	0.939
7	-2.7523	-1.549	-2.357	-1.102	3.754	2.114
8	-2.8582	-4.294	-1.978	0.865	-1.234	0.368
9	-4.3968	-3.231	-1.204	-3.372	-2.075	0.074
10	-5.2038	-1.259	-0.036	0.110	4.796	2.479

$$H_k = \Psi(\sum_{j=1}^{5} w_{kj}x_j + b(k)) \tag{5.2}$$

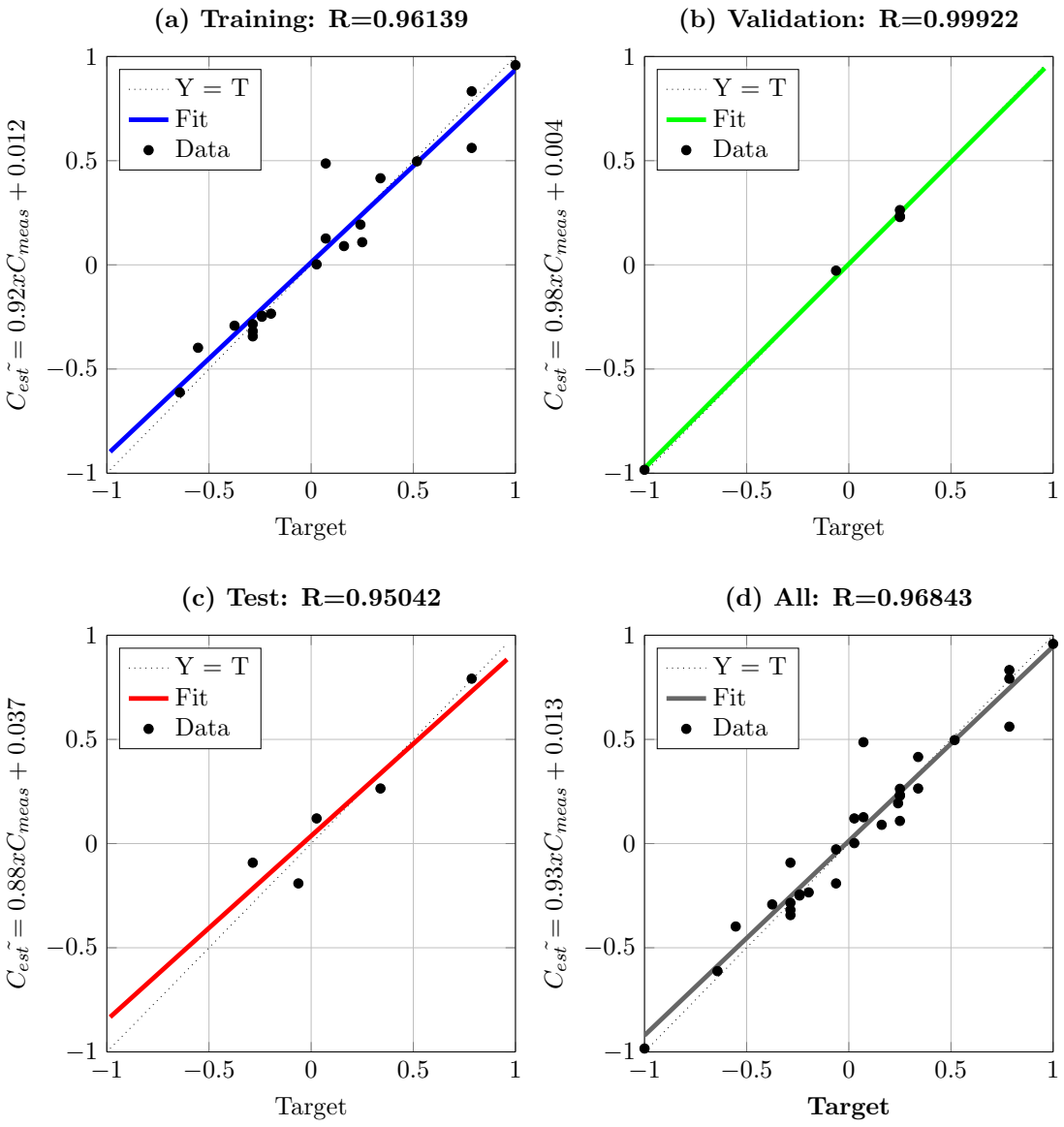

Figure 5.15: Correlation between the estimated and measured normalized cleanliness.

Considering the relation between the hidden layer and the output layer, cleanliness which defines the optical state of the reflector at any instant t from the model was then evaluated according to Equation 4.1. Table 5.4 provides the weights obtained from the hidden layer to the output layer for the adopted model with a constant bias of $b(k) = 1.476$ obtained between the hidden layer and the output. Based on the weights obtained between the hidden layer and the output (cleanliness), only nodes 4 and 8 appear not to be relevant in explaining cleanliness.

Table 5.4: Weights between the nodes at hidden layer and output

Node	Weight ($\mathbf{w}_{jk}$)
1	-1.329
2	1.4273
3	1.8228
4	0.16099
5	-1.7641
6	-0.62803
7	-1.0093
8	0.30508
9	-1.8025
10	0.88421

$$C(t) = \Psi(\sum_{j=1}^{10} w_{kj} H_k + b(k)) \tag{5.3}$$

The results obtained from the developed CSP reflector optical degradation using neural network shows that, a combination of weather factors can be used to estimate the optical degradation caused by soiling on CSP reflector. A high coefficient of determination was observed from the neural network model as compared to the correlations that considered the relationship between a single weather factor and the optical losses caused by soiling in CSP reflector.

5.6 Summary

This chapter presented the results of experimental data and a neural network model aimed at identifying key weather factors that influence the optical losses caused by soiling on CSP reflector. The key highlights are:

- In the event of no rain, the following is expected:
  - i When temperatures are high wind speed increases and consequently cleanliness reduces.
  - ii When temperatures are low humidity increases and dirt coagulation is accelerated. This results in reduction in cleanliness.
- During the event of rain, low temperatures are experienced and cleanliness is increased.
- The neural network model which accounts for a number of weather factors simultaneously shows a high coefficient of determination as compared to the correlations that consider only a single weather factor and the optical losses caused by soiling in CSP reflector.

Chapter 6

Conclusions and recommendations

This chapter presents a summary of key findings of this study. The aim of the study was to relate the time variations of optical losses caused by soiling on CSP reflector surfaces to the local weather factors. Correlations between selected key weather factors and observed CSP reflector cleanliness were established. A neural network model that simultaneously analysed correlation of multiple weather factors was developed. This was implemented in estimation of optical losses caused by soiling on CSP reflectors.

6.1 Key contributions and findings

6.1.1 Cleanliness measurement device, RCMS

The study utilised cleanliness monitoring as the method to assess reflector optical losses caused by soiling. The study designed and developed a device termed as real-time cleanliness monitoring sensor (RCMS), which was used to collect DNI measurements in order to infer reflector optical state.

Among the sources of error in the measurement was the calibration of pyrheliometer used in the RCMS, variation of intensity of measuring DNI values, mirror positioning and soiling of pryheliometer. Error analysis and calibration was undertaken to reduce potential sources of errors for the observed values since RCMS was a new device. In doing so, this increased the confidence in using such observed values to assess optical losses caused by soiling on CSP reflector.

6.1.2 Experimental analysis

The experimental analysis was aimed at estimating the correlations between the weather factors and cleanliness. Two relations between cleanliness and weather factors were studied. In the first case, the variation of cleanliness with weather factors that directly influence the rate of soiling were investigated over time. It was observed that wind speed and humidity lead to degradation in the reflector optical state. On the other hand, rain offers natural cleaning leading to improved cleanliness of the reflector. The challenge of the results from this analysis is that it did not account

for the interaction of the weather factors when relating them to cleanliness. This was achieved using the neural network model discussed in Subsection 6.1.3.

In the second case, all the weather factors that either directly or indirectly influence reflector optical losses were statistically analysed using clustering method to investigate appropriate weather indicators that can be related to reflector optical losses caused by soiling. The results showed a relatively strong correlation between temperature and DNI to cleanliness, which were $R^2 = 0.468$ and $R^2 = 0.2181$ respectively. Although a relatively strong correlation was observed, temperature and DNI do not directly influence cleanliness. Weather factors that directly influence cleanliness, namely, wind speed and humidity showed weak correlation to cleanliness. Temperature and DNI directly influence wind speed, as well as humidity and consequently represents a combination of ultimate effect of these two factors. This indicates that the variation of optical losses caused by soiling is well represented by a combination of local weather factors.

6.1.3 Neural network model findings

Artificial neural networks offer a high potential in estimating CSP reflector optical losses caused by soiling. A multi layer feed forward neural network model was created by combining five input weather factors namely, wind speed, temperature, DNI, rainfall and humidity. The mirror optical state (cleanliness), was the model output.When these five input weather factors were combined with the output,a high coefficient of determination of $R = 0.964$ was observed.

The neural network underestimated soiling measurements with maximum percentage difference between the measured and estimated cleanliness of about 5.4%. This indicates that soiling variation with time and season are caused by a combination of weather factors acting together. If well trained, the neural network model can be adopted in estimating CSP reflector optical losses caused by soiling which eventually can dramatically lead to improvement of plant performance and cleaning routines.

The neural network model demonstrated that a combination of weather factors can be used to estimate the optical degradation caused by soiling on CSP reflector. A high coefficient of determination was observed from the neural network model as compared to the correlations that considered the relationship between a single weather factor which were done in the experimental analysis.

6.2 Conclusions

Real time measurement of optical losses caused by soiling on CSP reflector surfaces shows a great potential in facilitating the development of relationship between factors affecting the rate of optical loss caused by soiling on reflectors. Optical loss caused by soiling on CSP reflector is as a result of the combined effect of a number of weather factors. Key weather factors that directly affect the rate of soiling are; wind speed, relative humidity and rainfall. These factors do not correlate well with optical losses due to interaction amongst them. Weather factors such as temperature and DNI affect a number of these weather factors and hence correlate well with optical losses caused by soiling on CSP reflector. Estimation of soiling losses using neural network

shows a great potential for tackling the complex soiling phenomenon by establishing a combined effect of the factors influencing the rate of soiling.

6.3 Recommendations for future work

Possible future research opportunities were identified in this study. These include:

- **Industrial real time reflectiveness measurement**

  Reflectivity measurement is an important operational requirement for CSP plants. Developing such sensors as integrated sensors in the plant's distributed control system and in supervisory control and data acquisition (SCADA) system would be an interesting area of future research. Ideally, the reference mirror should be integrated into the plant and be cleaned with the identical cleaning processes as the rest of the plant.

- **Spatial influence on reflectivity**

  Significant differences exists between different CSP sites based on rain patterns, geotechnical characteristics, humidity, temperature, wind speed, mirror inclination and height of the mirror. It will be essential for future research to examine the influence of these spatial variations on optical losses caused by soiling on CSP reflector from different CSP potential geographical regions. This would enable the development of CSP specific soiling maps.

- **Optimisation of cleaning operations**

  It will be essential and interesting for future research to combine the weather predictions in order to optimise the timing of reflector washing for specific CSP plant configurations. This would provide critical empirical information to CSP investors on the potential of operational expenses associated with cleaning routine expected at different CSP regions.

- **Neural networks applied to other aspects of technology**

  There are future improvements on the neural network model that may be required. This would involve including other possible parameters such as site characteristics, dust properties and collector properties that affect optical losses caused by soiling on CSP reflectors.Developing a model capable of estimating soiling losses across the entire solar field is also a possible future research direction.

  Further, while linear regression is shown to be powerful, one of the biggest needs in the industry is to have an intelligent power production forecast for individual plants and for the overall generation network. This could be an interesting future research on how to develop these intelligent forecasts.

List of References

Alkasassbeh, M., Sheta, A.F., Faris, H. and Turabieh, H. (2013). Prediction of PM10 and TSP Air Pollution Parameters Using Artificial Neural Network Autoregressive , External Input Models : A Case Study in Salt , Jordan. *Middle-East Journal of Scientific Research*, vol. 14, no. 7, pp. 999–1009. ISSN 19909233.

Barrierger, M.T. (1978). *Engineering Analysis of Site Depended Factors Affecting the Crosbyton Solar Power Project*. Ph.D. thesis.

Beckwith, T.G., Marangoni, R.D. and Lienhard, J.H. (2007). *Mechanical measurements*. Pearson Prentice Hall Upper Saddle River, NJ. ISBN 0201847655.

Berg, R.S. (1978). Heliostat dust buildup and cleaning studies. Tech. Rep..

Bevington, P.R. and Robinson, D.K. (2003). Data reduction and error analysis. *Mc Graw Hill- New York*.

Biryukov, S. (2000 sep). Degradation of reflectivity of parabolic mirror caused by dust on its surface. *Journal of Aerosol Science*, vol. 31, pp. 985–986. ISSN 00218502.

Blackmon, J.B. (1978). Dust buildup tests of heliostats and mirror specimens. Tech. Rep..

Bonnardot, V., Planchon, O., Carey, V. and Cautenet, S. (2002). Diurnal wind, relative humidity and temperature variation in the Stellenbosch-Groot Drakenstein wine-growing area. *South African Journal for Enology and Viticulture*, vol. 23, no. 2, pp. 62–71. ISSN 0253-939X.

Bowman, J., Jensen, S. and McDonald, M. (2011). Analysis Of Soiling Rates At The Victor Valley Community College CPV Site. In: *7TH INTERNATIONAL CONFERENCE ON CONCENTRATING PHOTOVOLTAIC SYSTEMS: CPV-7*, vol. 1407, pp. 312–316. AIP Publishing. ISBN 0094-243X.

Brogren, M., Karlsson, B., Roos, A. and Werner, A. (2004). Analysis of the effects of outdoor and accelerated ageing on the optical properties of reflector materials for solar energy applications. *Solar energy materials and solar cells*, vol. 82, no. 4, pp. 491–515.

Call, P.J. (1980). Summary of Solar Experience with the soiling of optical surfaces. In: *Workshop held in Denver, 16-17 Jul. 1979*, vol. 1, pp. 16–17.

Campell Scientific. Inc (1996). 03001 R.M. Young Wind Sentry Set - Instruction manual.

Campell Scientific. Inc (2015). CS215 Temperature and Relative Humidity Probe. pp. 5–6. Available at: `http://s.campbellsci.com/documents/us/manuals/cs215.pdf`

Caron, S. (2011). Accelerated aging of thick glass second surface silvered reflectors under sandstorm conditions.

Crawford, J.S., Stewart, J. and Pérez-ullivarri, J.A. (2012). A Comparison of Three Portable Reflectometers for Use in Operations and Maintenance of CSP Plants. In: *SolarPACES 2012*.

Cuddihy, E.F. (1980 sep). Theoretical considerations of soil retention. *Solar Energy Materials*, vol. 3, no. 1-2, pp. 21–33. ISSN 01651633.
Available at: `http://www.sciencedirect.com/science/article/pii/0165163380900477`

Czanderna, a., Masterson, K. and Thomas, T.M. (1985). Silver/Glass Mirrors for Solar Thermal Systems.

Deffenbaugh, D.M., Green, S.T. and Svedeman, S.J. (1986). The effect of dust accumulation on line-focus parabolic trough solar collector performance. *Solar Energy*, vol. 36, no. 2, pp. 139–146.

Department of Energy (2010). Executive Summary of the Draft Integrated Electricity Resource Plan for South Africa - 2010 to 2030. Tech. Rep. October.

Department of Environmental Affairs (2011). South African Government's position on Climate Change. Tech. Rep..

Duffie, J.A. and Beckman, W.A. (1980). *Solar engineering of thermal processes*, vol. 3. Wiley New York.

El-Shobokshy, M.S. and Hussein, F.M. (1993). Effect of dust with different physical properties on the performance of photovoltaic cells. *Solar Energy*, vol. 51, no. 6, pp. 505–511.

Elminir, H.K., Ghitas, A.E., Hamid, R., El-Hussainy, F., Beheary, M. and Abdel-Moneim, K.M. (2006 nov). Effect of dust on the transparent cover of solar collectors. *Energy Conversion and Management*, vol. 47, no. 18-19, pp. 3192–3203. ISSN 01968904.

Fend, T., Hoffschmidt, B., Jorgensen, G., Küster, H., Krüger, D., Pitz-Paal, R., Rietbrock, P. and Riffelmann, K.-J. (2003). Comparative assessment of solar concentrator materials. *Solar Energy*, vol. 74, no. 2, pp. 149–155.

Fernández-Reche, J. (2006 jul). Reflectance measurement in solar tower heliostats fields. *Solar Energy*, vol. 80, no. 7, pp. 779–786. ISSN 0038092X.
Available at: `http://linkinghub.elsevier.com/retrieve/pii/S0038092X0500232X`

Freese, R. and Pettit (1980). Wavelength Dependent Scattering Caused by Dust Accumulation on Solar Mirrors. vol. 3.

Gee, R., Brost, R., Zhu, G. and Jorgensen, G. (2010). An improved method for characterizing reflector specularity for parabolic trough concentrators. In: *Proceedings of Solar PACES Conference Perpignan (France)*, p. 2124.

Geográfica, D.D.E.E., Energia, G.E., Gabriel, A. and Rocha, C.D. (2014). Photovoltaic Forecasting with Artificial Neural Networks Photovoltaic Forecasting with Artificial Neural Networks André Gabriel Casaca de Rocha Vaz.

Google Earth 6.0, G.E. (2015). Google Earth Location: 33°55'42.84" S, 18°51'55.08" E, Elevation: 119m.
Available at: `http://www.earth.google.com`

Griffith, D.J., Vhengani, L. and Maliage, M. (2014). Measurements of Mirror Soiling at a Candidate CSP Site. *Energy Procedia*, vol. 49, pp. 1371–1378.

Haykin, S. and Network, N. (2004). *A comprehensive foundation*, vol. 2.

Heerden, Van and Louis (2015). Status of CSP and its future in the South African energy mix. Tech. Rep..

Heimsath, A., Heck, M., Morin, G., Kiewitt, W. and Platzer, W. (2014). SOILING OF ALUMINUM AND GLASS MIRRORS UNDER DIFFERENT CLIMATIC CONDITIONS AND TECHNO-ECONOMIC OPTIMIZATION OF CLEANING INTERVALS.

Heinold, B., Tegen, I., Esselborn, M., Kandler, K., Knippertz, P., Müller, D., Schladitz, A., Tesche, M., Weinzierl, B., Ansmann, A., Althausen, D., Laurent, B., Massling, A., Müller, T., Petzold, A., Schepanski, K. and Wiedensohler, A. (2009). Regional Saharan dust modelling during the SAMUM 2006 campaign. *Tellus, Series B: Chemical and Physical Meteorology*, vol. 61, no. 1, pp. 307–324. ISSN 02806509.

Herrmann, J., Slamova, K., Glaser, R. and Köhl, M. (2014). Modeling the Soiling of Glazing Materials in Arid Regions with Geographic Information Systems (GIS). *Energy Procedia*, vol. 48, pp. 715–720. ISSN 18766102.
Available at: `http://linkinghub.elsevier.com/retrieve/pii/S1876610214003452` `http://www.sciencedirect.com/science/article/pii/S1876610214003452`

Ho, C.K., Ghanbari, C.M., Neill, M.B.O. and Yuan, J.K. (1995). On-Sun Testing of a Heliostat Using Facets with Metallized Polymer Films. *Renewable Energy*, vol. 1100, pp. 1–8.

Hugo, N. (2015). PFG specteral testing.

(IEA), I.E.A. (2010). Technology Roadmap: Concentrating Solar Power. pp. 1–50.

Igel, E.A. and Hughes, R.L. (1979). Optical analysis of solar facility heliostats. *Solar Energy*, vol. 22, no. 3, pp. 283–295.

Karim, M., Naamane, S., El Amrani EL Hassani, I., Delord, C., Belcadi, S., Tochon, P., Bennouna, A., Amrani, I.E., Hassani, E.L., Delord, C., Belcadi, S., Tochon, P. and Bennouna, A. (2014). Towards the prediction of CSP mirrors wear: Methodology of analysis of influencing parameters on the mirrors surface degradation: Application in two different sites in Morocco. *Solar Energy*, vol. 108, pp. 41–50. ISSN 0038092X.
Available at: `http://dx.doi.org/10.1016/j.solener.2014.06.036`

Kattke, K. and Vant-Hull, L. (2012). Optimum target reflectivity for heliostat washing.

Kennedy, C., Terwilliger, K. and Milbourne, M. (2005). Development and Testing of Solar Reflectors. Tech. Rep..

Kipp & Zonen (2001). Pyrheliometer CH1 Instruction Manual. vol. 5003, pp. 1–23.

Kipp & Zonen (2011). Kipp & Zonen SOLYS 2 instruction manual. Tech. Rep..

Kukkonen, J. (2003 oct). Extensive evaluation of neural network models for the prediction of NO2 and PM10 concentrations, compared with a deterministic modelling system and measurements in central Helsinki. *Atmospheric Environment*, vol. 37, no. 32, pp. 4539–4550. ISSN 13522310.
Available at: `http://www.sciencedirect.com/science/article/pii/S1352231003005831`

Major, G. (1994). Circumsolar correction for pyrheliometers and diffusometers. *WMO/TD*, , no. 635, p. 42.

Mani, M. and Pillai, R. (2010 dec). Impact of dust on solar photovoltaic (PV) performance: Research status, challenges and recommendations. *Renewable and Sustainable Energy Reviews*, vol. 14, no. 9, pp. 3124–3131. ISSN 13640321.
Available at: `http://www.sciencedirect.com/science/article/pii/S1364032110002455`

Massi Pavan, A., Mellit, A. and De Pieri, D. (2011). The effect of soiling on energy production for large-scale photovoltaic plants. *Solar Energy*, vol. 85, no. 5, pp. 1128–1136. ISSN 0038092X.
Available at: `http://linkinghub.elsevier.com/retrieve/pii/S0038092X11000892`

Meijers, J.P. (2015). Stellenbosch weather.
Available at: `http://weather.sun.ac.za/`

Merrouni, a.A., Wolfertstetter, F., Mezrhab, a., Wilbert, S. and Pitz-Paal, R. (2015). Investigation of Soiling Effect on Different Solar Mirror Materials under Moroccan Climate. *Energy Procedia*, vol. 69, pp. 1948–1957. ISSN 18766102.
Available at: `http://linkinghub.elsevier.com/retrieve/pii/S1876610215005007`

Meyen, S., Nrel, G., Solar, J.C.A., Flabeg, S.H., Ise, W.P.F., Ise, A.H.F., Neill, M.O., Alanod, S.Z.B. and Alanod, S.Z.B. (2013). Parameters and method to evaluate the solar reflectance properties of reflector materials for concentrating solar power technology-Official SolarPACES reflectance guideline verstion 2.5.

Meyen, S., Sutter, F., Heller, P. and Oschepkov, A. (2014). A New Instrument for Measuring the Reflectance Distribution Function of Solar Reflector Materials. *Energy Procedia*, vol. 49, pp. 2145–2153. ISSN 18766102.

Nelson, A., Keene, S., Diaz, J.M., Susca, E., Nazarian, D., Gonzales, E. and Kennedy, C.E. (2011). Understanding soil adhesion in Concentrating Solar Power plants: a novel analysis of soil characteristics. *SolarPaces Conference*.

Noring, J.E., Grether, D.F. and Hunt, A.J. (1991). Circumsolar radiation data: The Lawrence Berkeley Laboratory reduced data base. Final subcontract report. Tech. Rep..

Perez, P. and Reyes, J. (2006). An integrated neural network model for PM10 forecasting. *Atmospheric Environment*, vol. 40, no. 16, pp. 2845–2851. ISSN 1352-2310.

Petavratzi, E., Kingman, S. and Lowndes, I. (2005). Particulates from mining operations: A review of sources, effects and regulations. *Minerals Engineering*, vol. 18, pp. 1183–1199. ISSN 08926875.

Pettit, R.B., Laboratories, S. and Nm, A. (1977). Characterization of the reflected beam profile of solar mirror materials. *Solar Energy*, vol. 19, no. 6, pp. 733–741.

Raccurt, O., Delord, C., Bouquet, C. and Couturier, R. (2014). Correlation between Solar Mirror Degradation and Colorimetric Measurement of Protective Back Layer. *Energy Procedia*, vol. 49, pp. 1700–1707.

Roth, E.P., Pettit, R.B. and Murr, L.E. (1980). CHAPTER 6 - The Effect of Soiling on Solar Mirrors and Techniques Used to Maintain High Reflectivity. In: *Solar Materials Science*, chap. Chapter6, pp. 199–227. Academic Press. ISBN 978-0-12-511160-7.

Saberian, A., Hizam, H., Radzi, M.A.M., Ab Kadir, M.Z.A., Mirzaei, M., Kadir, M.Z.a.A. and Mirzaei, M. (2014). Modelling and prediction of photovoltaic power output using artificial neural networks. *International Journal of Photoenergy*. ISSN 1110-662X.

Sarver, T., Al-Qaraghuli, A. and Kazmerski, L.L. (2013). A comprehensive review of the impact of dust on the use of solar energy: History, investigations, results, literature, and mitigation approaches. *Renewable and Sustainable Energy Reviews*, vol. 22, pp. 698–733.

Sayyah, A., Horenstein, M.N. and Mazumder, M.K. (2013 jun). Mitigation of soiling losses in concentrating solar collectors. *2013 IEEE 39th Photovoltaic Specialists Conference (PVSC)*, pp. 0480–0485.
Available at: `http://ieeexplore.ieee.org/lpdocs/epic03/wrapper.htm?arnumber=6744194`

Sector, V.P., Hoffschmidt, B., Alexopoulos, S., Rau, C., Sattler, J., Anthrakidis, a., Boura, C., Connor, B.O. and Hilger, P. (2012). Concentrating Solar Power. *Comprehensive Renewable Energy*, vol. 3, no. 2, pp. 595–636. ISSN 0094243X.
Available at: `http://dx.doi.org/10.1016/B978-0-08-087872-0.00319-X`

Shao, Y., Wyrwoll, K.-H., Chappell, A., Huang, J., Lin, Z., McTainsh, G.H., Mikami, M., Tanaka, T.Y., Wang, X. and Yoon, S. (2011). Dust cycle: An emerging core theme in Earth system science. *Aeolian Research*, vol. 2, no. 4, pp. 181–204.

Stine, W.B. and Geyer, M. (2001). Power from the Sun.

Sutter, F., Meyen, S., Heller, P. and Pitz-Paal, R. (2013). Development of a spatially resolved reflectometer to monitor corrosion of solar reflectors. *Optical Materials*, vol. 35, no. 8, pp. 1600–1608. ISSN 09253467.
Available at: `http://dx.doi.org/10.1016/j.optmat.2013.04.013`

Svozil, D., Kvasnicka, V.V. and Pospichal, J.J. (1997). Introduction to multi-layer feed-forward neural networks. *Chemometrics and intelligent laboratory systems*, vol. 39, no. 1, pp. 43–62. ISSN 0169-7439.
Available at: `http://linkinghub.elsevier.com/retrieve/pii/S0169743997000610`

Tahboub, Z., Oumbe, A., Hassar, Z. and Obaidli, A. (2013). Modeling of irradiance attenuation from a heliostat to the receiver of a solar central tower. *Energy Procedia*, vol. 49, pp. 2405–2413. ISSN 18766102.
Available at: `http://dx.doi.org/10.1016/j.egypro.2014.03.255`

Tanabe, K. (2008). Modeling of airborne dust accumulation on solar cells at the Martian surface. *Acta Astronautica*, vol. 62, no. 12, pp. 683–685.

Taylor, J.L. (2009). Reflectance Measurements of Materials Used in the Solar Industry. *PerkinElmer Technical Note*.

Terrat, M.-N. and Joumard, R. (1990). The measurement of soiling. *Science of the total environment*, vol. 93, pp. 131–138.

Verney-Carron, a., Dutot, A.L., Lombardo, T. and Chabas, A. (2012). Predicting changes of glass optical properties in polluted atmospheric environment by a neural network model. *Atmospheric Environment*, vol. 54, pp. 141–148. ISSN 13522310.
Available at: `http://linkinghub.elsevier.com/retrieve/pii/S1352231012002312`

Vivar, M., Herrero, R., Antón, I., Martínez-Moreno, F., Moretón, R., Sala, G., Blakers, A.W. and Smeltink, J. (2010 jul). Effect of soiling in CPV systems. *Solar Energy*, vol. 84, no. 7, pp. 1327–1335. ISSN 0038092X.

Wentworth, C.K. (1922 jul). A Scale of Grade and Class Terms for Clastic Sediments. *The Journal of Geology*, vol. 30, no. 5, pp. 377–392. ISSN 00221376.
Available at: `http://www.jstor.org/stable/30063207`

Wolfertstetter, F. (2013). Reflector Soiling and Cleaning Methods.

Wolfertstetter, F., Pottler, K., Merrouni, A.A., Mezrhab, A. and Pitz-paal, R. (2012). A Novel Method for Automatic Real-Time Monitoring of Mirror Soiling Rates. In: *SolarPACES Conference, Marrakesch, Morocco*, pp. 2–5.

Ziuku, S. and Meyer, E.L. (2012). Mitigating climate change through renewable energy and energy efficiency in the residential sector in South Africa. vol. 2, no. 1, pp. 33–43.

Appendices

Appendix A

Device specifications

This section provides details of main RCMS devices. The first section presents the ISO specification of Kipp & Zonen CH1 pyrheliometer while the second section presents operation specification of Kipp & Zonen SOLYS 2 sun tracker.

A.1 Kipp & Zonen CH1 pyrheliometer

Specification	
ISO classification	**First Class**
Response time (95%)	5s
Zero offset duet to temparature change	± 1W/m^2
Non linearlity (0 to 1000W/m^2)	± 0.2
Non stability (Change/year)	± 0.5
Sensitivity	7 to 14 μ VW/m^2
Operating temparature	-40 to + 80° C
Temparature dependence of sensitivity	± 0.5% (-20 to + 50° C
Impendance	10 to 100 Ω
Spectral range (50% points)	200 to 4000 nm
Typical signal output for atmospheric application	0 to 15 mV
Expected daily uncetainity	± 1%
Madimum irradiance	4000 W/m^2
Full opening view angle	5° ± 0.2°
Slope angle	1° ± 0.2°
Weight (excluding cable)	0.9 Kg
Required tracking accuracy	± 0.5° from ideal

A.2 Kipp & Zonen SOLYS 2 operating specification

	SOLYS 2	Comments
Performance		
Pointing accuracy	< 0.1 °	Meets BSRN requires requirements
Torque	20 Nm	
Payload	20 kg	Balanced
Angular velocity	5 °/s	
Angular acceleration	3.6 °/s²	
Rotation	110 ° zenith	
	540 ° azimuth	
Protection against over rotation and damage	Physical limit stops	
Operating Conditions and Dimensions		
Supply voltage	18 to 30 VDC (nominal 24 DC)	Allows for battery charging or under load
	90 to 264 VAC, 50 / 60 Hz	For world-wide use
Power consumption during Sun Cycle	20 W maximum	DC Power
	120 W maximum	AC Power with heater operating
Power consumption after Sun Cycle	13 W maximum	DC Power
	113 W maximum	AC Power with heater operating
Storage temperature	- 40 to + 50 °C	
Operating temperature range	- 20 to + 50 °C	DC Power
	- 40 to + 50 °C	AC Power (heater standard)
Weight	23 kg	For standard tracker
	5 kg	Tripod stand
Dimensions (WxDxH)	50 x 34 x 38 cm (excluding tripod stand)	Includes standard pyrheliometer mounting
Bubble level accuracy	< 0.1°	Relative to zenith shaft
Compliance to international standards		
Environmental protection	IP 65	Suitable for all-weather outdoor use
CE compliance	Yes	
Materials	Suitable for coastal use and areas with pollution	
Features		
Transmission	Inverted tooth belts	Pre-tensioned, no adjustment needed
Connections	Plug and socket for AC power, DC power, Ethernet	
GPS for location and time / date information	Standard	Antenna on top of housing
Pyrheliometer mounting	One side plate and mounting kit as standard	For Kipp & Zonen CH 1 or CHP 1
Mounting base	Standard tripod	Includes adjustable feet for leveling
LED Indicators for	Power, internal temperature and status	Multi-color to indicate various modes
Customer operation		
Installation	Plug-and-play, no PC	GPS acquires location and time / date

	required	
Functional self test	Standard	Multi-color LED status indicator
Test / diagnostic facility	Standard	Via Ethernet port
Sun tracking mode	Standard	Michalsky algorithm (1988)
Firmware update possible	Flash memory	Via Ethernet port
Maintenance	No scheduled maintenance required	Annual inspection recommended
Automatic restart after power interruption	Yes	
Options		
Sun sensor kit	For active sun tracking	Plug in unit with alignment adjustment. 3.12° field of view
Second side mounting plate	For fitting to zenith axis shaft on opposite side to standard Pyrheliometer mounting	Does not include instrument mounting brackets
Top mounting plate	3 positions for Kipp & Zonen radiometers (with or without CV 2 ventilation units) or Eppley PSP / PIR (with or without VEN ventilation units)	No adaptors required
Shading ball assembly	Includes top mounting plate and second side mounting plate and 2 shading balls on adjustable rods	Shading ball height adjustable to suit radiometers above
Radiometer mounting kits	For Kipp & Zonen CH 1 or CHP 1 Pyrheliometer	All require a side mounting plate
	For PMOD-WRC PMO 6 absolute cavity Pyrheliometer	
	For Middleton SP02 or SP01-L sun photometer	
	For Eppley HF or AHF absolute cavity Pyrheliometer	

Appendix B

Silver glass mirror properties

This chapter shows properties of typical glass mirrors used in CSP applications. Figure B.1 show the variation of solar reflectance for different mirror manufacturers and manufacturing process with mirror thickness. Figure B.3 shows properties of typical silver glass mirror used in experimentation alongside with component forming mirror and silver properties.

B.1 Variation of solar reflectance with glass mirror thickness

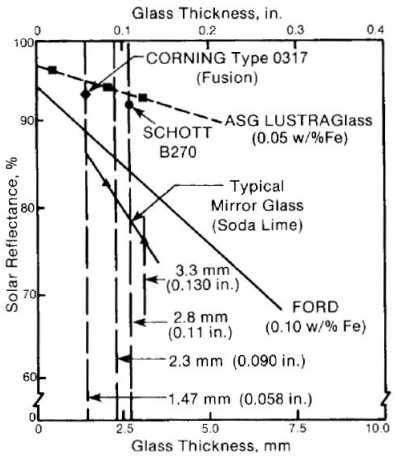

Figure B.1: Reflectance vs mirror thickness (Czanderna *et al.*, 1985).

B.2 PG silver glass - mirror properties

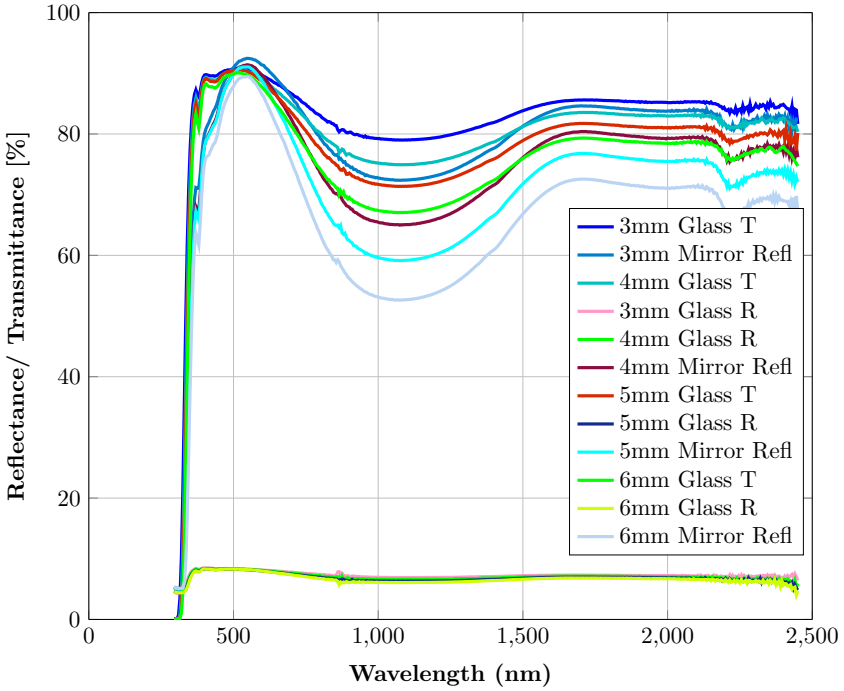

Figure B.2: PG - silver glass mirror properties- variation with thickness(Hugo, 2015).

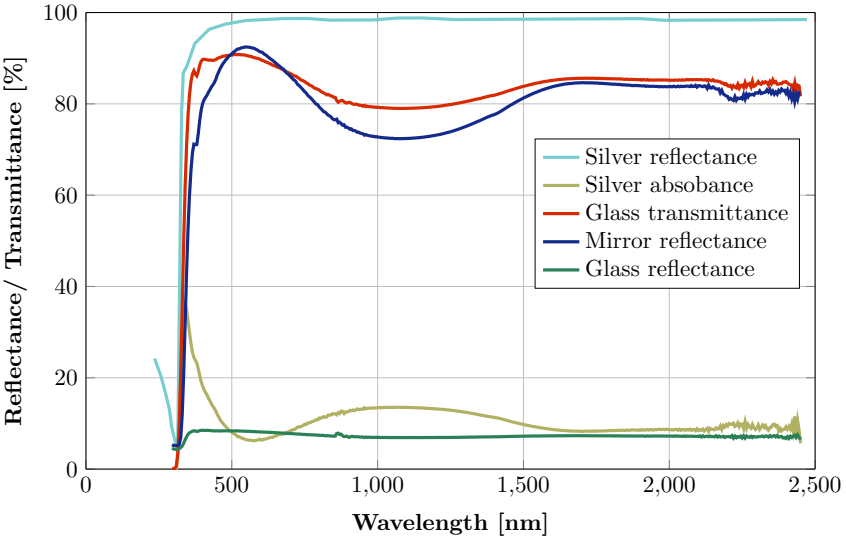

Figure B.3: 3 mm PG - silver glass mirror properties (Hugo, 2015).

Appendix C

RCMS accessories

This chapter presents the pictures of the devices and parts forming cleanliness measurement device for both the existing and manufactured. Manufactured parts for RCMS are shown in Section C.1. A description of the accessories forming the mirror mounting unit is provided in Section C.2. Pictures of RCMS mounting, mirror panel mounting and sitting size of SOLYS 2 sun tracker are shown in Section C.3

C.1 RCMS manufactured accessories

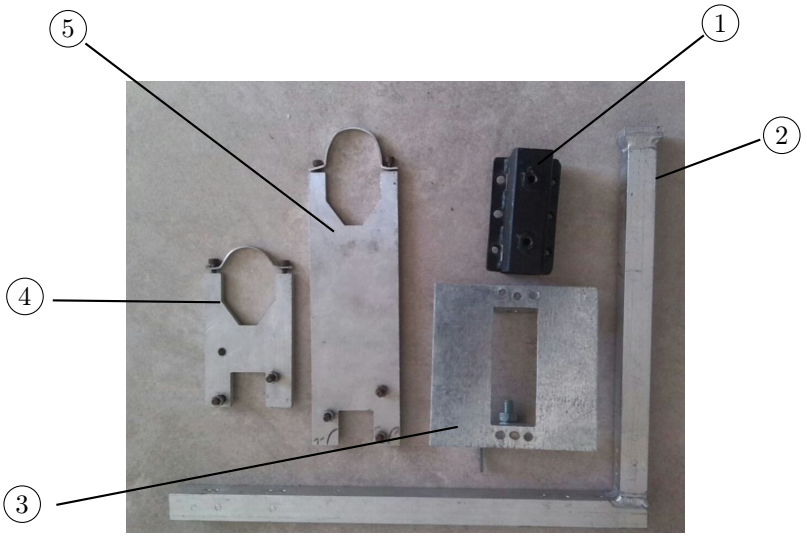

Figure C.1: Solar absolute specular reflectance measurement set up accessories. 1. Mirror frame to tracker mounting bracket. 2. Mirror frame. 3. Mirror plate. 4 and 5. CH(P)1 mounting clamp.

C.2 Mirror mounting Unit

This section provides the details of the mirror mounting unit previously outlined in Section 3.3.1 I(d). Parts forming the mirror mounting unit include: (i) Mounting bracket(part 1); (ii) Mirror support rod (part 2); (iii) Mirror mounting panel (part 3) as shown in Figure C.1.

Two parts forming the mounting bracket include a 25 x 25 x 2 mm square steel bar of length 80 mm with two equally spaced M 6 threaded holes on its length. Opposite to the hole side of the tube is a welded 21 x 9 mm rectangular channel made from 2 mm thick steel plate with a flange formed on either side of the channel. Three 6 mm diameter holes are drilled on either side of the flange equally spaced along the 80 mm length. The second channel with the same features form the second mating part on the shading ball drive arm. The representation of the configuration of the mounting bracket is as shown in CAD drawing in Figure E.3 in Appendix E.

The mirror mounting support rod is made from 20 x 20 mm square aluminium tubing profiles welded to form a 550 x 450 mm L- shape that is attached on the shading drive arm at the lateral end of the horizontal axis from the mounting bracket. The joint from the mounting bracket forms an adjustable distance in the range from 250 mm to 500 mm from the pyrheliometer entrance window to the mirror surface which was used for validation of measurements. As long as not stated otherwise the standard distance used for measurement was 450 mm. On the shorter end, a 25 x 25 x 6 mm with a M 8 threaded hole was formed to enable mounting of mounting plate.

Mirror mounting panel as seen in Figure C.1 in Appendix C, was used for placement of the measured mirror. This part was made from 120 x 120 mm square 2 mm steel plate. A 40 x 80 mm rectangular hole was centrally cut on its surface. This hole provides clamping for the measured mirror and a lateral movement to enable several measurement points. Two 40 x 40 mm flanges on were welded on the back side along the edge of the width of the rectangular hole. One each of the flanges was a 8 mm diameter hole. One of the holes is for fastening of mirror on the plate and the other fastening on the mirror mounting support. The mirror panel itself is inclined by 15° respective the horizontal axis of the tracker such that the reflection angle is the same as in the reference system.

C.3 RCMS pictures

Figure C.2 shows the pyrheliometer and mirror mounting in SOLYS 2 to form the RCMS device. Figure C.3 shows the addition mountings on the sample mirror which provides the mounting on the mirror mounting plate. Figure C.4 and Figure C.5 minimum operating area for SOLYS 2 sun tracker.

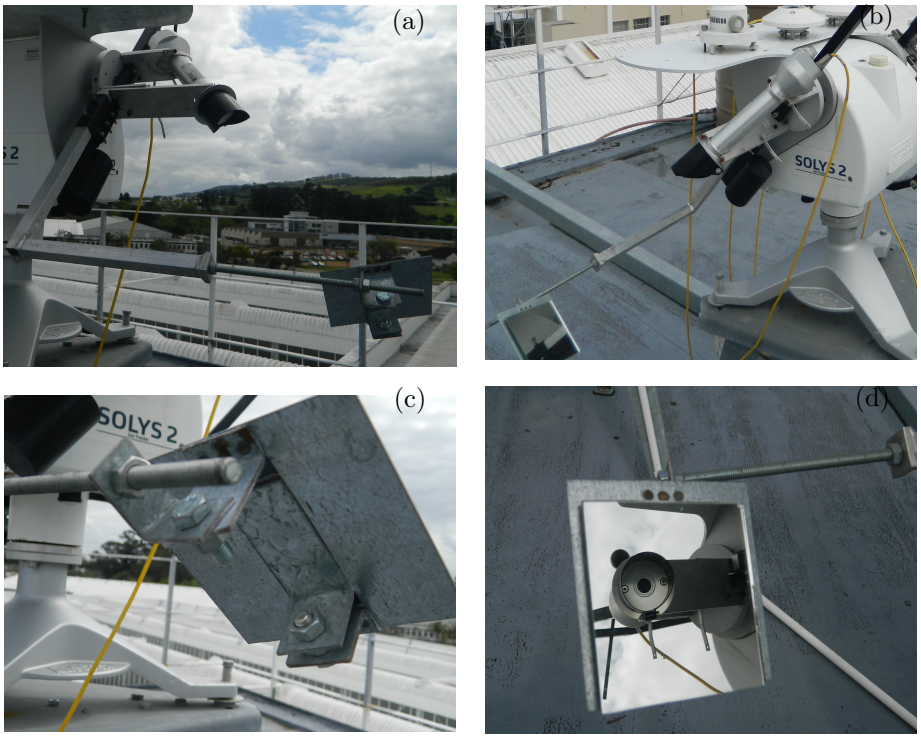

Figure C.2: Measuring section, pyrheliometer mounting and mirror mounting.

(a) Front view **(b)** side view

Figure C.3: Sample mirror mounting with back mounting.

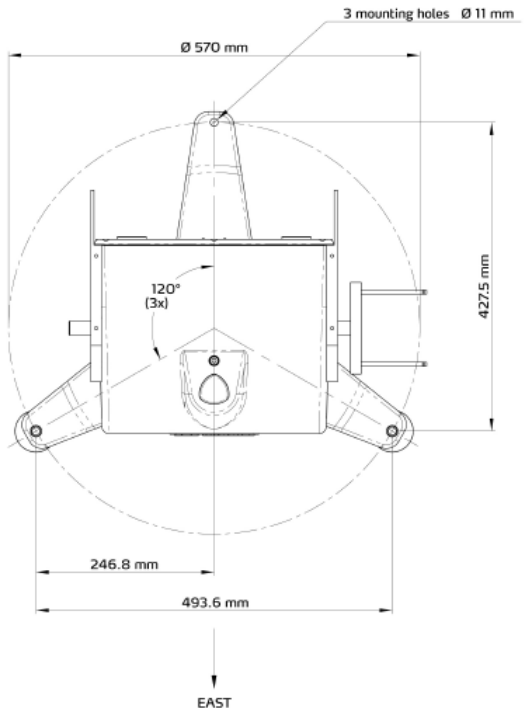

Figure C.4: Kipp & Zonen SOLYS 2 device sitting area (Kipp & Zonen, 2011).

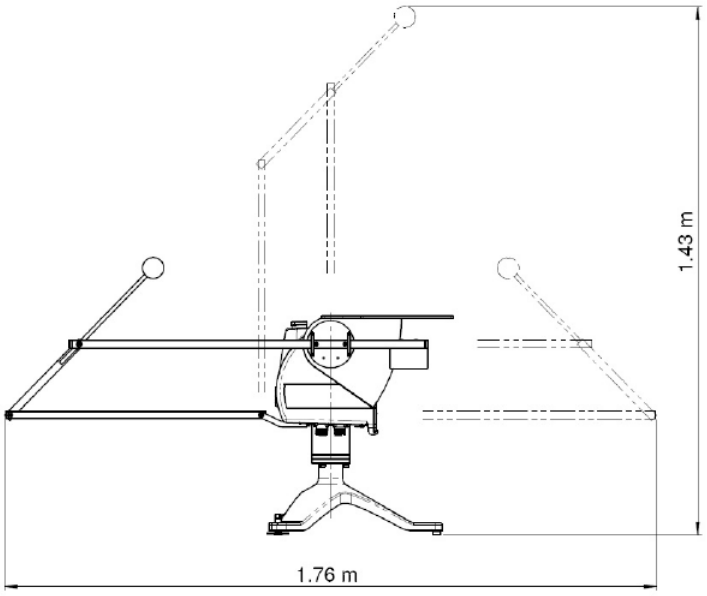

Figure C.5: Kipp & Zonen SOLYS 2 minimum required height operation area (Kipp & Zonen, 2011).

Appendix D

Experimental results data

This chapter presents a summary of measured and calculated results. Table D.1 shows the measured daily weather data values and the corresponding cleanliness calculated from the cleanliness measuring device. Normalisation parameters obtained for model training data are shown in Table D.2. Summaries of the measured and estimated results of model are presented in Table D.3 with the corresponding percentage differences between the measurements.

NOTE: The data provided in Table D.1 was evaluated using the following criteria;

- Temperature and relative humidity obtained as average between the daily maximum and minimum.
- DNI, wind speed and rainfall were logged as daily average.
- Daily average cleanliness was calculated from minute data.
- Experimental data was not collected from in the last week of March up to second week of April when the tracker was damaged and a re design of the RCMS was done.

Table D.1: Time prediction network training data

Date	Temp (° C)	DNI (W/m^2)	Rainfall (mm)	Humidity (%)	wind speed (m/s)	Cleanliness (%)
2015/02/17	24.49	1066.09	0.00	41.90	3.71	100.00
2015/02/18	24.06	1056.40	0.20	46.93	1.27	97.56
2015/02/20	20.39	1035.97	0.50	67.54	3.23	90.75
2015/02/21	17.52	1017.93	0.50	63.71	2.79	89.87
2015/02/22	18.03	1023.34	0.50	61.22	3.85	84.42
2015/02/23	19.26	1064.46	0.50	48.48	2.29	97.40
2015/02/24	21.23	1032.23	0.50	54.99	2.23	92.00
2015/02/25	24.69	977.91	0.50	55.90	4.29	75.76
2015/02/27	20.13	976.57	0.50	74.52	2.37	88.75
2015/02/28	21.91	1045.33	0.50	62.12	1.79	84.42
2015/03/01	21.64	1019.33	0.80	58.44	1.42	83.88
2015/03/02	23.26	1030.21	0.80	59.19	5.14	89.83
2015/03/03	28.61	1048.91	0.80	41.90	3.58	86.59
2015/03/04	30.02	1028.42	0.80	41.23	1.57	87.66
2015/03/06	13.46	1039.56	0.80	34.81	2.21	84.69
2015/03/07	19.49	1029.65	0.80	62.61	1.15	90.59
2015/03/08	17.86	976.66	0.80	74.15	2.48	92.56
2015/03/09	19.01	1038.06	0.80	63.73	1.41	88.75
2015/03/10	22.47	1023.08	0.80	61.80	1.46	86.58
2015/03/11	19.74	954.35	0.80	72.16	2.57	90.86
2015/03/12	22.86	689.26	0.80	55.65	1.23	87.66
2015/03/13	21.75	857.21	0.80	66.88	2.46	91.18
2015/03/14	20.62	953.63	0.80	67.99	3.04	92.00
2015/03/15	24.10	945.16	0.80	58.23	1.51	80.09
2015/03/16	21.03	955.17	1.10	70.81	2.45	84.42
2015/03/17	19.13	715.72	0.00	72.63	3.53	100.00
2015/03/18	21.78	782.84	0.00	58.08	5.70	97.40
2015/03/20	20.13	694.59	0.00	71.55	0.99	94.16
2015/03/21	21.16	761.31	2.10	63.48	2.50	92.00
2015/03/22	21.01	755.33	2.40	66.58	2.42	90.91
2015/03/23	21.42	750.19	2.40	67.71	2.44	89.83
2015/03/24	24.39	681.77	2.40	58.54	4.02	88.20
2015/03/25	23.04	744.55	2.40	64.88	2.65	84.96
2015/04/17	14.64	945.76	0.00	66.06	2.98	100.00
2015/04/18	19.09	963.36	0.00	48.25	4.11	98.00

Date	Temp (° C)	DNI (W/m^2)	Rainfall (mm)	Humidity (%)	wind speed (m/s)	Cleanliness (%)
2015/05/30	15.28	786.45	22.00	83.37	3.19	89.25
2015/05/31	13.37	808.14	22.00	82.60	1.93	87.63
2015/06/01	12.27	320.87	22.00	80.78	1.46	84.41
2015/04/19	19.05	949.04	0.00	46.94	2.11	97.40
2015/04/20	18.83	963.36	0.00	48.49	1.11	88.75
2015/04/21	15.23	891.77	0.00	72.91	1.65	90.81
2015/04/22	19.53	932.93	0.00	54.64	2.47	84.42
2015/04/24	18.48	938.30	0.00	57.19	0.98	97.40
2015/04/25	19.26	940.09	0.00	58.25	0.83	92.00
2015/04/26	17.33	887.29	0.00	63.67	1.59	75.76
2015/04/27	16.86	915.12	0.30	78.52	1.52	88.75
2015/04/28	17.33	923.09	0.30	68.80	0.68	83.34
2015/04/29	17.50	826.89	3.30	64.10	1.49	87.13
2015/05/01	15.50	882.39	3.90	80.75	1.11	84.42
2015/05/02	13.93	905.46	3.90	77.32	0.88	81.18
2015/05/03	17.34	859.55	4.20	78.64	0.72	87.13
2015/05/04	17.23	874.32	4.20	76.13	0.81	80.09
2015/05/05	17.78	868.06	4.20	81.89	1.00	84.42
2015/05/06	14.99	642.14	4.20	80.58	1.76	90.91
2015/05/08	16.41	913.39	4.20	56.97	0.76	90.91
2015/05/09	19.68	891.67	4.20	57.80	0.94	84.96
2015/05/10	16.17	824.88	4.20	75.35	0.95	90.91
2015/05/11	17.46	863.14	4.20	70.79	1.83	90.62
2015/05/12	18.98	877.45	4.20	62.88	1.33	89.54
2015/05/13	19.64	872.97	4.20	57.01	0.83	87.92
2015/05/15	13.17	747.94	8.00	74.14	1.37	84.69
2015/05/16	12.26	772.31	35.00	69.12	1.41	96.47
2015/05/17	14.94	855.23	53.00	78.13	1.03	98.00
2015/05/18	17.14	814.36	53.00	62.18	0.54	97.09
2015/05/19	18.59	813.91	53.00	59.14	2.51	96.45
2015/05/20	16.04	759.32	53.00	81.37	1.72	90.52
2015/05/22	15.50	801.97	53.40	75.48	1.26	91.70
2015/05/23	20.36	736.96	65.00	55.56	0.93	95.22
2015/05/24	16.82	182.15	16.00	66.89	1.03	95.73
2015/05/25	15.97	810.37	22.00	79.63	1.03	96.77
2015/05/26	16.33	826.95	22.00	69.37	2.20	93.55
2015/05/27	14.30	54.79	22.00	87.91	2.23	91.40
2015/05/29	16.45	775.93	22.00	83.52	2.74	90.32

Date	**Temp** (° C)	**DNI** (W/m^2)	**Rainfall** (mm)	**Humidity** (%)	**wind speed** (m/s)	**Cleanliness** (%)
2015/06/02	13.85	741.39	22.00	59.98	5.38	83.87
2015/06/03	15.50	0.42	22.00	74.05	4.12	87.63
2015/06/04	13.67	843.42	22.00	78.15	3.04	96.77
2015/06/05	13.92	854.62	22.00	68.37	2.81	88.17
2015/06/07	11.62	890.43	22.00	71.17	0.73	90.22
2015/06/08	12.17	906.23	22.00	61.38	0.57	83.87
2015/06/09	12.57	918.66	22.00	60.54	0.69	96.77
2015/06/10	16.07	890.75	24.00	51.59	0.69	91.40
2015/06/12	13.37	731.45	24.00	81.10	0.62	75.27
2015/06/13	14.40	774.66	32.40	73.06	0.77	88.17
2015/06/14	15.48	833.68	36.00	71.10	1.51	82.80
2015/06/15	13.21	825.24	37.00	77.54	1.82	86.56
2015/06/16	13.08	402.20	37.00	84.76	2.23	83.87
2015/06/17	12.42	756.79	37.00	83.31	2.39	80.65
2015/06/18	12.01	692.33	37.00	73.12	1.00	86.56
2015/06/20	12.41	869.39	37.00	76.93	0.75	79.57
2015/06/21	16.45	839.40	37.00	59.29	0.73	83.87
2015/06/22	13.22	895.85	37.00	75.89	0.87	90.32
2015/06/23	12.97	837.19	37.00	68.59	1.76	89.78
2015/06/24	13.46	831.43	37.00	78.04	3.39	92.43
2015/06/26	9.87	866.35	37.00	83.67	0.69	93.64
2015/06/27	10.23	894.08	37.00	68.45	0.65	92.62
2015/06/28	10.75	780.30	37.00	72.93	1.11	88.46
2015/06/29	12.62	742.66	37.00	76.45	1.40	83.31

Table D.2: Input normalization parameters

Parameter	b_{max}	b_{min}
Cleanliness [%]	100.00	75.21
Wind speed [m/s]	5.72	0.54
Cumulative rainfall [mm]	65.00	0.00
Temperature [C]	30.02	9.87
Relative humidity [%]	87.91	34.81

Table D.3: Comparison between actual and estimated cleanliness

Date	Measured Cleanliness [%]	Estimated Cleanliness [%]	% Difference
29-May	94.7	96.0	1.4
30-May	94.4	92.5	-2.1
31-May	92.9	91.8	-1.1
01-June	89.5	91.0	1.7
02-June	85.9	90.5	5.1
03-June	87.8	90.1	2.6
04-June	90.9	90.3	-0.7
05-June	93.3	91.2	-2.3
06-June	94.0	92.5	-1.6
07-June	89.9	92.4	2.7
08-June	86.9	90.5	3.9
09-June	92.9	93.3	0.4
10-June	94.2	95.1	0.9
11-June	94.3	92.3	-2.3
12-June	93.3	90.9	-2.7
13-June	90.2	90.1	-0.1
14-June	87.1	90.0	3.3
15-June	88.7	89.7	1.1
16-June	91.2	91.1	-0.2
17-June	93.9	90.7	-3.5
18-June	94.4	92.1	-2.5
19-June	93.4	92.3	-1.2
20-June	92.6	90.8	-1.9
21-June	89.5	88.6	-1.0
22-June	85.3	86.6	1.4
23-June	87.3	87.0	-0.4
24-June	89.8	88.4	-1.6
25-June	92.4	90.3	-2.4
26-June	93.6	91.3	-2.5
27-June	92.6	89.5	-3.4
28-June	88.4	88.7	0.3
29-June	83.3	88.1	5.4

Appendix E

CAD drawings

This section presents the CAD drawing of the manufactured parts used in the development of real time cleanliness monitoring device. Figure E.1 and Figure E.2 shows the specifications of the two modified pryheliometer clamps manufactured. Figure E.3 shows the specifications of zenith mounting used to connect the mirror mounting rod to the SOLYS 2 zenith rod.

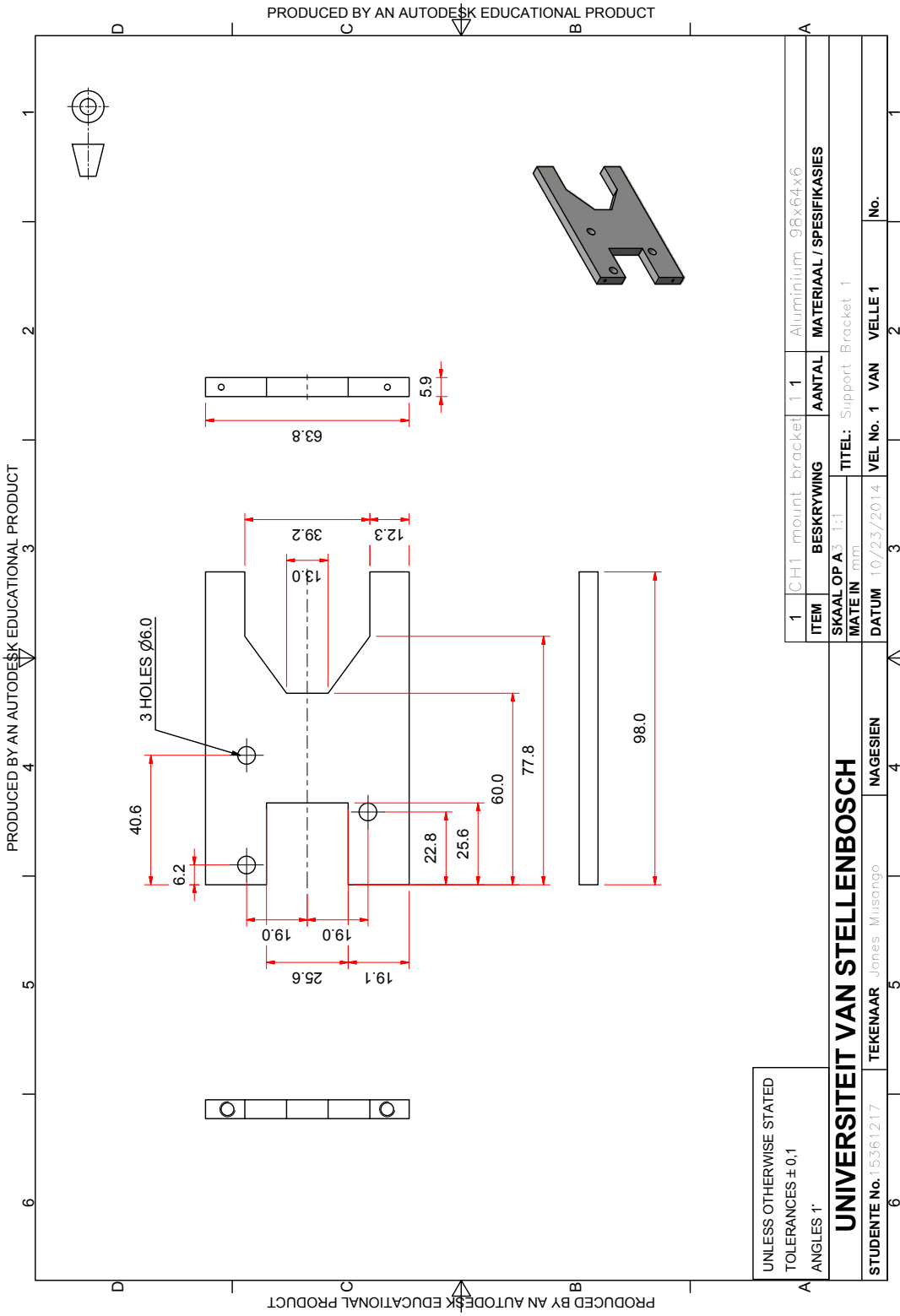

Figure E.1: Pyrheliometer (Kipp & Zonnen CH1 mounting clamp 1

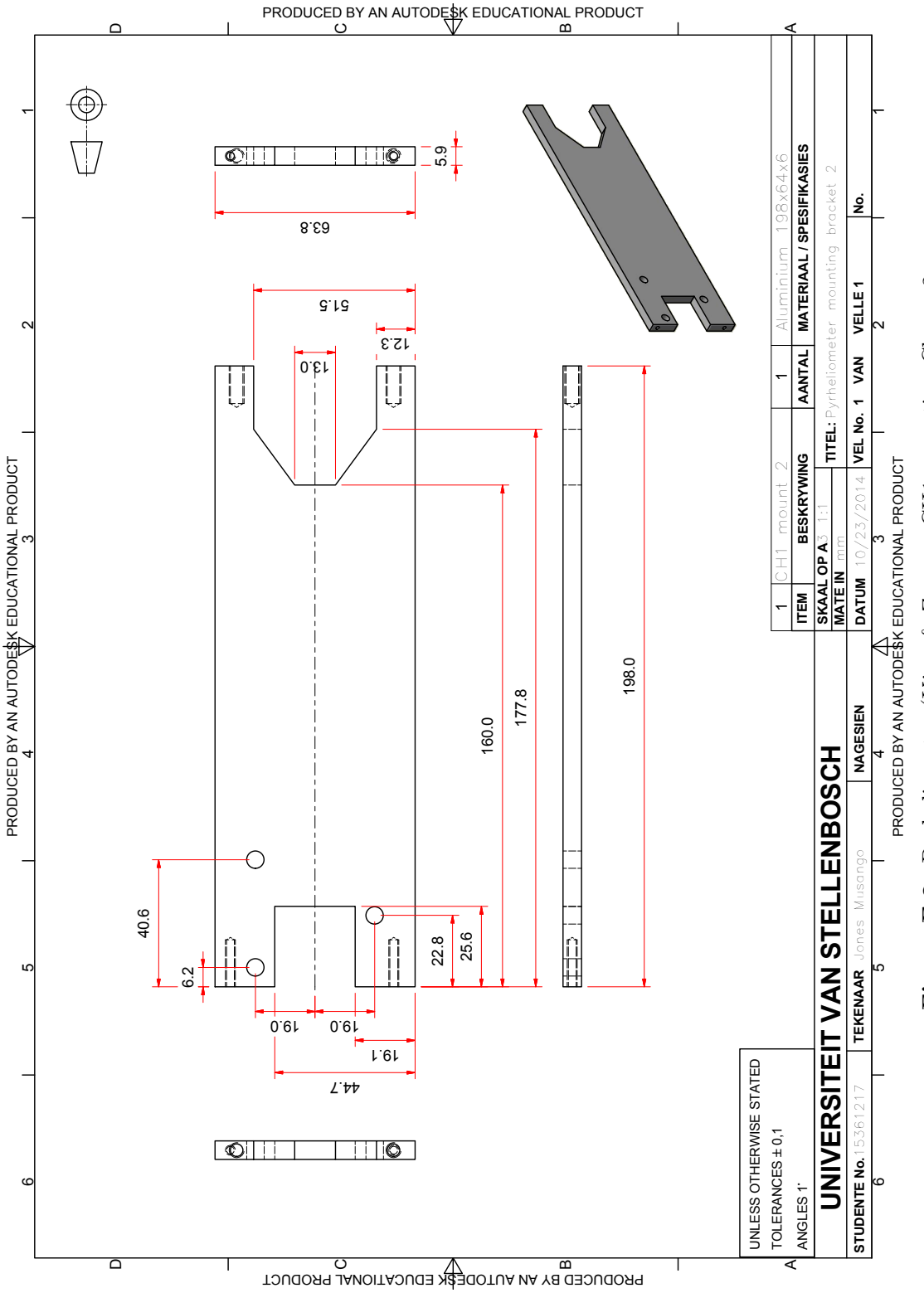

Figure E.2: Pyrheliometer (Kipp & Zonnen CH1 mounting Clamp 2

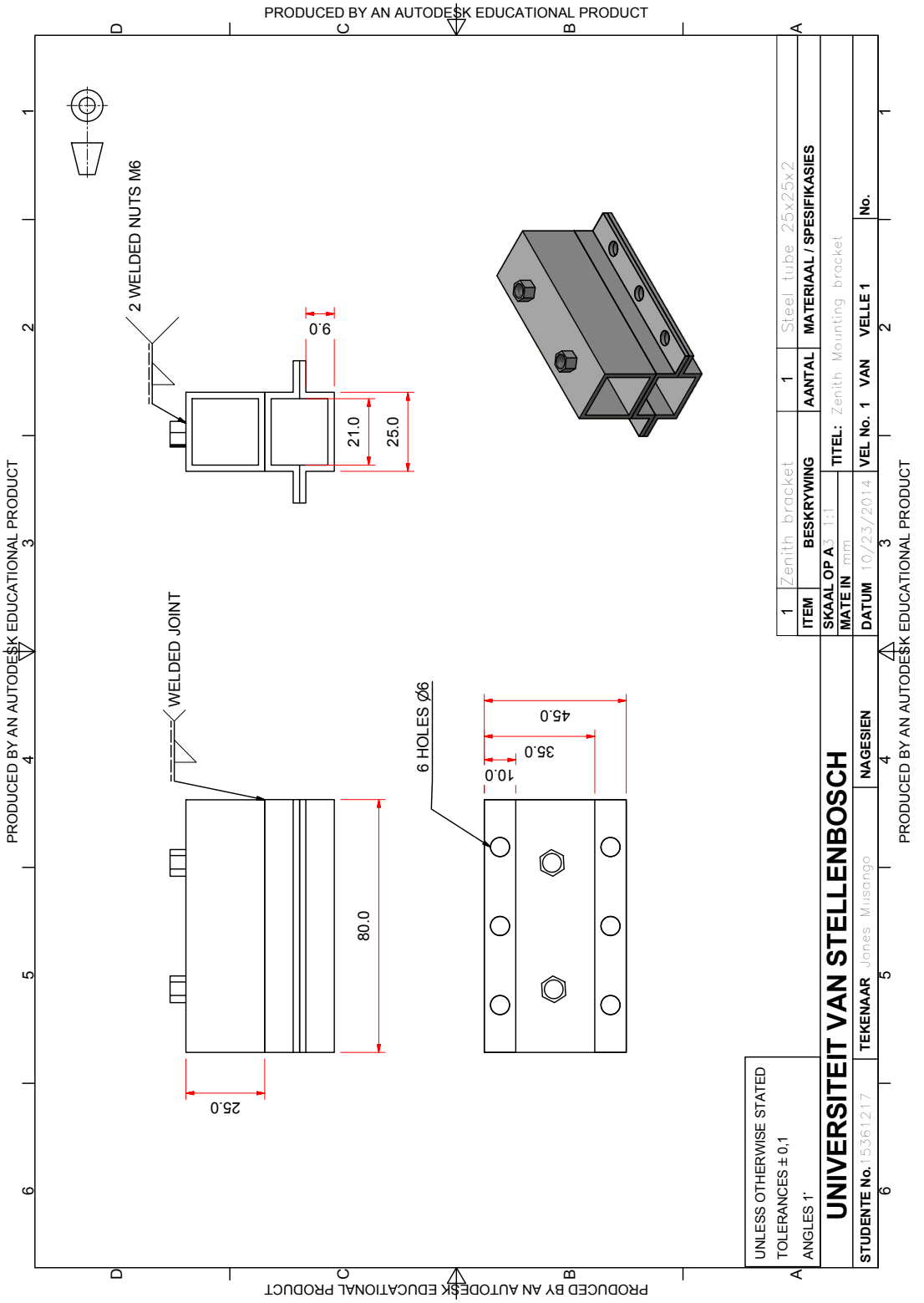

Figure E.3: Shading ball arm- mirror mounting bracket

Appendix F

Sonbesie weather station

Figure F.1 shows the location of Sonbesie Weather Station in Stellenbosch University Civil Engineering building. A diagrammatic architecture of instrumentation at the station is presented in Figure F.2. Average weather conditions of the test location and the foregrounding are presented in Figure F.3

F.1 Experimental test location

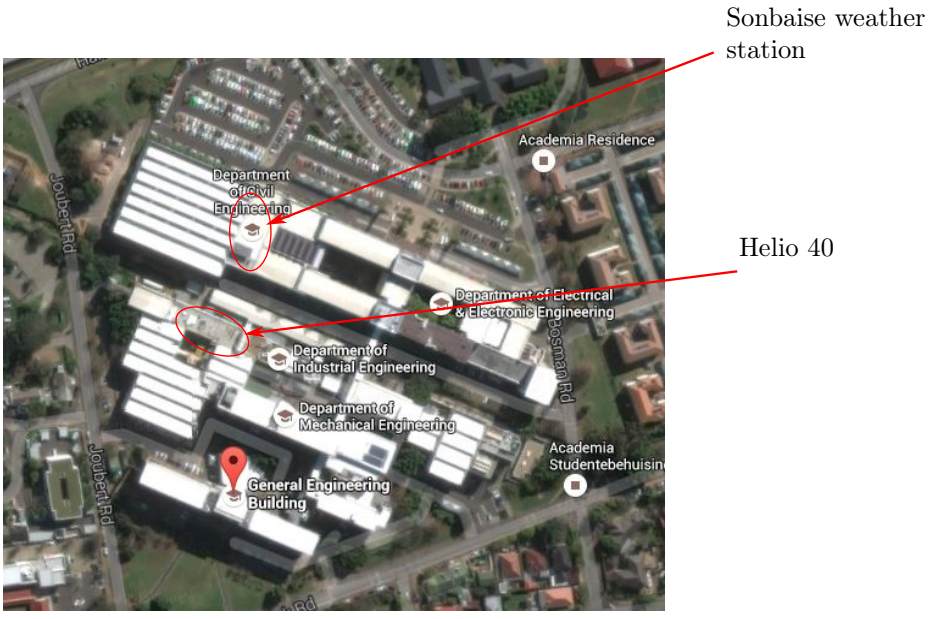

Figure F.1: Location of Sonbesie Weather Station (Google Earth 6.0, 2015).

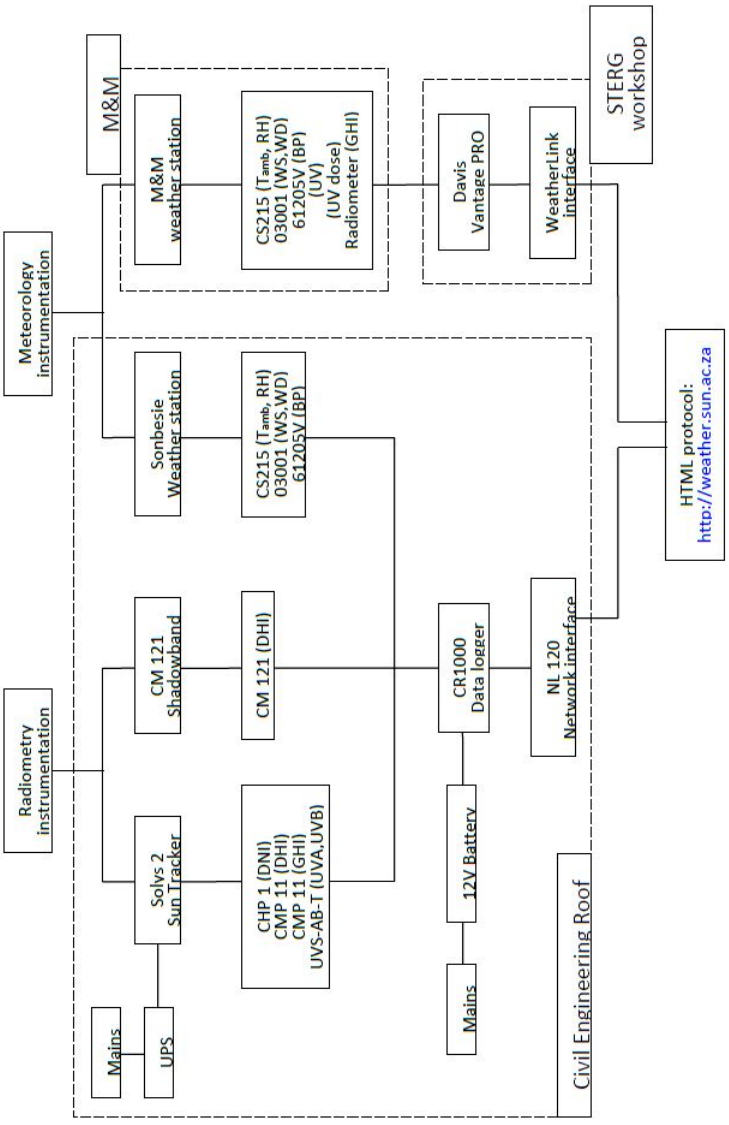

Figure F.2: Sonbesie Weather Station device architecture (Meijers, 2015).

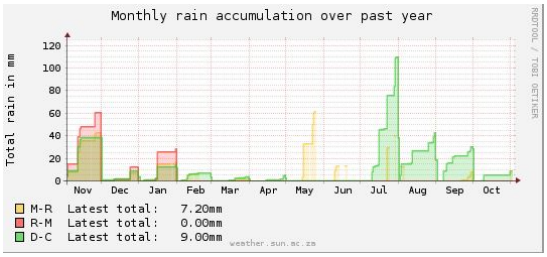

(a) Average of annual variation of rainfall.

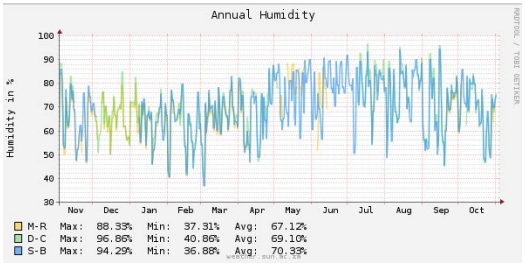

(b) Annual average variation of Humidity.

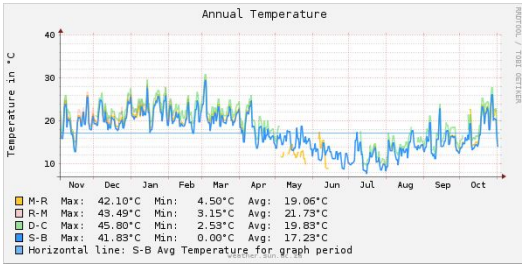

(c) Average annual variation of Temperature.

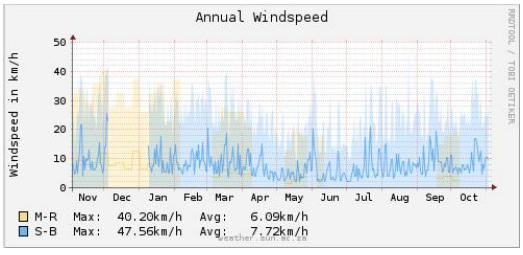

(d) Average annual variation of wind speed

Figure F.3: Average annual weather condition in Stellenbosch as measured from Sonbesie Weather Station (Meijers, 2015).